



Michigan Technological University
Create the Future Digital Commons @ Michigan Tech

Dissertations, Master's Theses and Master's
Reports - Open

Dissertations, Master's Theses and Master's
Reports

2011

Effects of silicon content and cooling rate on mechanical properties of heavy section ductile cast iron

Meghan Haycock
Michigan Technological University

Follow this and additional works at: <https://digitalcommons.mtu.edu/etds>



Part of the [Engineering Science and Materials Commons](#)

Copyright 2011 Meghan Haycock

Recommended Citation

Haycock, Meghan, "Effects of silicon content and cooling rate on mechanical properties of heavy section ductile cast iron ", Master's Thesis, Michigan Technological University, 2011.
<https://doi.org/10.37099/mtu.dc.etds/25>

Follow this and additional works at: <https://digitalcommons.mtu.edu/etds>



Part of the [Engineering Science and Materials Commons](#)

EFFECTS OF SILICON CONTENT AND COOLING RATE ON MECHANICAL PROPERTIES OF
HEAVY SECTION DUCTILE CAST IRON

By

Meghan Haycock

A THESIS

Submitted in partial fulfillment of the requirements of

MASTER OF SCIENCE

(Materials Science and Engineering)

MICHIGAN TECHNOLOGICAL UNIVERSITY

2011

This thesis, "Effects of Silicon Content and Cooling Rate on Mechanical Properties of Heavy Section Ductile Cast Iron," is hereby approved in partial fulfillment of the requirements for the degree of MASTER OF SCIENCE IN MATERIALS SCIENCE AND ENGINEERING.

Department of Materials Science and Engineering

Signatures:

Thesis Advisor

Dr. Paul Sanders

Department Chair

Dr. Mark Plichta

Date

*This thesis is dedicated to my fiancé,
without whose love and unwavering support
this would not have been possible.*

*And to my parents for teaching
me that I am capable of anything.*

Table of Contents

Table of Contents.....	iv
List of Figures	vii
List of Tables	xiv
Acknowledgements.....	xv
Preface	xvi
Abstract	xvii
1 Introduction.....	1
1.1 The Wind Industry	1
1.2 Structure and Design Requirements of Wind Turbine Generators	1
1.3 Wind Turbine Generator Materials	2
2 Background.....	3
2.1 Alloying Elements and Their Effect on Mechanical Properties	3
2.1.1 Carbon	3
2.1.2 Silicon.....	3
2.1.3 Carbon Equivalent.....	4
2.1.4 Magnesium	5
2.1.5 Phosphorous.....	5
2.1.6 Sulfur.....	5
2.1.7 Nickel	5
2.1.8 Carbide and Pearlite Promoters	6
2.1.9 Cerium	7
2.2 Effect of Microstructure on Toughness	7
2.2.1 Nodule Count	7
2.2.2 Nodularity.....	9
2.2.3 Microstructure Matrix	9
2.3 Effect of Solidification Rate and Segregation on Toughness.....	10
2.4 Hypotheses.....	11
2.4.1 Effect of Material Chemistry on Microstructure and Toughness	11
2.4.2 Effect of Cooling Rate on Segregation and Toughness.....	12
3 Experimental Procedure.....	13
3.1 Selection and Determination of Alloys and Charge Mix	13
3.2 Mold Preparation.....	14
3.3 Melting and Solidification.....	16
3.4 Sample Preparation.....	17
3.5 Chemical Analysis.....	18

3.6	Metallography	18
3.6.1	<i>Nodularity</i>	18
3.6.2	<i>Microstructure</i>	19
3.7	Mechanical Testing	20
4	Experimental Results	22
4.1	Pouring Results	22
4.2	Cooling Curves	22
4.2.1	<i>Baseline</i>	22
4.2.2	<i>Medium Si</i>	25
4.2.3	<i>High Si</i>	27
4.2.4	<i>Cooling Rates</i>	29
4.3	Chemical Analysis	30
4.4	Metallography	31
4.4.1	<i>Nodularity and Nodule Count</i>	31
4.4.2	<i>Matrix Microstructure</i>	31
4.5	Mechanical Testing	33
4.5.1	<i>Tensile</i>	33
4.5.2	<i>Charpy Impact</i>	37
4.5.3	<i>Vickers Microhardness</i>	38
5	Discussion	42
5.1	ANOVA Analysis	42
5.2	Cooling Rate	42
5.3	Microstructure	45
5.3.1	<i>Composition</i>	45
5.3.2	<i>Cooling Rate</i>	46
5.4	Hardness	51
5.4.1	<i>Composition</i>	51
5.4.2	<i>Cooling Rate</i>	52
5.5	Tensile Testing	54
5.5.1	<i>Composition</i>	54
5.5.2	<i>Cooling Rate</i>	57
5.5.3	<i>Relative Effect of Si Content and Cooling Rate</i>	61
5.6	Impact Toughness	63
5.6.1	<i>Composition</i>	63
5.6.2	<i>Cooling Rate</i>	65
5.6.3	<i>Relationship Between Impact Energy, Elongation and Tensile Strength</i>	67
6	Conclusions	69
6.1	Hypothesis 1 - Effect of Composition	69
6.2	Hypothesis 2 - Effect of Cooling Rate	69
	References	71

Appendix A	Mass Balance and Charge Determination for Each Heat	74
Appendix B	Photomicrographs of Test Castings	81
Appendix C	ANOVA and Linear Regression Results for Cooling Rate Analysis	97
Appendix D	ANOVA and Linear Regression Results for Quantitative Metallography Results.	100
Appendix E	ANOVA and Linear Regression Results for Analysis of the Effect of Si Content and Cooling Rate on Hardness	102
Appendix F	ANOVA and Linear Regression Results for Mechanical Testing Data	103
Appendix G	ANOVA and Linear Regression Results for Charpy Impact Results ..	109

List of Figures

Figure 1.1: The top of a wind turbine generator showing the different components. (Image reprinted from Puttenat 2008).	1
Figure 2.1: Graph showing the effects of temperature on impact toughness. Note that the DBTT increases for increasing amounts of Si. (Image reprinted from Ductile Iron Society 1990).....	4
Figure 3.1: Schematic showing the pattern that was cast. The sprue is in the center with three runners leading to the three blocks. The sprue area:runner area:gate area is 1:2.7:2.7	15
Figure 3.2: Series of images showing molding process. In (a), the drag is in its proper orientation after being filled and flipped. The placement of the pattern with place holder thermocouples in place is shown in (b). The completed cope is pictured in (c) and (d) shows the entire mold ready for a pour. The Germalloy has been printed in the pouring basin in (d)	16
Figure 3.3: Schematics for slice location (left) and sample locations in each slice (right).	17
Figure 3.4: Sectional view of section where metallography sample was taken from. Note that the mounted surface is perpendicular to the chill direction.....	20
Figure 4.1: Cooling curve for the baseline alloy, actively chilled block. The eutectic arrest at the 120mm thermocouple occurred at 1154°C and the eutectoid arrest occurred at 746°C. The recalescence in the 0mm thermocouple is 161°C and decreases with increasing distance from the chill	23
Figure 4.2: Cooling curve for baseline alloy, passively chilled block. The eutectic arrest in the 120mm thermocouple occurred at 1155°C and the eutectoid occurred at 746°C. The recalescence in the 0mm thermocouple is 220°C.....	24
Figure 4.3: Cooling curve for baseline, non-chilled block. There was not a large difference in cooling between the thermocouples. The eutectic arrest occurred at 1154°C and the eutectoid occurred at 750°C.....	24
Figure 4.4: Cooling curve for heat 4, active chill, medium Si alloy. The eutectic arrest occurred at 1150°C and the slight eutectoid arrest occurred at 800°C.	25
Figure 4.5: Cooling curve for heat 4, passive chill, Medium Si alloy. The eutectic arrest occurred at 1146°C and the slight eutectoid arrest occurred at 800°C.	26
Figure 4.6: Cooling curve for heat 4, no chill, Medium Si alloy. There was not a large difference in cooling rate with distance from the bottom of the	

casting. The eutectoid arrest occurred 1160°C while the eutectoid arrest occurred at 800°C	26
Figure 4.7: Cooling curve for actively chilled block, high Si alloy. Two arrests took place: eutectic (1154°C) and the eutectoid (793°C).	27
Figure 4.8: Cooling curve for high Si alloy, passively chilled block. The eutectic arrest occurred at 1159°C and the eutectoid arrest occurred at 796°C.	28
Figure 4.9: Cooling curve for non-chilled block, heat 6, high Si alloy. The eutectic arrest occurred at 1160°C and the eutectoid occurred at 814°C. The 0mm thermocouple experiences a neoeutectic at 1130°C.	28
Figure 4.10: Plot of cooling rate as a function of distance from the chill. As distance increases, the cooling rate decreases for the chilled samples but remains constant for the non-chilled sample.	30
Figure 4.11: Plot showing Young's modulus as a function of distance from the chill	33
Figure 4.12: Plot of yield stress as a function of distance from the chill.....	34
Figure 4.13: Plot of tensile strength as a function of distance from the chill ..	34
Figure 4.14: Plot of strain as a function of distance from the chill	35
Figure 4.15: Plot showing hardness as a function of distance from the chill for each block from the baseline alloy.....	38
Figure 4.16: Plot showing hardness as a function of distance from the chill for each block from the medium Si alloy.	39
Figure 4.17: Plot showing hardness as a function of distance from chill for each block from the high Si alloy.	39
Figure 4.18: Average Vickers hardness of each block plotted as a function of distance from the chill. Note that each heat is grouped together and they are distinct from each other.	40
Figure 5.1: Cooling rate as a function of distance from the chill for the chilled blocks and non-chilled blocks. The non-chilled blocks experienced a relatively constant cooling rate while the chilled blocks showed a dramatic decrease in cooling rate for increasing distance from the chill. However, even at the furthest point, the chilled cooling rate is still about 3 times faster than the non-chilled block.	44
Figure 5.2: Effect of distance from the chill, presence of chill and Si content on the cooling rate. The presence of a chill and the distance were both significant to the cooling rate but the Si content was not. The line at 15 indicates the mean of the data.	44
Figure 5.3: Nodularity vs. Si content. The error bars are one standard error of the mean and are large because this plot also includes the effect of cooling rate.	45
Figure 5.4: Nodule count as a function of Si content. The error bars are one standard error of the mean and are large because they include the effect of cooling rate.....	46

Figure 5.5: Nodularity as a function of cooling rate. The error bars are one standard error of the mean. They are smaller in this figure than in Figure 5.3 because the effect of Si, present in the data, is smaller than cooling rate.	48
Figure 5.6: Nodule count as a function of cooling rate. The error bars are one standard error of the mean and are small because the effect of Si content is small compared to the effect of cooling rate.	48
Figure 5.7: Effect of Si content (a) and cooling rate (b) on nodularity. An increase in Si content decreases nodularity while an increase in cooling rate results in an increase in nodularity. By comparing (a) and (b), it can be seen that the cooling rate has a much larger effect on the nodularity than the Si content.	49
Figure 5.8: Effect of Si content (a) and cooling rate (b) on nodule count. Comparing (a) and (b) shows that the cooling rate has a larger effect on the nodule count than Si, although an increase in either will result in an increase in nodule count.	49
Figure 5.9: Photomicrographs showing as-polished graphite structures of the test castings. Examples of high nodule counts are shown in samples Baseline-A1 (a), Medium Si-A1 (c) and High Si-P1 (e) while lower nodule counts and larger nodules are exemplified in samples Medium Si-A5 (b), Medium Si-P5 (d) and High Si-P5 (f).	50
Figure 5.10: Hardness as a function of Si content. The error bars are one standard error of the mean and are small.	52
Figure 5.11: Hardness as a function of cooling rate for the chilled and non-chilled castings. The errors bars are one standard error of the mean and are large because the data includes the effect of Si content.	53
Figure 5.12: Plot showing of effect of Si content and cooling rate on hardness. From this plot it is easy to see that Si content is significant while cooling rate is not.	53
Figure 5.13: Etched micrographs of the baseline alloy showing the matrix microstructure of the test blocks. Sample Baseline-P1 (a) and Baseline-P3 show an increase in nodule size, ferrite grain size, and presence of intercellular pearlite as well as a decrease in nodule count.	54
Figure 5.14: Yield stress as a function of Si content. It is clear that an increase in Si content results in an increase in yield stress. The error bars represent one standard error the mean.	55
Figure 5.15: Tensile strength as a function of Si content. Just as for yield stress, as Si content increases, an increase in tensile strength results. The error bars are one standard error of the mean.	56
Figure 5.16: Elongation as a function of Si content. For an increase in Si, which also results in an increase in strength, there is a decrease in elongation. The error bars represent one standard error of the mean.	56

Figure 5.17: Young's modulus measure ultrasonically as a function of Si content. The error bars represent one standard error of the mean. It can be seen that for an increase in Si content, a decrease in modulus occurs.....	57
Figure 5.18: Comparison of cooling rate for the baseline alloy. Image (a) is from the sample closest to the chill while (b) is from the center of non-chilled block. The grain size in (a) is much finer than in (b) and this was reflected in the strength of the material. The yield stress/tensile strength for (a) and (b) were 240MPa/398MPa and 224MPa/373MPa, respectively.....	58
Figure 5.19: Yield stress as a function of cooling rate. The error bars are one standard error of the mean and are large because they include the effect of Si. A correlation is difficult to discern, but ANOVA showed that cooling rate is a significant factor for yield stress.	59
Figure 5.20: Tensile strength as a function of cooling rate. The error bars are one standard error of the mean and are large because they include the effect of Si on the tensile strength.....	59
Figure 5.21: Elongation as a function of cooling rate. The error bars are for one standard error of the mean and include the effect of Si causing them to be large.	60
Figure 5.22: Young's modulus as a function of cooling rate. The error bars are for one standard error of the mean and include the effect of Si resulting in a large error.	60
Figure 5.23: Effect of cooling rate and Si content on yield stress. Both factors are significant and an increase in either factor will result in an increase in yield stress.....	61
Figure 5.24: Effect of cooling rate and Si content on tensile strength. Both factors are significant and an increase in either will result in an increase in tensile strength.	62
Figure 5.25: Effect of cooling rate and Si content on elongation. Both factors are significant and an increase Si results in decreased elongation while an increase in cooling rate can increase the elongation.	62
Figure 5.26: Effect of cooling rate and Si content on ultrasonic modulus. Si content is significant while cooling rate is not. An increase in Si content will decrease Young's modulus of the casting.	63
Figure 5.27: Impact energy for the three alloys as a function of impact temperature. By comparing the three alloys, it can be seen that the baseline had the highest impact energies for all temperatures while the medium and high Si alloys has the lowest.....	64
Figure 5.28: Figure from the Ductile Iron Society showing the impact energy vs. temperature for different Si alloys. The data from this study has been placed on the plot for comparison. (Image reprinted from Ductile Iron Society 1990)	65

Figure 5.29: Impact energy as a function of temperature. The medium and high Si impact energies for the chilled samples are the same as the non-chilled samples and are, therefore, not visible on this graph.....	66
Figure 5.30: Plot showing effect of Si content and cooling rate on impact energy.	67
Figure 5.31: Plot showing impact energy as a function of tensile strength and the equation for the line of best fit. This shows that for an increase in tensile strength, a large decrease in impact energy results.....	68
Figure B.1: Baseline-A1. (a) and (b) are from close to the surface while (c) is from further inside the casting. Note decrease in nodule count and the appearance of pearlite in (c) compared to (a) and (b).....	81
Figure B.2: Micrographs of sample Baseline-A3. Image (a) is taken at 100x in the as-polished condition while (b) is taken at 50x after being etched with 2% Nital. There is relatively the same amount of intercellular pearlite present as in Baseline-A1.....	82
Figure B.3: Baseline-A5. Note the larger intercellular pearlite colonies present in (c) and the degenerate graphite that begins to appear in (b). (a) shows a representative area of the sample. Additionally, this sample shows larger graphite nodules when compared to Baseline-A1 and -A3.	82
Figure B.4: Baseline-P1. Images (a) and (c) are taken close to the chill/casting interface while (b) and (d) are taken further away. Note the decrease in nodule count and increase in nodule size ((a) and (b)) and the increase in ferrite grain size ((c) and (d)) as distance from the chill increases.	83
Figure B.5: Baseline-P3. Image (a) shows a representative area of the sample while (b) shows the presence of degenerate graphite. When comparing (c) with Figure B.4 (d), it is apparent that there is an increase in the size of the intercellular pearlite colonies. An increase in nodule size can also be seen by comparing Figure B.4 (a) and (b) with (a) above. .	84
Figure B.6: Baseline-P5. A dramatic decrease in nodule count compared to Figure B.4 can be seen in (b). Image (a) shows the presence of chunky graphite. Additionally, (c) shows degenerate graphite.....	84
Figure B.7: Baseline-N1. Note that (a) shows larger and fewer nodules than the Baseline-A and Baseline-P blocks. Additionally, there was flake graphite at the casting surface (b). Pearlite was present close to the surface (c), but became more prevalent as distance from the surface increased (d).	85
Figure B.8: Baseline-N3. Nodule count has improved, but it is still inferior to the actively and passively chilled blocks. Nodularity has also deteriorated (b). Presence of intercellular pearlite has decreased (c).	86

Figure B.9: Baseline-N5. The nodule count is about the same compared to Baseline-N3 in (a). Less intercellular pearlite is present as shown in (b).	86
Figure B.10: Medium Si-A1. The nodule count in this sample was very high at the chill/casting interface (a); however, there was some degenerate graphite present at the surface (b). This sample had a region of pearlite (c) that was also visible macroscopically (e). Image (d) shows a representative area.....	87
Figure B.11: Medium Si-A3. Both (a) and (b) are representative of the sample. Very little degenerate graphite and pearlite were present and there was a bimodal distribution in nodule size.	88
Figure B.12: Medium Si-A5. Some degenerate graphite was present in the form of spiky, chunky and exploded. The spiky graphite is visible in (a). Intercellular pearlite colonies also began to appear (b).	88
Figure B.13: Medium Si-P1. Small nodules and a high nodule count seen in (a). The ferrite is very fine at the surface (c) and slightly coarser further away from the chill (b).....	89
Figure B.14: Medium Si-P3. Note that the graphite nodules in (a) are larger than in Figure B.13(a). Also, more intercellular pearlite colonies are present and in the sample closer to the chill.	89
Figure B.15: Medium Si-P5. The nodules are roughly the same as in Medium Si-P3. Relatively the same amount of intercellular pearlite is present. Some degenerate graphite was also present.....	90
Figure B.16: Medium Si-N1. This sample had noticeable lower nodule count and poor nodularity (a). Compacted graphite was present on the surface of the casting (b) and (d). Intercellular pearlite was also present here where it was virtually absent in the actively and passively chilled blocks.....	90
Figure B.17: Medium Si-N3. Poor nodularity and nodule count (a), (b). Nearly identical to medium Si-N1	91
Figure B.18: Medium Si-N5. This sample has very large nodules and the presence of exploded graphite and large intercellular pearlite colonies (c). It also had a low nodule count (a), (b).....	91
Figure B.19: High Si-A1. Note that it has a very fine graphite morphology (a) and ferrite matrix (b). This sample also had an area of pearlite (d) similar to the medium silicon-A1 sample.....	92
Figure B.20: High Si-A3. The nodules were larger and there was a lower nodule count than in the sample closer to the chill (a). There was also more pearlite present (b). One region showed an unusually high amount of pearlite (c).....	93
Figure B.21: High Si-A5. Image (a) shows a representative area with decent graphite structure while (b) shows an area with a fair amount of degenerate graphite. The matrix microstructure in (c) and (d), which	

	were obtained at 50x while (a) and (b) were obtained at 100x, is coarser than in the A3 sample. Intercellular pearlite is also present in this sample (c), (d).....	93
Figure B.22:	High Si-P1. This sample had a very fine microstructure like A1. The graphite nodules are small and well-formed (a). The surface shows evidence of compacted graphite (b), but there is no other degenerate graphite. The ferrite was very fine (c); there was also a region of pearlite (d).....	94
Figure B.23:	High Si-P3. This sample had larger nodules and a lower nodule count than P1 (a). Intercellular pearlite also began to appear (b).	94
Figure B.24:	High Si-P5. A fair amount of degenerate graphite was observed in this sample. In (a), spiky graphite is present while in (b), chunky graphite is present near a portion of the thermocouple. Image (c) shows a representative area with a bimodal distribution in nodules and intercellular pearlite present.	95
Figure B.25:	High Si-N1. This sample had a much lower nodule count than the chilled blocks (a). The surface in (b) shows evidence of compacted graphite. Image (c) was taken at an intermediate distance away from the chill and shows a very good microstructure. However, further away from the chill and spiky graphite forms, the nodule count falls and intercellular pearlite begins to appear (d).	96
Figure B.26:	High Si-N3. The presence of degenerate graphite continues as the distance from the chill increases (a). However, the pearlite is no longer present as it is in N1 (b).	96

List of Tables

Table 1.1	Specifications for EN1563: GJS-400-18-LT Standard	2
Table 2.1	Summary of alloying elements and their effects on graphite morphology and matrix microstructure.....	8
Table 2.2	Summary of microstructural features and their effects on impact toughness.	10
Table 3.1	Target alloy compositions for test heats	13
Table 3.2	Yields used in mass balance	13
Table 3.3	Table of materials, their source and their composition with regard to the 5 elements of interest	14
Table 3.4	Part numbers of resin used	14
Table 3.5	Procedure used to polish metallographic samples.	19
Table 3.6	Supplies and sources for polishing.....	20
Table 4.1	Tapping temperature and pouring time for each trial heat	22
Table 4.2	Summary of time to 400°C, baseline alloy.....	23
Table 4.3	Summary of time to 610°C, baseline alloy.....	23
Table 4.4	Time to 400°C, medium Si alloy.....	25
Table 4.5	Cooling times to 400°C, High Si alloy	27
Table 4.6	Summary of calculated cooling rates and interpolated cooling rates	29
Table 4.7	Final heat chemistries and their respective targets.	31
Table 4.10	Summary of impact energies and percent shear for Charpy impact testing	37
Table 4.11	Summary of hardness results	41
Table 5.1	Experimental hardness values and calculated values using equation in Donelan (2000)	52
Table A.1	Charge material chemistries and final melt chemistry for the baseline alloy.....	75
Table A.2	Charge material chemistries and final melt chemistry for the medium Si alloy	77
Table A.3	Charge material chemistries and final melt chemistry for the high Si alloy.....	79

Acknowledgements

I would like to extend a sincere thank you to everyone who has contributed to this project. To my advisor, Dr. Paul, for his guidance and answering every single one of my questions. To my fellow graduate students for assisting with molding, pouring, testing and use of equipment: Justin Clark, Nick Johnson, Joe Licavoli, Helen Ranck, and Karl Warsinski. To the MSE staff members Tom Wood and Nick Hendrickson for assisting with mechanical testing and especially Pat Quimby for helping with every aspect of molding, pouring and cutting. To Dan Young for doing all the heavy lifting. And to all the members of industry who have been supportive of university research by donating all the materials needed:

Gene Muratore, Rio Tinto
Mike Miklus, Youngstown Specialty Metal
Matt Liptak, Elkem Materials
Mark Adamovits, ASK Chemicals
Mark Beers, ASK Chemicals Metallurgy
Jerry Clancy, Fairmount Minerals
Joe Nowasad, ArcelorMittal
Jim Csonka, Hickman Williams
Allan Wilde and Gwen Baker, Waupaca

Additionally, I would like to thank URV USA, LLC for sponsoring this project.

Preface

Chill technology and the Power Chill™ casting process has been developed by Meehanite Worldwide Corporation together with URV Foundry in Finland. This technology is proprietary and thus its design is not disclosed in this thesis.

This thesis has been partially funded through the Center of Energy Excellence Grant awarded to URV USA, LLC from the State of Michigan.

Abstract

The effects of Si and cooling rate are investigated for their effect on the mechanical properties and microstructure. Three alloys were chosen with varying C and Si contents and an attempt to keep the remainder of the elements present constant. Within each heat, three test blocks were poured. Two blocks had chills - one with a fluid flowing through it to cool it (active chill) and one without the fluid (passive) - and the third block did not have a chill. Cooling curves were gathered and analyzed. The mechanical properties of the castings were correlated to the microstructure, cooling rate and Si content of each block. It was found that an increase in Si content increased the yield stress, tensile strength and hardness but decreased the impact toughness, elongation and Young's modulus. The fast cooling rates produced by the chills caused a high nodule count in the castings along with a fine ferrite grain size and a high degree of nodularity. The fine microstructures, in turn, increased the strength and ductile to brittle transition temperature (DBTT) of the castings. The fast cooling rate was not adequate to overcome the dramatic increase in DBTT that is caused by the addition of Si.

1 Introduction

1.1 The Wind Industry

The amount of energy that is generated via wind power is increasing. At the end of 2010, there was a total of 196,630MW installed capacity of wind turbines worldwide; this represents a growth of 23.6%, or a total of 37,642MW. The three top countries utilizing wind power are China (22.7%), the United States (20.4%) and Germany (13.8%). Worldwide, 670,700 people are employed, in one fashion or another, in the wind energy industry and it is forecast that a worldwide capacity of 600,000MW will be reached by 2015 (World Wind Energy Association 2011). Many wind turbines are located on land, but increasingly wind farms are being built off-shore. Additionally, there are designs for larger capacity generators, which lead to larger required castings. Together, these two issues pose interesting challenges to their design, manufacture and installation.

1.2 Structure and Design Requirements of Wind Turbine Generators

Wind turbines have four major components: the tower, nacelle, blades and blade hub. Within these components, many parts are made of ductile iron (DI). Figure 1.1 gives a view of a wind turbine generator with the important components labeled. Of these components, the hub, gear box housing and main shaft (both located within the nacelle), and support bases are all manufactured out of DI. It is not uncommon for section thickness of these castings to be upwards of 4 - 6in (100 - 150mm) and weigh in the tens of tons for a final casting weight. The nacelle at the top of the tower is the most complex component of the wind turbine. It houses the drive train, gearbox, generator and electronic components. It is within this structure that the kinetic energy of the rotating blades is transformed into electric energy.

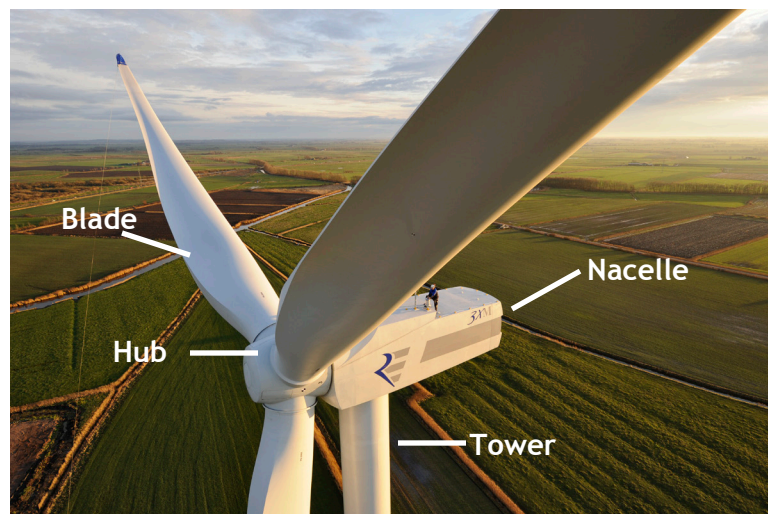


Figure 1.1: The top of a wind turbine generator showing the different components. (Image reprinted from Puttenat 2008).

All cast iron components must be strong and able to resist yielding under very large loading conditions, react to dynamic loads placed on them as well as oppose fatigue crack initiation. Typically, the design life of a wind turbine is 20 years. Material specifications of the DI call for a strong, tough and ductile material. In large section castings, this can be hard to achieve for a number of reasons which are discussed later.

1.3 Wind Turbine Generator Materials

Presently, there is a European standard that is used by many foundries and wind turbine OEMs that specifies the properties a material must have for different section thicknesses. The standard is EN1563: EN-GJS-400-18U-LT. The specifications are given in Table 1.1 (Standard:1563 2007).

As wind turbines get larger, the section sizes of critical components, such as the blade hub, need to increase in section thickness in order to obtain the strength required to support itself. However, with this increase in section thickness, a decline in the quality of material (strength, impact toughness, etc.) in the middle of the heavy section deteriorates. Therefore, by producing a high quality material, consistent in microstructure and mechanical properties across the section, the castings may be made with smaller section thicknesses. This results in lighter and stronger castings and will make the wind turbine more efficient.

Table 1.1
Specifications for EN1563: GJS-400-18-LT Standard

Property	Value
Minimum Tensile Strength	370MPa (54 ksi)
Minimum Yield Strength (0.2% offset)	240MPa (35 ksi)
Minimum Elongation	12%
Charpy Impact (min. mean, RT)	12J
Charpy Impact (min. individual, RT)	9J
Charpy Impact (min. mean, -20°C)	10J
Charpy Impact (min. individual, -20°C)	7J

2 Background

2.1 Alloying Elements and Their Effect on Mechanical Properties

The composition of DI plays a significant role in the mechanical properties of a final casting. DI is composed primarily of Fe, C and Si. Other elements commonly added or present in DI include Mg, P, S, Ni, Mn, Cr, Mo, Sn, Ti, Cu and Ce. These are discussed in detail below.

2.1.1 Carbon

Carbon is the primary alloying element present in DI. It serves to form nodules which act as “crack-arresters.” As the C content increases, the upper shelf energy of notched charpy impact tests decreases (Ductile Iron Society 1990). Additionally, if the C content is high, it is possible for a large amount of primary graphite to precipitate out of the melt and grow to a size which allows it to float to the top of the solidifying casting. This is termed C flotation and is considered to be a degenerate form of graphite within the structure (Riposan 2010). In Labrecque (2010), it is also noted that as C levels increase, so does the risk of all forms of degenerate graphite.

2.1.2 Silicon

Silicon, another primary alloying element in DI, is a strong ferrite promoter and graphitizer. At high levels, it is generally considered to be detrimental - especially with respect to the ductile to brittle transition temperature (DBTT), as shown in Figure 2.1 (Ductile Iron Society 1990). In cases when strength is preferred, an increase in Si content increases proof stress, hardness and tensile strength. Conversely, though, an increase in Si increases the DBTT, thus decreasing impact toughness. Therefore, for materials in which it is important to maintain high impact toughness at low temperatures, the Si content is kept as low as possible to still retain a ferrite matrix, but avoid the increase in DBTT.

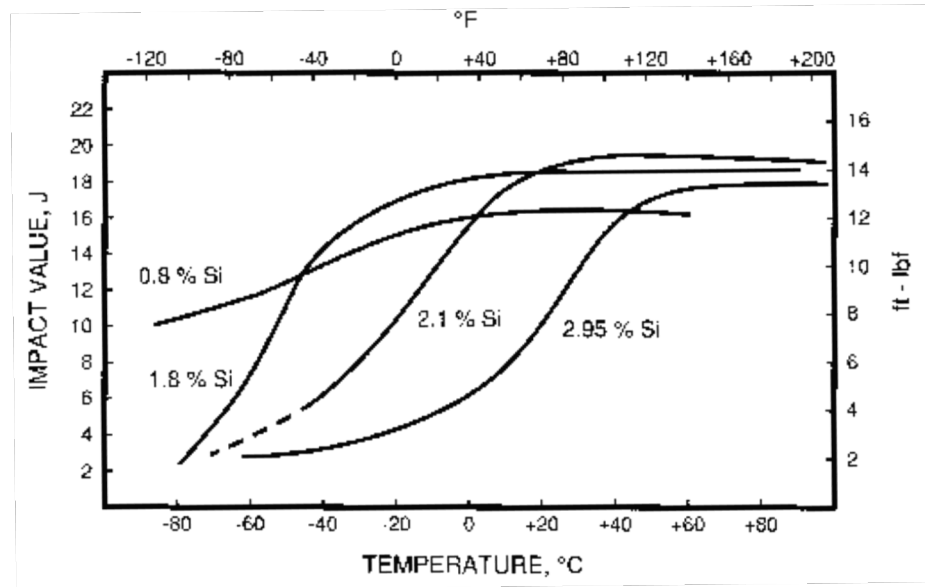


Figure 2.1: Graph showing the effects of temperature on impact toughness. Note that the DBTT increases for increasing amounts of Si. (Image reprinted from Ductile Iron Society 1990)

2.1.3 Carbon Equivalent

The eutectic composition of DI has a carbon equivalent (CE) equal to 4.3. However, most ductile irons maintain a CE anywhere between 4.2 and 4.5. Carbon equivalent can be calculated using equation 2.1, given in the Metals Handbook published by ASM. The literature indicates that for a higher CE iron, the nodules are more compact and less irregular in shape. However, the higher CE irons also have a higher likelihood of exhibiting carbon flotation - a phenomenon in which the graphite nodules grow large enough to float to the top of the melt. In addition, chunky graphite is more prevalent in irons with a CE greater than 4.3 (Hoover 1986).

$$CE = \%C + \frac{\%Si + \%P}{3} \quad \text{eq. (2.1)}$$

It should be noted, that for DI to have a sufficient nodule count, it is important that the CE be kept close to the eutectic composition or slightly higher. This is dictated by the graphite nucleation and growth that occurs in eutectic and hypereutectic ductile irons. Ideally, in eutectic iron, once the melt reaches the eutectic temperature, the graphite and austenite nucleate simultaneously. In hypereutectic iron, primary graphite nodules nucleate first and grow in the liquid, thus depleting it of C until the concentration reaches the eutectic

composition. At that point, the eutectic reaction takes place and secondary nodules are nucleated along with austenite.

2.1.4 Magnesium

Magnesium, in addition to some rare earth (RE) elements, is commonly used as the nodularizing agent. The magnesium - usually in the form of FeMgSi or NiMg alloys - reacts violently with the liquid iron, effectively “cleans” the melt of excess oxides and combines with sulfur to form MgS, which acts as a nucleation site for the graphite nodules. It changes the surface energy of the graphite allowing it to precipitate in nodules as opposed to flakes. Its presence in the melt fades with time so it is important to pour soon after the nodularizing reaction is complete.

Excessive Mg can be detrimental to a casting. It is well documented in the literature that high levels of residual Mg can lead to the formation of degenerate graphite - especially crab graphite - as well as carbides and dross defects. Mg is one of the strongest carbide promoters (Ecob 2011). It can also encourage porosity and shrinkage. However, a Mg content that is too low can result in compacted graphite to form (Hughes 1988)

2.1.5 Phosphorous

The presence of P is generally considered to be an impurity in the casting. It segregates to the grain boundaries and forms phosphides and promotes pearlite (Riposan 2010). It raises the DBTT and embrittles the matrix (Marks 1999). These effects are more pronounced at levels greater than 0.005wt%.

2.1.6 Sulfur

The presence of S in the melt is detrimental to material properties and is to be kept as low as possible. During the Mg treatment, the S often combines with Mg and form MgS which either forms slag or acts as nucleation sites for graphite nodules. If present in large quantities in the mold (sand), S can cause flake graphite at the casting surface to form (Goodrich 1997). S can be reduced by performing a de-sulfurization treatment. CaCO_3 (limestone) and CaC_2 are two common materials used to do this. Alternatively, if Ce is added to the metal, higher concentrations of S may be tolerated (Hughes 1988).

2.1.7 Nickel

Although a stronger pearlite stabilizer than Cu, Ni is preferred as a ferrite strengthener over Cu since it does not have as dramatic effect on increasing the DBTT. Where Cu increases the DBTT by 45°C for a 1% addition, Ni only increases it by 10°C for the same addition rate (Ductile Iron Society 1990). It is

usually added with the Mg in the form of NiMg as the nodularizing agent. Ni can also be helpful for obtaining high strength and ductility in the as-cast state when doing so has proven difficult (Riposan 2010). Additionally, Ni is a mild graphitizer (Hayrynen 1988).

2.1.8 Carbide and Pearlite Promoters

A number of elements are known to promote carbides and pearlite in heavy section DI. Among these are Mn, Cr, Mo, Sn, Ti and Cu (Ductile Iron Society 1990; Marks 1999; Riposan 2010). These are typically considered to be detrimental to the production of heavy section DI. Pearlite and carbides produce microstructures that are harder and stronger therefore reducing the ductility and impact toughness of the castings. The effects of these and other subversive elements are cumulative and the effects are exacerbated in heavy section castings (Marks 1999). Many of the effects of these subversive elements may be reduced or eliminated by the addition of Ce (Hughes 1988).

Manganese is usually a residual element from the use of scrap steel in the charge mixture. It segregates to the grain boundaries and the last to freeze areas forming pearlite and carbides, especially in heavy sections (Cho 2007). It also increases the DBTT thus decreasing the impact toughness of the material (Gilbert 1970). However, there are studies that show increasing the Mn content from 0.07wt% to 0.20wt% actually decreases the occurrence of chunky graphite (CHG) in heavy sections (Thrury 1977). Mn levels are diluted by adding high purity pig iron to the charge. The presence of Mn must be balanced so as to minimize the risk of CHG, but not increase the DBTT unnecessarily.

Molybdenum strengthens pearlite in the as-cast condition (Hayrynen 1988). While this is good for applications in which strength is preferred, it is detrimental to the impact toughness of the material and should be avoided in heavy section castings where toughness is an important mechanical property.

In addition to promoting pearlite, Sn also promotes the formation of crab graphite (Hayrynen 1988). Since degenerate graphite is detrimental to impact toughness and other mechanical properties, it is important to minimize the amount of Sn added. Some sources indicate that low levels of Sn may be beneficial, however. It was found that an addition rate of 0.05wt% prevented the formation of CHG in an as-cast 10in (254mm) cube when the maximum Si level 2.5wt% (Karsay 1970)

It is well documented in the literature that Ti is a pearlite and carbide promoter and can even promote degenerate forms of graphite. It is also an anti-spheroidizing element and has a chilling effect on iron in thin sections (Shy

2000). Sometimes it is intentionally added, along with Mg, to form compacted graphite iron.

Copper is a grain refiner and can be used to strengthen low Si ferrite, but it dramatically increases the DBTT (Ductile Iron Society 1990). It is also considered to be a pearlite promoter (Marks 1999). While it is also a mild graphitizer, it increases the negative effects of other subversive elements that may be present (Hayrynen 1988).

2.1.9 Cerium

Cerium is another element that may act as a nodularizer in DI. Its presence also neutralizes the deleterious effects of subversive elements that may be present from charge materials (Marks 1999). If the charge is exceptionally pure with very few subversive elements present, the presence of excess Ce may actually be harmful because it promotes degenerate graphite formation (Hughes 1988).

From the above discussion, it can be seen that the presence of some alloying elements are beneficial to DI production while others need to be strictly controlled due to their deleterious effects on the castings.

Table 2.1 on page 8 provides a summary of the elements discussed above.

2.2 Effect of Microstructure on Toughness

There are three main features that affect the impact toughness and other mechanical properties in DI. These are nodule count, nodularity and matrix microstructure. Each of these is discussed in more detail below.

2.2.1 Nodule Count

One of the largest factors for improving toughness in DI is the nodule count. In order for an acceptable microstructure to be obtained, the nodule count must be kept above 60 nodules/mm². Listed below are some of the benefits associated with a high nodule count.

- Finer segregation. This thus results in a decrease in pearlite and carbides at the grain boundaries (Labrecque 2011)
- The DBTT is shifted to a lower temperature (Labrecque 2011)
- The occurrence of degenerate forms of graphite are reduced (Basutkare 2007)
- The percent pearlite is decreased, the tensile strength increases, and the ductility increases due to a reduction in the presence of carbide. A more homogenous and finer microstructure are also produced (Ductile Iron Society 1990)

However, it is important to note that the nodule count can be too high and can be detrimental to the properties of a casting. For example, an excessively high nodule count decreases the upper shelf energy of impact strength (Labrecque 2011). Riposan (2010) also recommends keeping the nodule count below 300 nodules/mm².

Table 2.1
Summary of alloying elements and their effects on graphite morphology and matrix microstructure

Element	Pearlite Stabilizer	Carbide Promoter	Nodulizer	Graphitizer	Ferrite Promoter	Comments
Si				✓	✓	Strong graphitizer; Can increase DBTT; Reduces occurrence of chunky graphite
Mg			✓			Strong nodularizer, fades quickly; Excess amounts can promote carbides, crab graphite and shrinkage; Too little present and compacted graphite is formed
P	✓					Strong pearlite stabilizer; Segregates to grain boundaries and forms brittle phosphides; increases DBTT
S						Excessive amounts can form dross defects and other degenerate forms of graphite
Ni	✓			✓		Mild graphitizer; Can be used to strengthen ferrite
Mn	✓	✓				Strong pearlite stabilizer; Can produce undesirable microsegregation
Cr	✓	✓				
Mo	✓	✓				Strengthens pearlite
Sn	✓					Promotes formation of crab graphite
Ti	✓	✓				Strong pearlite and carbide stabilizer; Has anti-spheroidizing effect
Cu	✓			✓		Mild graphitizer; Dramatically increases DBTT; Can increase effects of other subversive elements
Ce			✓			Can reduce effects of subversive elements; Will promote degenerate graphite in chemically pure heavy sections

2.2.2 Nodularity

In addition to nodule count, nodularity is also an important factor. Although there are some sources that indicate that nodularity is not as crucial a factor as nodule count (Labrecque 2011), others indicate that nodularity should be at or above 90% since poorly formed nodules can act as stress concentrators (Khajure 2010). One way to improve the nodularity of the casting is to add REs at a rate of 1.0 - 1.5 times the amount of subversive elements. Ce, especially, is helpful in neutralizing their effects. It should be noted, that although there are standards in place, that there is no universally agreed-upon method for determining nodularity in DI. For the purposes of this study, ASTM standard E2567-11 was used and is discussed later, in section 3.6.1.

In addition to nodules, there are many forms of degenerate graphite that may form. These include chunky, exploded, compacted, flake and spiky graphite. Of these, chunky graphite is the most common in heavy sections. Chunky graphite is usually the result of high concentrations of subversive elements. This can be corrected with additions of Ce or other REs. However, if REs are added to a melt which is relatively free of trace elements, they may promote chunky graphite (Riposan 2010). The presence of chunky and other forms of degenerate graphite result in a dramatic reduction in elongation and impact properties of a casting. Many of these can be controlled by careful monitoring of trace elements and appropriate additions of REs.

2.2.3 Microstructure Matrix

Another major contributing factor to mechanical properties in DI is the matrix structure. DI is classified in four ways:

- Ferritic
- Ferritic/Pearlitic
- Pearlitic/Ferritic
- Pearlitic

Ferritic matrices are soft, not very strong, ductile and tough. The increasing amount of pearlite increases the hardness and strength of the castings; however, pearlite is a very hard and brittle phase which decreases the ductility and impact toughness of the material. The presence of pearlite also increases the DBTT (Hughes 1988). Just as in steels, the fineness of the microstructure also contributes to the mechanical properties. A finer structure decreases the presence of undesirable carbides. This results in an increase in strength and a decrease in DBTT (Gilbert 1970). Additionally, the amount of ferrite may be increased with an increase in nodule count. The presence of carbides, especially at grain boundaries, decreases the impact toughness and ductility while increasing hardness. This occurs more readily in heavy sections due to

the slow cooling rate. For wind turbines, this is detrimental and should be avoided.

These features present in the casting microstructure all play important roles in determining the impact toughness of the material. Table 2.2 below summarizes their effects.

Table 2.2
Summary of microstructural features and their effects on impact toughness.

Feature	Effect	Impact on Toughness
Nodule Count	High nodule count can decrease DBTT	Increase
	High nodule count leads to finer, more homogenous microstructure	Increase
	Too high and the upper shelf energy can be reduced	No Effect
	Too low and large nodules form	Decrease
Nodularity	High nodularity (poorly formed nodules can act as stress concentrators)	Increase
Matrix	Ferrite is ductile, but also tough	Increase
	As pearlite:ferrite ratio increases, DBTT increases	Decrease
	Fine matrix (small ferrite grain size)	Increase
Degenerate Graphite	Chunky, exploded, compacted, flake and spiky graphite forms	Decrease

2.3 Effect of Solidification Rate and Segregation on Toughness

Solidification rate plays a large role in determining the microstructure of a DI casting. DI solidifies in the following manner:

- Temperature drops below graphite liquidus - with significant undercooling, primary graphite nodules form
- As the casting cools further and reaches the eutectic temperature, austenite dendrites begin to form around the nodules. Secondary nodules then form, along with austenite shells surrounding them. The austenite allows C to diffuse from the liquid into the graphite allowing the nodule to grow in size.
- With further cooling, the austenite phase grows, rejecting carbide promoters into the liquid.
- Upon further cooling of the casting, the austenite transforms into either ferrite or ferrite + pearlite, depending on composition and cooling rate, in a eutectoid reaction

In general, the faster the cooling rate, the higher the nodule count, the smaller the nodules and the finer the microstructure. It was also found that a high

cooling rate increased the degree of nodularity in heavy sections (Helmink 1977). As the cooling rate decreases, as in the thermal centers of heavy sections, the nodule count decreases, the nodules grow larger and the degree of segregation increases. A large degree of segregation is especially detrimental since it is the carbide and pearlite forming elements that are rejected into the liquid. They then form carbides and pearlite at the grain boundaries (Riposan 2010).

According to Sprengler (1995), sections that had a solidification time of longer than 90 minutes experienced a decrease in mechanical properties. They also found that longer solidification times resulted in grain boundary segregation in the form of carbides and that solidification time had a significant impact on both nodule shape and nodule size. When the solidification and cooling rates were controlled, mainly with the application of chills, a positive effect on mechanical properties was achieved (Nakamura 1989).

2.4 Hypotheses

2.4.1 Effect of Material Chemistry on Microstructure and Toughness

Material chemistry has a large impact on the microstructure and, hence, toughness of a material. In general, the more alloying elements that are present, the more complicated the microstructure. As a result, it is important to keep the castings as pure as possible - meaning that the alloy is comprised of mainly iron, carbon and silicon with very low amounts of other alloying elements. It is expected that by maintaining a high concentration of ferrite-stabilizing elements (C, Si) and minimizing pearlite-stabilizing elements (Mn, Sn, Cu, etc.) and other subversive elements, a fully or mostly ferritic matrix will be produced. This matrix will ensure toughness in the material while the presence of Si and residual tramp elements will increase its strength. There appears to be a lack of information in the literature regarding the Si concentrations investigated in this study with many values not exceeding 2.8wt%.

Hypothesis 1: The increase in Si content in the matrix will decrease the impact toughness of the material as well as strengthening the ferritic matrix of the castings.

2.4.2 Effect of Cooling Rate on Segregation and Toughness

One of the primary considerations of this study is to investigate the cooling rate. Three cooling rates were investigated:

- Fast - achieved using a chill actively cooled with a flowing fluid
- Medium - a chill with no flowing fluid of the same size and shape
- Slow - no chill present

It is expected that the use of the chills will dramatically reduce the amount of time for the casting to reach a shakeout temperature of 400°C (752°F). This fast cooling rate will not allow for a large degree of segregation in the chilled castings thus producing a fine ferritic microstructure that is tough.

Hypothesis 2: The increase in cooling rate will redistribute the segregation so that it is more uniform in the casting and create a much finer microstructures (smaller ferrite grain size, smaller graphite nodules, high nodule count) leading to an increase in impact toughness.

3 Experimental Procedure

3.1 Selection and Determination of Alloys and Charge Mix

The alloy compositions were suggested by URV USA, LLC, the sponsor of the present study. Table 3.1 shows the 3 alloys of interest to them.

Each charge consisted of a mix of pig iron, steel, DI returns, and/or graphite as well as any required alloying additions. A mass balance, found in Appendix A, was performed in Microsoft Excel to determine the charge mixture required to obtain the specified chemical composition. The yields listed in Table 3.2 were used to help determine the charge mix and were determined from a combination of experience and results of previous heats poured. Note that although a sulfur yield is listed, this is not a true yield since S is not added to the melt and is a result of residuals in the charge material. Rather, this is used to determine the final S content after the Mg reaction. A list of materials with their compositions regarding the above 5 elements are shown in Table 3.3. Only elements that were provided in the certificate of analysis are included in the table. In the case of the Germalloy, the nominal analysis is provided.

Table 3.1
Target alloy compositions for test heats

Alloy	Primary Elements (all are in wt%)						
	C	Si	Mg	Mn	P	S	CE
Baseline	3.7	2	0.039	0.18	0.025	0.005	4.38
Medium Si	3.2	3.65	0.045	0.28	0.025	0.005	4.43
High Si	3.05	4.25	0.045	0.28	0.025	0.005	4.48

Table 3.2
Yields used in mass balance

Element	Yield
C	90%
Si	90%
Mg	60%
S	50%

Table 3.3
Table of materials, their source and their composition with regard to the 5 elements of interest

Material	Source	C	Si	Mg	P	Mn	S
Steel	Youngstown Specialty Metals	0.003	0.006	0.001	0.009	0.14	0.014
Pig Iron - Sorel	Rio Tinto via Grede Foundry	4.26	0.18		0.01	0.005	0.012
Graphite	Superior Graphite	99.7					0.03
FeMn	Vanadium Corporation of America	6.72				75.1	
DI Returns - Large	Waupaca	3.76	2.4		0.017	0.33	0.005
DI Returns - Small	Waupaca	3.74	2.4		0.015	0.28	0.005
Foundrisil	Elkem Materials		74.9				
Mg Treatment	Elkem Materials		44.4	5.55			
Foundrisil	Elkem Materials		74.9				
Ultraseed	Elkem Materials		74.4				
Germalloy	ASK Chemicals		78.0				

3.2 Mold Preparation

The molds were prepared using chemically bonded sand. PEP-SET-X resin, supplied by ASK chemicals, was used as the binder. PEP-SET-X resin is a three part resin system. The part numbers for the three parts are given below in Table 3.4. The catalyst was mixed in with Part I at a rate of 6% by weight batch wise. The resin was mixed in a ratio of 55 parts Part I and catalyst to 45 parts Part II. The total resin was added with sand at an addition rate of 1.25% by weight.

Table 3.4
Part numbers of resin used

Resin Component	Part Number
Part I	162400
Part II	32865
Catalyst	121415

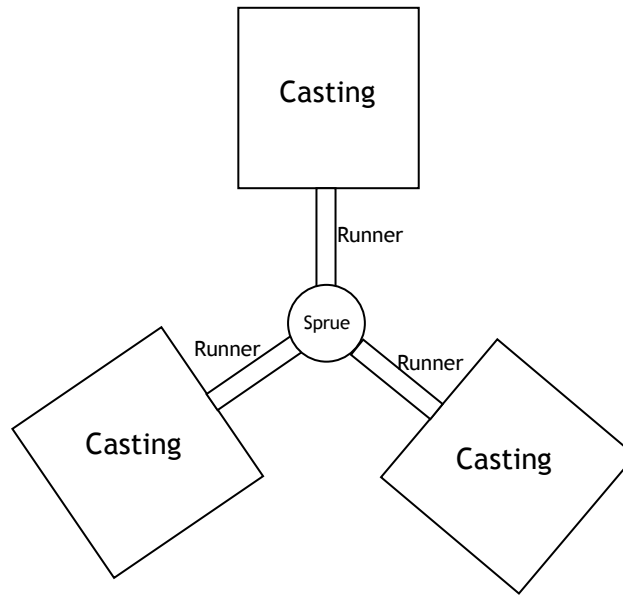


Figure 3.1: Schematic showing the pattern that was cast. The sprue is in the center with three runners leading to the three blocks. The sprue area:runner area:gate area is 1:2.7:2.7

Three blocks, 7" x 7" x 6.4" (180mm x 180mm by 165mm) were equilaterally spaced and connected to the sprue using runners. They were arranged in a triangle fashion and molded in a hexagonal wooden flask. The sprue:runner:gate area ratio was 1:2.7:2.7. Figure 3.1 below shows a schematic on how the pattern was oriented.

The flask was composed to two parts - the drag, or bottom, and the cope, or top. The drag contained two Powerchills, supplied by URV, and the sprue basin. Each Powerchill was manufactured out of gray iron and measures 11.5in wide by 11in tall (28cm x 30cm) and 4in (10cm) thick at the bottom and 4.25in (11cm) thick at the top. They have a weight of 135lbs (60kg) giving a chill to casting weight ratio of 3:2. This is a large ratio and in practice will be much smaller. However, due the melting capabilities in the foundry, this ratio was unavoidable. The drag was filled upside down on top of a wooden pallet and a screed was used to ensure planeness of the sand. Once the resin had cured, a steel baseplate was placed on the drag and the whole assembly was clamped together. The drag was then flipped over using an overhead crane. Once flipped, a wooden match plate was placed on the drag. The blocks, runners and sprue were placed in the correct locations within the cope. Thermocouples were also placed in the tops of the blocks as well as coming out from the two outside corners of the blocks. The thermocouples in the tops of the blocks were placed there to leave an area for thermocouples to be inserted into the casting to record cooling rates during solidification. The outside corners had thermocouples placed there to create vents for the gases produced during pouring to escape. The cope was then filled and allowed to cure. In-

mold inoculation was utilized by printing Germalloy pellets in the pouring basin. Figure 3.2 shows the molding process. Thermocouples were then bundled four at a time as in Figure 3.2(b) and placed in the mold such that they measured the temperature at the following distances from the chill/casting interface: 0mm (0 in.), 40mm (1.6in.), 80mm (3.1in.) and 120mm (4.7in.).

3.3 Melting and Solidification

All melting was completed in the MTU foundry using a 300lb (136kg) Inductotherm coreless induction furnace. The pig iron and DI returns were melted first along with any ferrosilicon, graphite or other alloying additions. The steel was melted last. Each heat was de-slagged with limestone and spectro buttons for chemical analysis were taken before and after the treatment. The melt was de-slagged when the temperature reached 2660°F (1460°C) and then tapped into a preheated tundish. The magnesium treatment was carried out using the sandwich method in the tundish. Treatment material with a mesh size of ¼" to ½" (6 - 13mm) was added to the bottom of the

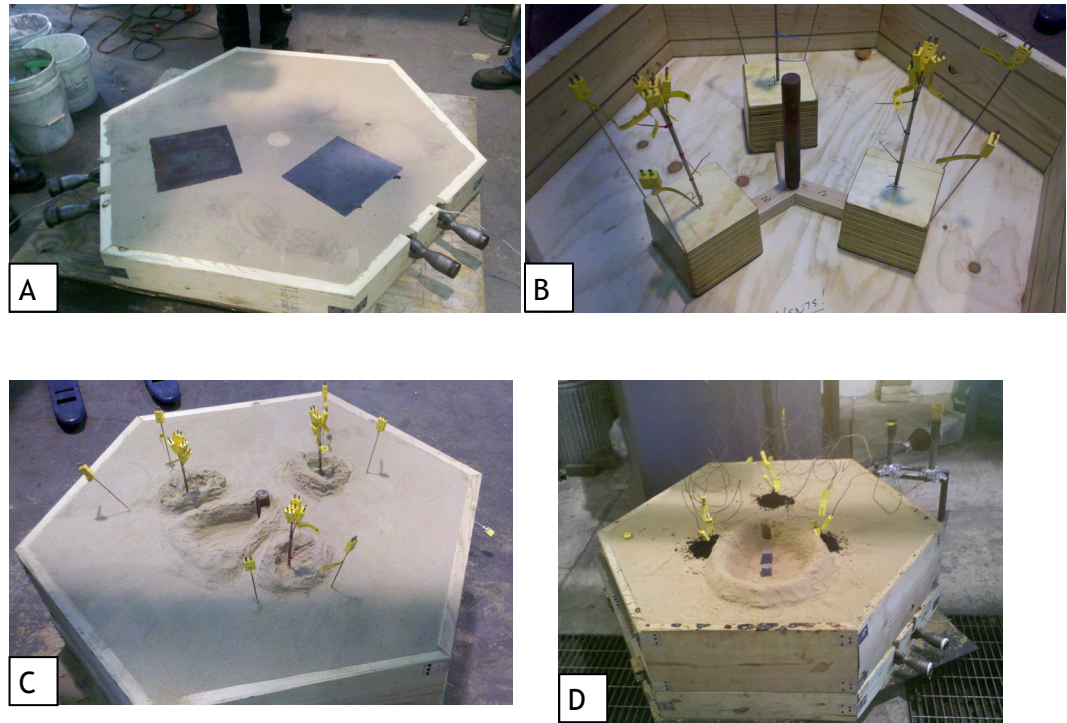


Figure 3.2: Series of images showing molding process. In (a), the drag is in its proper orientation after being filled and flipped. The placement of the pattern with place holder thermocouples in place is shown in (b). The completed cope is pictured in (c) and (d) shows the entire mold ready for a pour. The Germalloy has been printed in the pouring basin in (d)

tundish and covered with ferrosilicon. Once the Mg reaction was completed, a cooling cup and spectral button sample were taken and the remainder of the material poured into the mold.

After the mold was filled, the fluid was allowed to flow through the active chill. The thermocouple readings were monitored and when the temperature of the thermocouple at 0mm reached 750°C, the fluid was turned off. This slowed the cooling rate during the eutectoid reaction and was requested by the sponsors. The fluid was turned on again when the same thermocouple read 650°C.

3.4 Sample Preparation

Once the castings were cooled to below 400°C (750°F), they were removed from the mold, again with the aid of an overhead crane. Five slices were then cut from the blocks parallel to the chill/casting interface. Metallography, Auger, tensile and Charpy samples were taken out of the first, third and fifth slices. Figure 3.3 shows the schematic for taking samples.

Samples were labeled with 3 identifiers. The first was a number, indicating which heat the sample is from - either 4, 5 or 6 which were the Medium Si, Baseline and High Si alloys, respectively. The second was a letter - A, P or N - which indicated the type of chill used (active, passive or none, respectively). Finally, the last was a number indicating which slice in the block the sample was from - either 1, 3, or 5 - see Figure 3.3 for slice locations. For example, sample 6A3 would indicate that it was from heat 6 (High Si alloy), was actively chilled and was from the 3rd slice taken from the block.

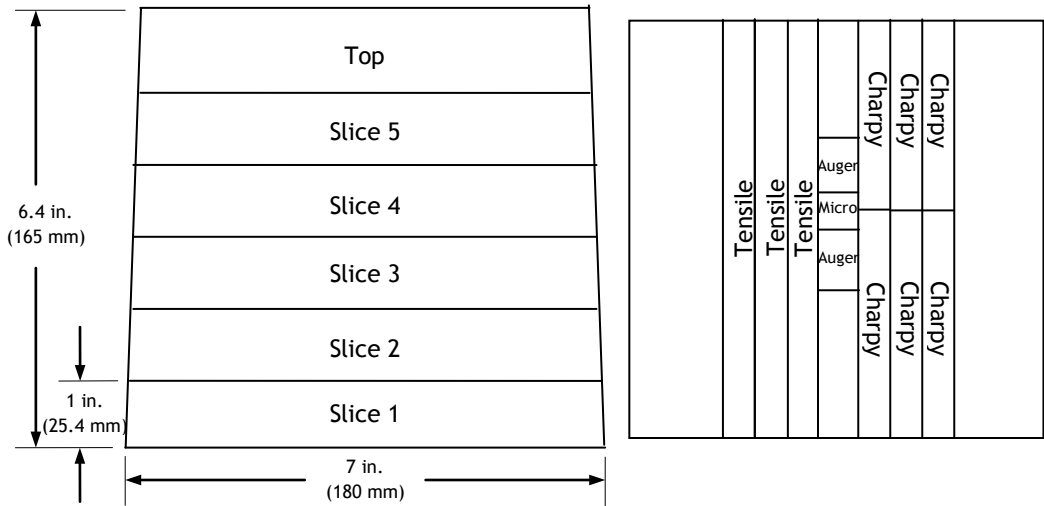


Figure 3.3: Schematics for slice location (left) and sample locations in each slice (right).

3.5 Chemical Analysis

Samples were sent to Waupaca's Ductile Iron Plant 4 in Marinette, WI for chemical analysis. Analysis was performed on a Fisons ARL-3460 Optical Emission Spectrometer. The following samples were obtained for analysis:

- Spectral button before de-slagging (above 2660° F (1460° C))
- Spectral button after de-slagging, before Mg treatment
- Spectral button after Mg treatment
- Runner section after pouring and shakeout

It was necessary to re-melt and chill cast the samples from the runners. Each sample was ground down to remove any oxides or other contaminants present on the surface.

3.6 Metallography

Samples were taken from the slices 1, 3 and 5 as indicated in Figure 3.3. They were mounted in epoxy such that the cross section was perpendicular to the Powerchill (see Figure 3.4), allowing for a gradient in nodules or microstructure to show, if one existed. When polishing DI, it is important to minimize the potential pull out of the graphite nodules. This was accomplished by using as few polishing steps as possible, as suggested by Radzikowska (2009), and using high pressure during the procedure. Additional information in the literature suggested a napless cloth with diamond paste for polishing since this would minimize graphite pull-out and using Nital to etch the surface (Radzikowska 2009). The procedure outlined in Table 3.5 yielded good results when polished on a Leco AP-300 autopolisher. A list of polishing consumables and their sources may be found in Table 3.6.

3.6.1 Nodularity

All nodularity ratings and nodule counts were determined using PAX-it! software. First, a roundness value was calculated using equation 3.1 on photomicrographs of the as-polished samples. This roundness value is based on the ASTM shape factor given in ASTM standard E2567-11.

$$\text{Roundness} = \frac{\text{Area of Particle}}{\text{Area of Equivalent Circle}} \quad \text{eq. (3.1)}$$

A cut off roundness value of 50% was chosen, per the standard, and any particle that had a roundness value above 50% was considered to be a nodule.

Nodularity was then calculated as a ratio of particles with a roundness value greater than 50% to the total number of particles. An average of 7 - 10 images per sample were used in nodularity calculations. Any nodules below 5 microns were not used in the calculations.

Table 3.5
Procedure used to polish metallographic samples.

Grit	Time	Pressure	RPM
60	Until Plane	40psi	300
240	60 sec	40psi	300
600	60 sec	40psi	300
1200	45 sec	30psi	150
1 micron diamond	5 min	30psi	150

3.6.2 Microstructure

The microstructure was determined by analyzing the samples after being etched with 4% nital. Photomicrographs of representative areas as well as unique features were taken. Figure 3.2 shows, schematically, where the samples were taken from and how they were mounted. From these samples, nodularity and nodule count were determined as well as matrix microstructure. Vickers hardness testing was also performed on the same samples.

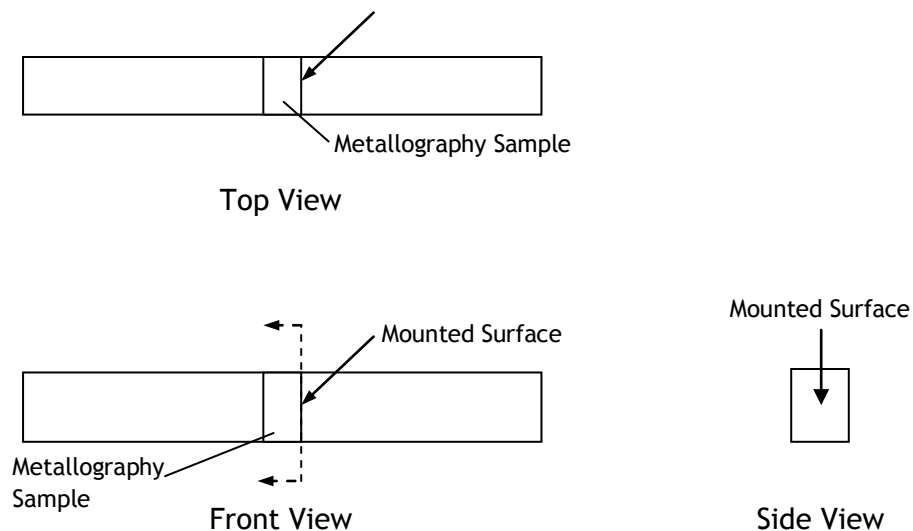


Figure 3.4: Sectional view of section where metallography sample was taken from. Note that the mounted surface is perpendicular to the chill direction.

Mounted Surface

Table 3.6
Supplies and sources for polishing

Material	Source
Epoxy	AeroMarine: Resin #300, Hardener #21
60, 600 Grit SiC Paper	Leco
240 Grit SiC Paper	McMaster-Carr
800 Grit SiC, 1µm Diamond	Pace Technologies

3.7 Mechanical Testing

Three types of mechanical testing were performed on the cast samples: tensile, notched Charpy impact and Vickers microhardness testing.

Tensile testing and Vickers microhardness were completed at MTU. The tensile testing was performed on an Instron 4201. It is a screw-driven frame and a strain rate of $3(10^{-4})/\text{sec}$ was used. An extensometer was attached to the sample to record the elongation. Three samples per slice, for a total of 9 samples per block, were tested at room temperature until failure. Vickers microhardness was performed on the metallographic samples previously prepared, taking care to avoid graphite nodules. A Leco M-400-G1 hardness tester was used. A 500g load was applied for 15 seconds on the heat 5 samples while a 1000g load, also applied for 15 seconds, was used on the samples from heats 4 and 6. A total of 5 tests were performed on each sample and averaged.

Young's modulus of the material was tested ultrasonically. The longitudinal and transverse wave frequency and time to travel thorough the material were measured. From this, the speed was calculated and used to calculate Poisson's ratio using equation 3.2. Young's modulus was then calculated from Poisson's ratio using equation 3.3. In the equations, v_T and v_L are the transverse and longitudinal velocities, respectively and ρ is the density of the material.

$$\nu = \frac{1 - 2\left(\frac{v_T}{v_L}\right)^2}{2 - 2\left(\frac{v_T}{v_L}\right)^2} \quad \text{eq. (3.2)}$$

$$E_y = \frac{\nu_L * \rho * (1 + \nu)(1 - 2\nu)}{1 - \nu} \quad \text{eq. (3.3)}$$

Charpy impact testing was performed at Stork Climax research lab located in Livonia, MI. Three temperatures - room temperature, -20°C, and -40°C - were chosen for testing. This allowed ductile and brittle fracture to occur as well as construction of an Impact Energy vs. Temperature curve to determine the DBTT of each casting.

4 Experimental Results

4.1 Pouring Results

The target tapping temperature range for the heats poured was 2660°F - 2678°F (1460°C - 1470°C) and was recommended by the sponsor. In order for the Germalloy pellets to fully dissolve and inoculate all iron, the pouring time needed to be around 20 seconds. Table 4.1 summarizes the experimental results of pouring.

Table 4.1
Tapping temperature and pouring time for each trial heat

Heat	Alloy	Tapping Temp.	Pouring Time
H110419	Baseline	2655°F (1457°C)	25 sec.
H110413	Medium Si	2658°F (1459°C)	31 sec.
H110504	High Si	2646°F (1452°C)	24 sec.

4.2 Cooling Curves

Cooling curves were collected from the thermocouples inserted into the mold prior to pouring. Temperature profiles were obtained for the following thermocouples:

- 0mm, 40mm, 80mm and 120mm from the chill/casting interface for each block (total of 12)
- Chill temperature 20mm below the surface for each chill (total of 2)
- Fluid in and out (total of 2)
- Cooling cup

This gave a total of 17 thermocouples per heat. Additionally, it was important to the sponsor to know the time to 400°C, the temperature at which they shake out their castings. For each heat, this temperature was recorded and is summarized in Table 4.2 through Table 4.5.

4.2.1 Baseline

The cooling curves for the three blocks from heat 5 are show in Figure 4.4 - 4.3. While recording data, the computer restarted and therefore, the cooling time to 400°C is not complete. However, in the absence of that data, the time to the lowest temperature recorded on the no chill block may be analyzed.

This temperature was 610°C, below the end of the eutectoid reaction. Table 4.3 shows the results of the cooling times from the three blocks.

Table 4.2
Summary of time to 400°C, baseline alloy

Chill Type	Time to 400°C	
	Sec.	Hours
Active	15160	4.21
Passive	19940	5.54
None	n/a	n/a

Table 4.3
Summary of time to 610°C, baseline alloy

Chill Type	Time to 610°C	
	Sec.	Hours
Active	7494	2.08
Passive	7814	2.17
None	22299	6.19

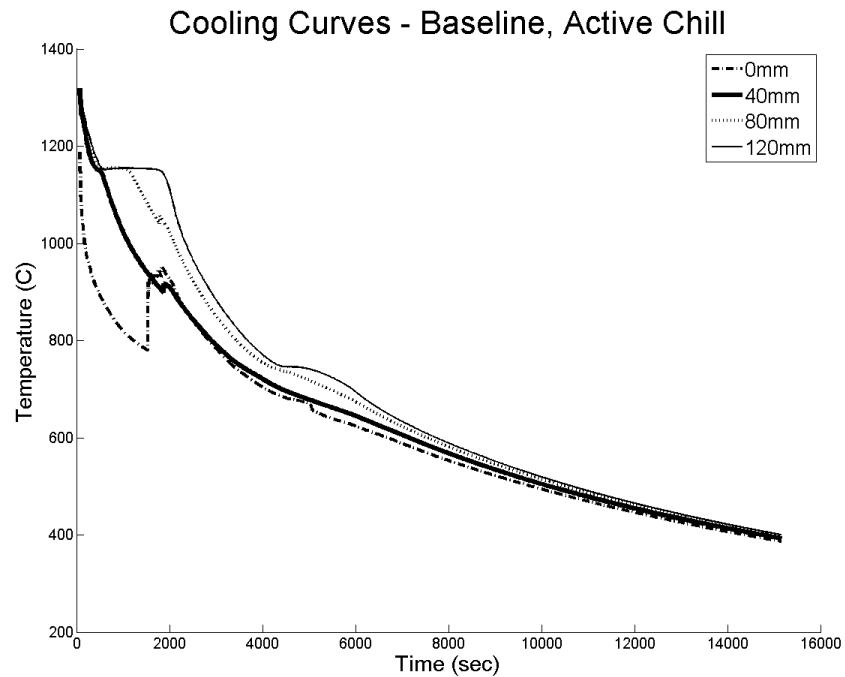


Figure 4.1: Cooling curve for the baseline alloy, actively chilled block. The eutectic arrest at the 120mm thermocouple occurred at 1154°C and the eutectoid arrest occurred at 746°C. The recalescence in the 0mm thermocouple is 161°C and decreases with increasing distance from the chill

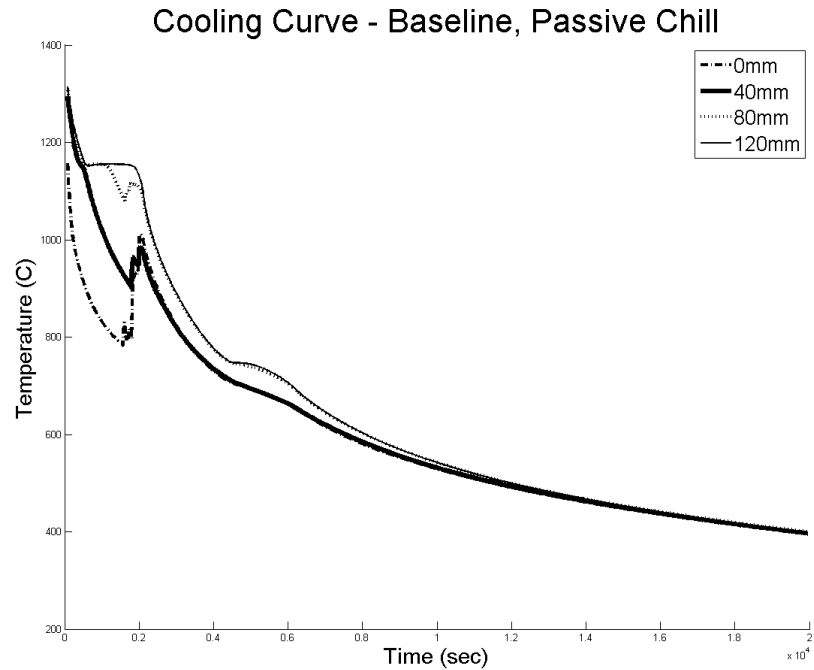


Figure 4.2: Cooling curve for baseline alloy, passively chilled block. The eutectic arrest in the 120mm thermocouple occurred at 1155°C and the eutectoid occurred at 746°C. The recalescence in the 0mm thermocouple is 220°C.

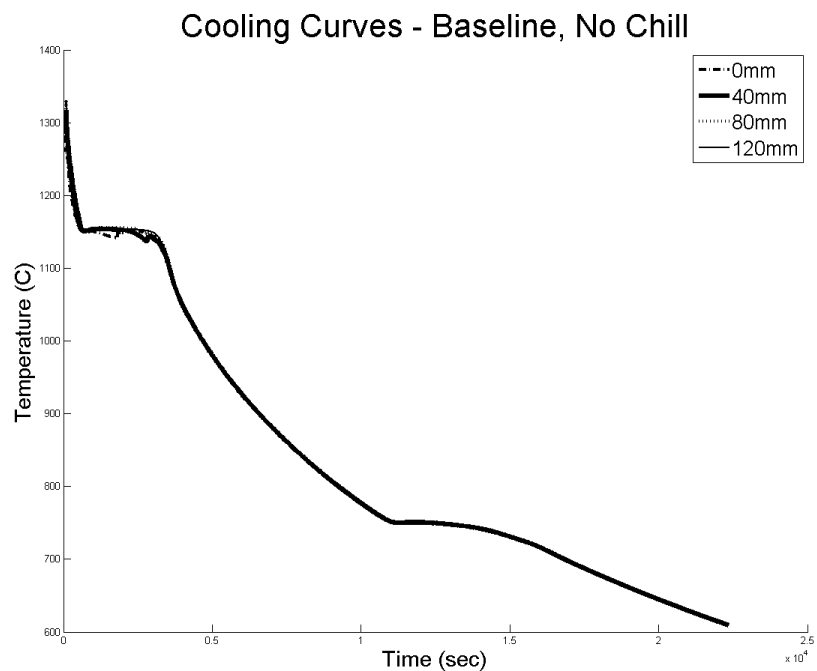


Figure 4.3: Cooling curve for baseline, non-chilled block. There was not a large difference in cooling between the thermocouples. The eutectic arrest occurred at 1154°C and the eutectoid occurred at 750°C.

4.2.2 Medium Si

Figure 4.4 through Figure 4.6 show the cooling curves for each block cast in heat 4. The data recording was turned on approximately 5 minutes after pouring. As a result, data from the first part of the active and passive chilled blocks were not recorded. However, no recalescence is observed. Table 4.4 shows the time for each block to cool to 400 °C.

Table 4.4
Time to 400 °C, medium Si alloy

Chill Type	Time to 400 °C	
	Sec.	Hours
Active	14290	3.97
Passive	17000	4.72
None	41700	11.58

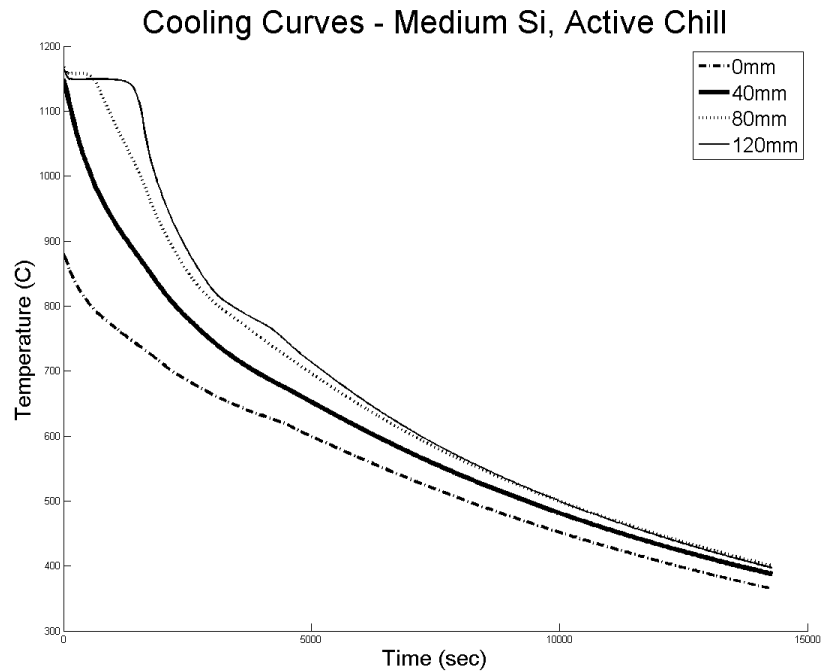


Figure 4.4: Cooling curve for heat 4, active chill, medium Si alloy. The eutectic arrest occurred at 1150 °C and the slight eutectoid arrest occurred at 800 °C.

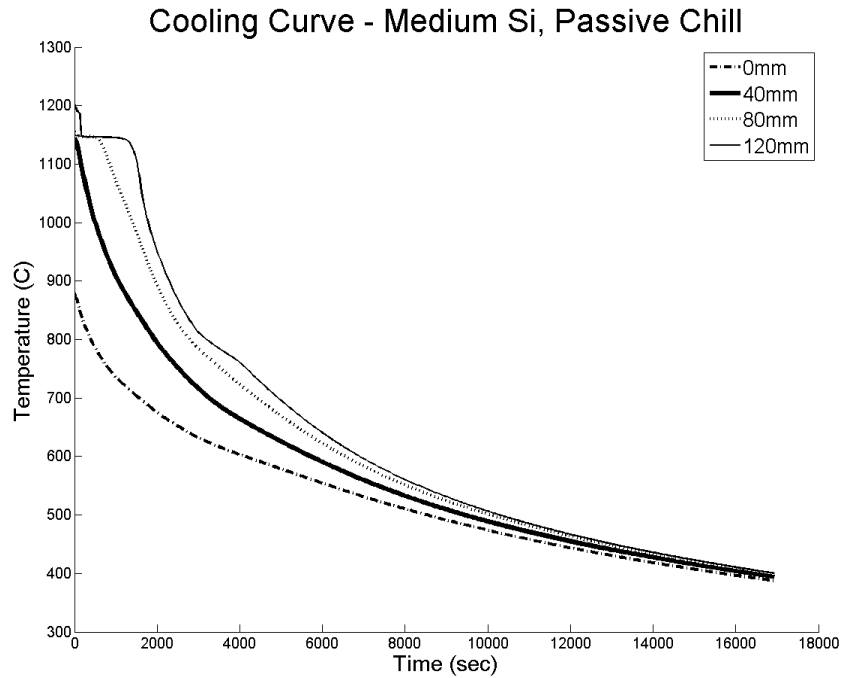


Figure 4.5: Cooling curve for heat 4, passive chill, Medium Si alloy. The eutectic arrest occurred at 1146°C and the slight eutectoid arrest occurred at 800°C.

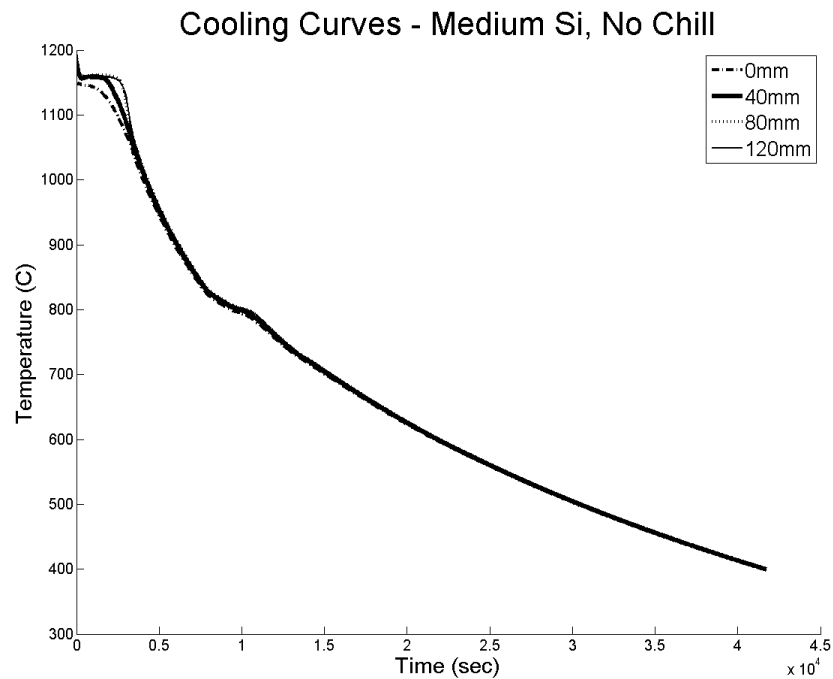


Figure 4.6: Cooling curve for heat 4, no chill, Medium Si alloy. There was not a large difference in cooling rate with distance from the bottom of the casting. The eutectic arrest occurred 1160°C while the eutectoid arrest occurred at 800°C

4.2.3 High Si

Figures 4.7 - 4.9 show the cooling curves for heat 6 and Table 4.5 shows the cooling times to 400°C.

Table 4.5
Cooling times to 400°C, High Si alloy

Chill Type	Time to 400 °C		
	Sec.	Min.	Hours
Active	14330	238.83	3.98
Passive	18700	311.67	5.19
None	41180	686.33	11.44

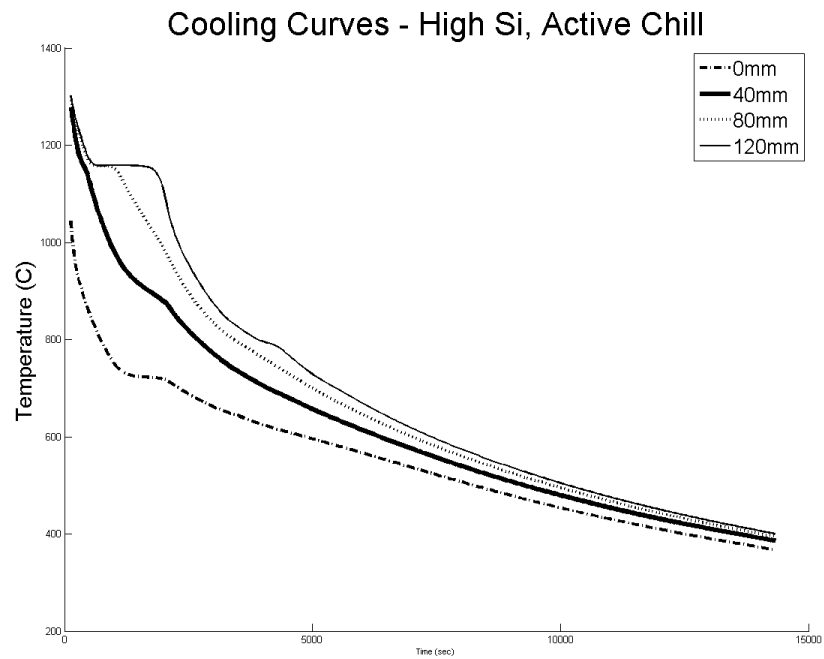


Figure 4.7: Cooling curve for actively chilled block, high Si alloy. Two arrests took place: eutectic (1154°C) and the eutectoid (793°C).

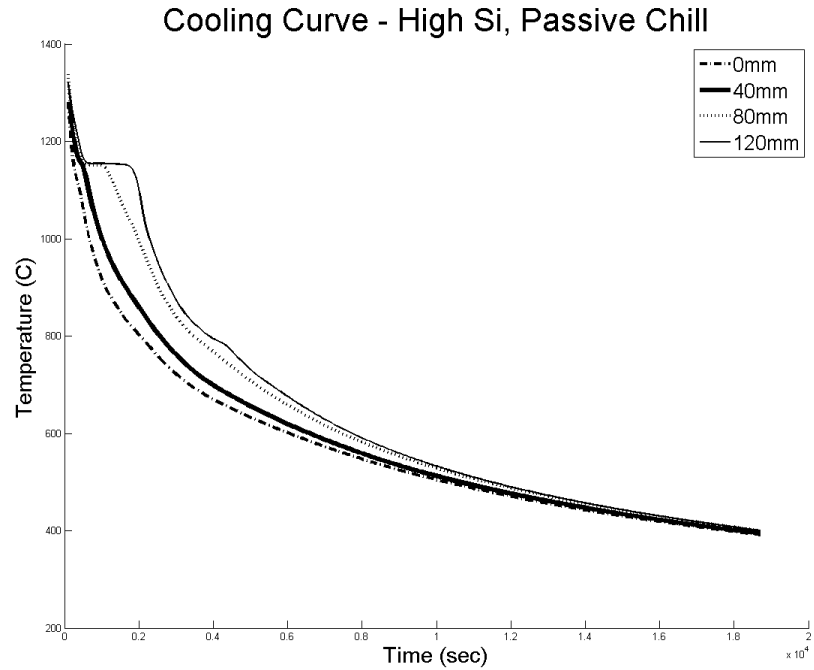


Figure 4.8: Cooling curve for high Si alloy, passively chilled block. The eutectic arrest occurred at 1159°C and the eutectoid arrest occurred at 796°C.

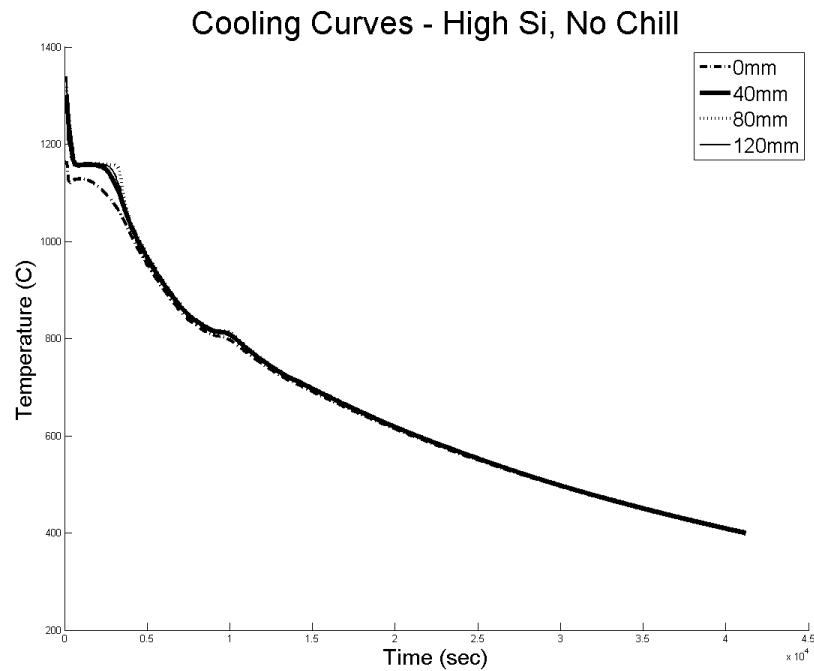


Figure 4.9: Cooling curve for non-chilled block, heat 6, high Si alloy. The eutectic arrest occurred at 1160°C and the eutectoid occurred at 814°C. The 0mm thermocouple experiences a neoeutectic at 1130°C.

4.2.4 Cooling Rates

From the cooling curves, it was possible to extract a cooling rate. This was defined as the time to reach 800°C (1472°F). Choosing this temperature avoided the recalescence seen in the medium Si alloy. Additionally, the cooling rate was fairly constant until that temperature in all heats poured. The cooling data for the medium Si alloy was incomplete. Therefore, in order to determine an accurate cooling rate, the curves were extrapolated to the pouring temperature. Samples were taken at 12.7mm, 63.5mm and 114.3mm from the chill interface and the thermocouple data was taken at 0mm, 40mm, 60mm and 120mm from the chill, thus, cooling rates at the sample locations were interpolated assuming the rate of change was constant between the thermocouple data points. Table 4.6 below lists the cooling rates for the sample locations in each block. Figure 4.10 shows the results of Table 4.6 graphically. The error bars are 1 standard error of the mean. For most of the data points, the error bars are hard to discern because they are very small.

Table 4.6
Summary of calculated cooling rates and interpolated cooling rates

Distance (mm)	Baseline			Medium Si			High Si		
	Active	Passive	None	Active	Passive	None	Active	Passive	None
0	16.9	36.1	5.2	48.0	34.3	5.2	67.44	23.84	4.90
40	16.5	15.1	5.2	17.5	19.5	4.9	17.85	18.73	4.64
80	13.9	14.7	5.2	13.4	14.8	4.7	14.11	13.76	4.59
120	13.0	12.8	5.2	12.5	13.1	4.7	12.29	12.43	4.63
12.7	16.8	29.4	5.2	38.3	29.6	5.1	51.7	22.2	4.8
63.5	15.0	14.8	5.2	15.2	16.7	4.8	15.7	15.8	4.6
114.3	13.2	13.1	5.2	12.7	13.4	4.7	126	12.6	4.6

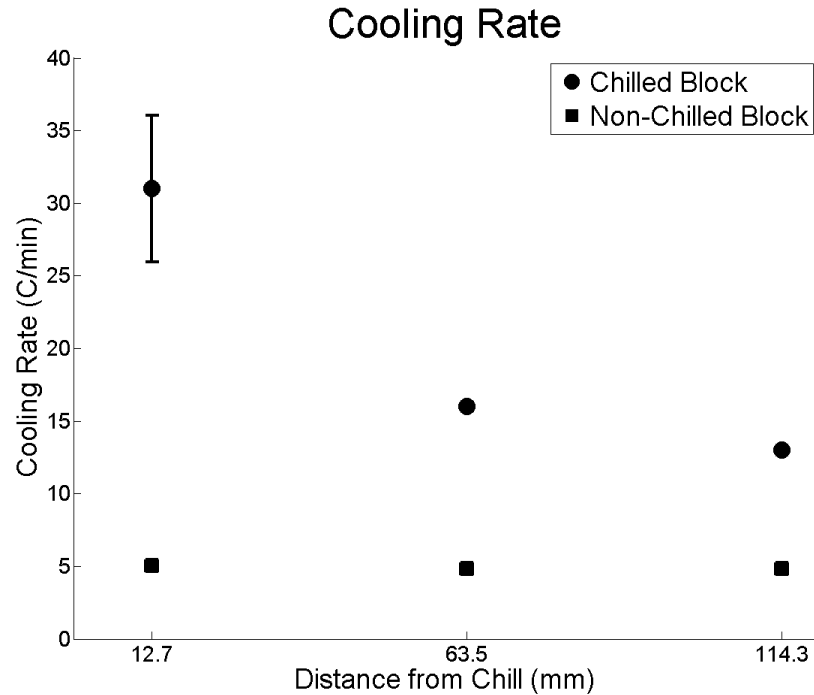


Figure 4.10: Plot of cooling rate as a function of distance from the chill. As distance increases, the cooling rate decreases for the chilled samples but remains constant for the non-chilled sample.

4.3 Chemical Analysis

Each heat was sampled for chemical analysis as previously outlined. Table 4.7 below shows the results of the three heats along with their respective targets. The final Mg contents were taken from the sample obtained after the Mg treatment occurred, but prior to inoculation. This was necessary since the samples taken after pouring needed to be re-melted and chilled. Final Mg values are unavailable for the medium Si alloy; a sample after treatment was not taken.

The final chemistry values are within the ranges given for each element. P was kept lower than the target since it is typically detrimental to mechanical properties and microstructure. The two main differences between the medium Si and high Si alloys are the C and Si contents - the other alloy elements were kept constant.

Table 4.7
Final heat chemistries and their respective targets.

Alloy		C	Si	Mg	P	Mn	S	CE
Baseline	Target	3.70	2.00	0.039	0.025	0.18	0.005	4.38
	Actual	3.72	1.77	0.042	0.007	0.15	0.005	4.31
Medium Si	Target	3.20	3.65	0.045	0.025	0.28	0.005	4.43
	Actual	3.27	3.70	n/a	0.009	0.27	0.005	4.51
High Si	Target	3.05	4.25	0.045	0.025	0.28	0.005	4.48
	Actual	3.06	4.34	0.069	0.012	0.29	0.005	4.51

4.4 Metallography

4.4.1 Nodularity and Nodule Count

Nodularity and nodule counts were obtained via PAX-it! software as outlined in section 3.6.1. Table 4.8 below summarizes the results of this analysis. As stated in section 3.6.1, a cut off of 50% was used to determine nodularity values and nodule count. The letter after the alloy name indicates which chill it is from - A for the active chill, P for the passive chill and N for no chill - while the number indicates which slice it came from within the block. Slice 1 was adjacent to the chill, slice 3 had a midpoint 63.5mm (2.5in) above the chill and slice 5 had a midpoint 114.3mm (4.5in) above the chill. Photomicrographs of the samples may be found in Appendix B and the specific figure with those images is given in the table. Some samples showed evidence of compacted or flake graphite at the surface of the castings. This is a result of localized de-nodularization. In these regions, the residual Mg is most likely low or it has been negated by an excess in tramp elements such as S, possibly present in the sand.

4.4.2 Matrix Microstructure

All samples consisted of a ferrite matrix with varying amounts of intercellular pearlite colonies. Some samples had regions of all pearlite, which were typically visible macroscopically. Grain size measurement were attempted utilizing the line intercept method in which a line is drawn, and the number of grain boundaries counted, but the results were contradictory to what were observed visually. Additionally, it is not common practice in industry to report grain size for ductile iron. Photomicrographs of each sample are provided in Appendix B.

Table 4.8
Summary of quantitative metallography results for each sample from each heat.

Sample	Distance From Chill (mm)	Nodularity	Nodule Count (mm ⁻²)	Average Roundness (%)	Sample Image Number
Baseline-A1	12.7	96	358	83	Figure B.1
Baseline-A3	63.5	93	228	77	Figure B.2
Baseline A5	114.3	93	182	75	Figure B.3
Baseline P1	12.7	94	420	84	Figure B.4
Baseline P3	63.5	94	209	77	Figure B.5
Baseline P5	114.3	83	115	69	Figure B.6
Baseline N1	12.7	84	92	69	Figure B.7
Baseline-N3	63.5	91	143	74	Figure B.8
Baseline-N5	114.3	92	135	75	Figure B.9
Med. Si-A1	12.7	93	317	83	Figure B.10
Med. Si-A3	63.5	95	203	82	Figure B.11
Med. Si-A5	114.3	90	161	77	Figure B.12
Med. Si-P1	12.7	95	328	86	Figure B.13
Med. Si-P3	63.5	93	181	79	Figure B.14
Med. Si-P5	114.3	95	235	82	Figure B.15
Med. Si-N1	12.7	84	64	68	Figure B.16
Med. Si-N3	63.5	88	113	72	Figure B.17
Med. Si-N5	114.3	79	118	70	Figure B.18
High Si-A1	12.7	96	421	86	Figure B.19
High Si-A3	63.5	94	321	80	Figure B.20
High Si-A5	114.3	88	210	75	Figure B.21
High Si-P1	12.7	95	419	85	Figure B.22
High Si-P3	63.5	92	291	78	Figure B.23
High Si-P5	114.3	86	223	74	Figure B.24
High Si-N1	12.7	82	143	68	Figure B.25
High Si-N3	63.5	87	181	71	Figure B.26
High Si-N5	114.3	78	150	66	-

4.5 Mechanical Testing

4.5.1 Tensile

A summary of the results from tensile testing are given in Table 4.9. A quick analysis of the data shows that the moduli were fairly constant for all samples, regardless of alloy or distance from the chill (i.e. cooling rate). However, differences may be seen for yield stress, tensile strength and strain. In addition to tensile testing, Young's modulus was measured ultrasonically. The results may be found in Table 4.9.

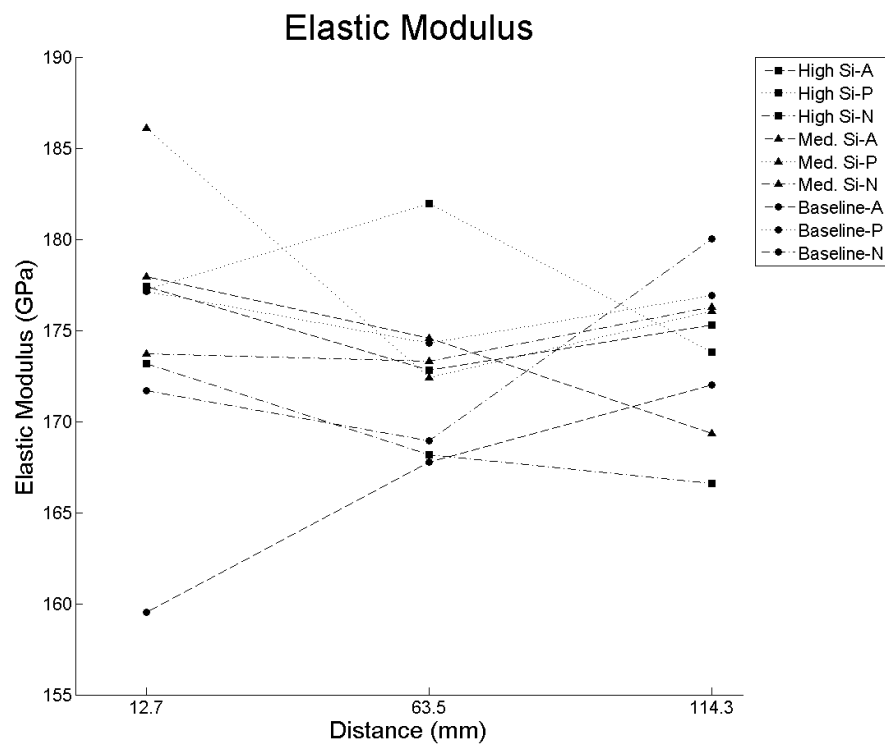


Figure 4.11: Plot showing Young's modulus as a function of distance from the chill

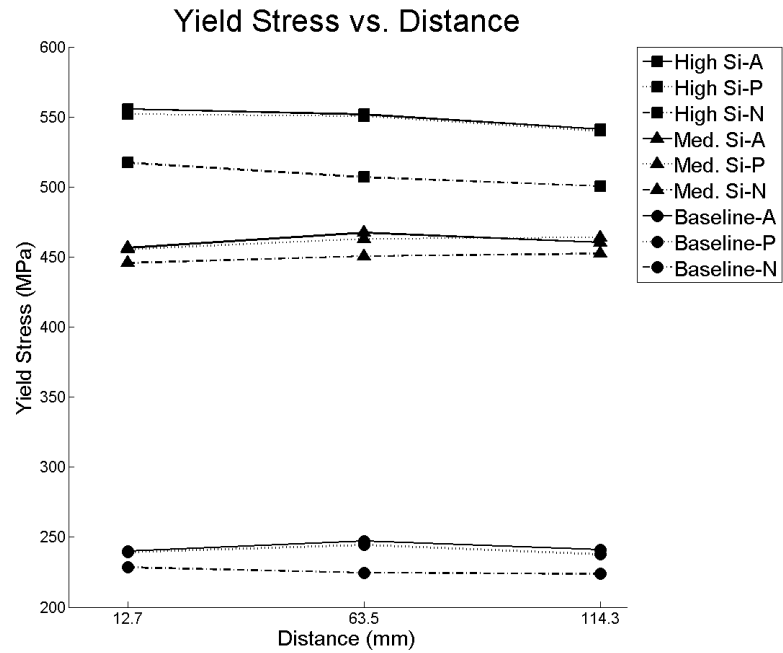


Figure 4.12: Plot of yield stress as a function of distance from the chill

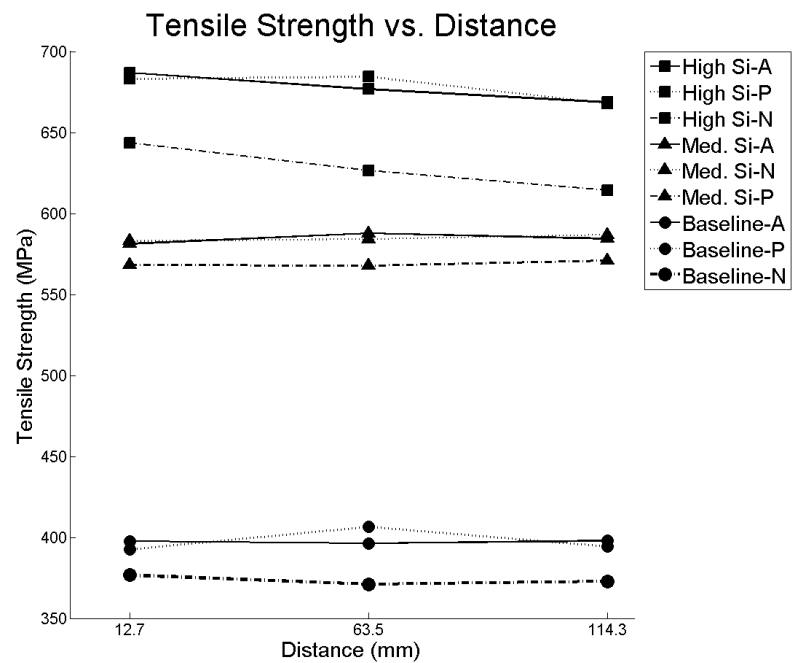


Figure 4.13: Plot of tensile strength as a function of distance from the chill

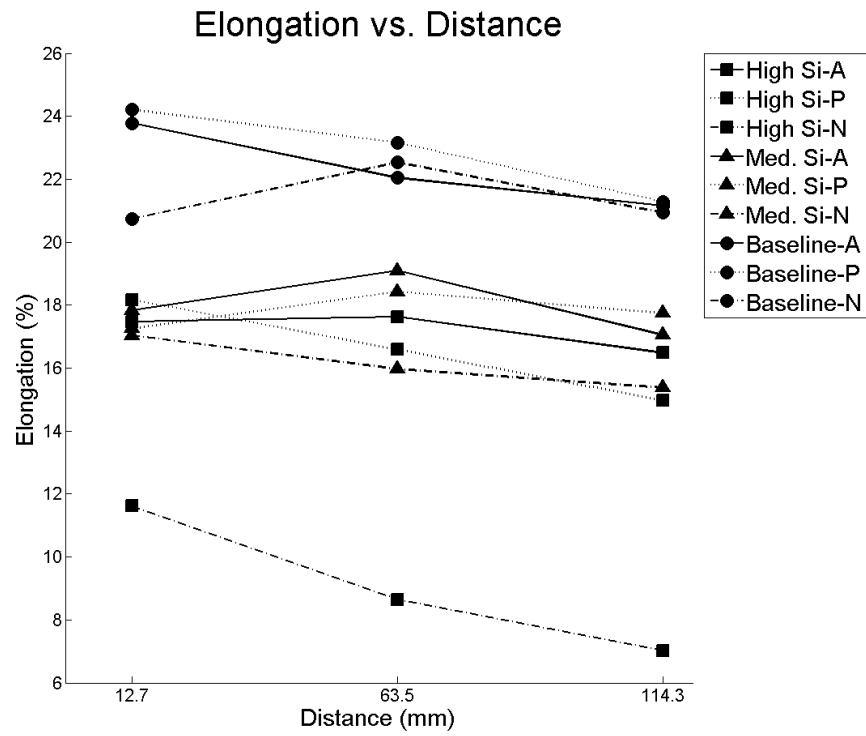


Figure 4.14: Plot of strain as a function of distance from the chill

Table 4.9 Summary of tensile testing results for all samples.

Sample	Distance (mm)	Average Modulus (GPa)	Average Yield Stress (MPa)	Average Tensile Strength (MPa)	Average Elongation (%)	Ultrasonic Modulus (GPa)
Baseline A	12.7	159.53	240.09	397.72	23.78	193.3
	63.5	167.75	247.30	396.24	16.28	181.9
	114.3	172.01	241.14	397.80	21.15	194
Baseline P	12.7	177.12	239.21	392.42	24.20	183.6
	63.5	174.30	244.31	406.47	23.16	184.2
	114.3	176.91	237.65	394.28	21.28	183.3
Baseline N	12.7	171.67	228.50	376.75	20.74	186.1
	63.5	168.92	224.50	370.99	22.53	179.1
	114.3	180.02	223.88	372.83	20.93	180.1
Med. Si A	12.7	177.96	456.41	581.19	17.83	178.5
	63.5	174.56	467.29	587.82	19.10	180
	114.3	169.36	460.47	584.28	17.05	176.8
Med. Si P	12.7	186.12	455.42	583.01	17.26	178.4
	63.5	172.42	463.01	584.02	18.43	173.4
	114.3	176.04	463.95	586.80	17.74	179.2
Med. Si N	12.7	173.71	445.67	568.08	17.04	177.6
	63.5	173.31	450.65	567.61	15.97	182.9
	114.3	176.30	452.40	570.91	15.37	173.9
High Si A	12.7	177.40	555.69	686.77	17.47	186.1
	63.5	172.80	551.80	676.80	17.63	179.5
	114.3	175.29	541.14	668.68	16.48	178.3
High Si P	12.7	177.25	552.07	683.04	18.17	178.9
	63.5	181.94	550.47	684.36	16.59	178.8
	114.3	173.80	539.96	667.83	14.97	178.5
High Si N	12.7	173.17	517.31	643.56	11.62	181.6
	63.5	168.17	506.84	626.49	8.64	190.2
	114.3	166.59	500.49	614.32	7.02	163.8

4.5.2 Charpy Impact

Charpy impact energies and percent shear are given in Table 4.10. Only the baseline samples had impact energies above 10J and showed any form of ductile fracture. The medium and high Si alloys were below the DBTT for all test temperatures. The percent shear indicates how much of the fracture occurred in a ductile manner and is 0 for all tests in the medium and high Si alloys. It decreases in the baseline alloy as testing temperature decreases.

Table 4.10
Summary of impact energies and percent shear for Charpy impact testing

Sample	Temp:	25 °C		-20 °C		-40 °C	
	Distance from Chill (mm)	Impact Energy (J)	% Shear	Impact Energy (J)	% Shear	Impact Energy (J)	% Shear
Baseline A	12.7	11.5	7.5	9.65	5	9.45	3
	63.5	12.5	7.5	11.7	5	8.85	3
	114.3	13.2	5	13.4	5	6.25	1.5
Baseline P	12.7	11.35	5	11.2	5	9.65	3
	63.5	13.4	5	13.05	5	8.1	3
	114.3	13.9	5	13.6	5	10.3	3
Baseline N	12.7	16.1	5	13.55	5	9.5	3
	63.5	15.45	5	13.4	5	9.5	3
	114.3	15.1	5	13.25	5	8.65	3
Med. Si A	12.7	2.7	0	2	0	1.85	0
	63.5	2.4	0	2.4	0	1.7	0
	114.3	2.55	0	1.85	0	1.7	0
Med. Si P	12.7	2.55	0	1.85	0	1.7	0
	63.5	2.55	0	1.7	0	1.7	0
	114.3	2.55	0	2	0	1.85	0
Med. Si N	12.7	2.2	0	2	0	1.7	0
	63.5	2.2	0	1.85	0	1.7	0
	114.3	2	0	2	0	1.7	0
High Si A	12.7	1.7	0	1.4	0	1.4	0
	63.5	1.85	0	1.4	0	1.4	0
	114.3	1.7	0	1.4	0	1.4	0
High Si P	12.7	1.7	0	1.4	0	1.4	0
	63.5	1.7	0	1.4	0	1.4	0
	114.3	1.7	0	1.4	0	1.4	0
High Si N	12.7	1.7	0	1.4	0	1.4	0
	63.5	1.7	0	1.4	0	1.4	0
	114.3	1.7	0	1.4	0	1.4	0

4.5.3 Vickers Microhardness

The results from the Vickers microhardness testing is given in Table 4.11. Figures 4.15 - 4.17 show plots of hardness as a function of distance from the chill for all blocks in a single heat. In the medium Si alloy (Figure 4.16), the hardness for all blocks was highest in the middle of the blocks while in the baseline alloy (Figure 4.15), the hardness was lowest in the centers. In heat 6 (high Si) (Figure 4.17), the two chilled blocks stayed relatively constant in hardness; however, the non-chilled block experienced a significant decrease in hardness as the distance from the surface increased. When comparing heats with each other, heat 6 (High Si) had the highest hardness and heat 5 (Baseline) had the lowest hardness. This is shown in Figure 4.18.

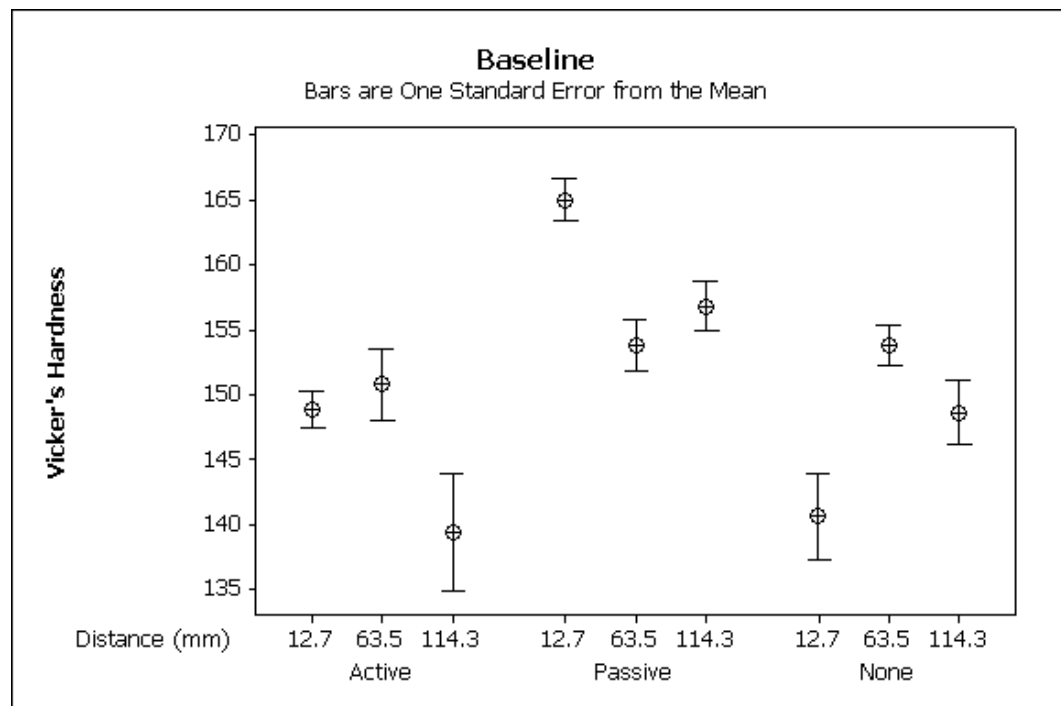


Figure 4.15: Plot showing hardness as a function of distance from the chill for each block from the baseline alloy.

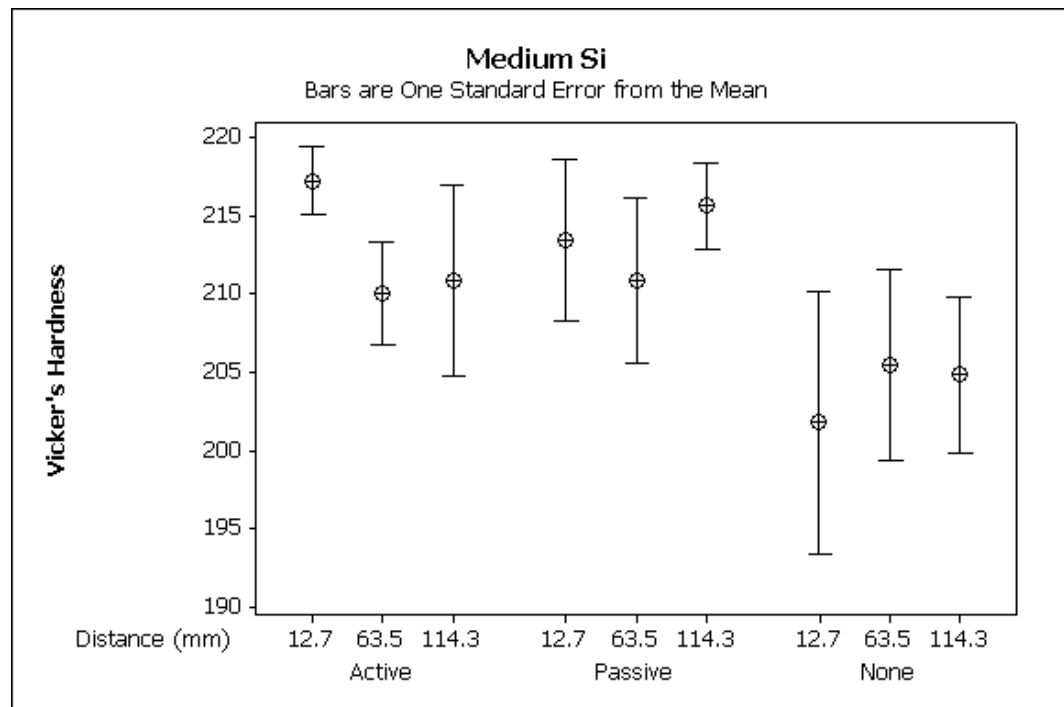


Figure 4.16: Plot showing hardness as a function of distance from the chill for each block from the medium Si alloy.

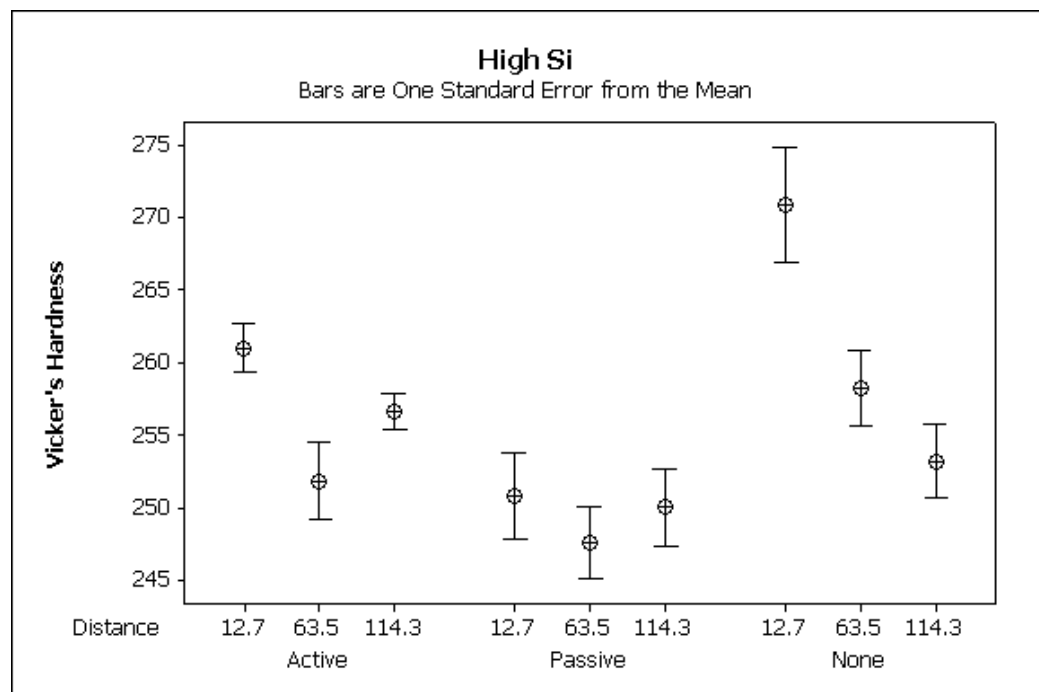


Figure 4.17: Plot showing hardness as a function of distance from chill for each block from the high Si alloy.

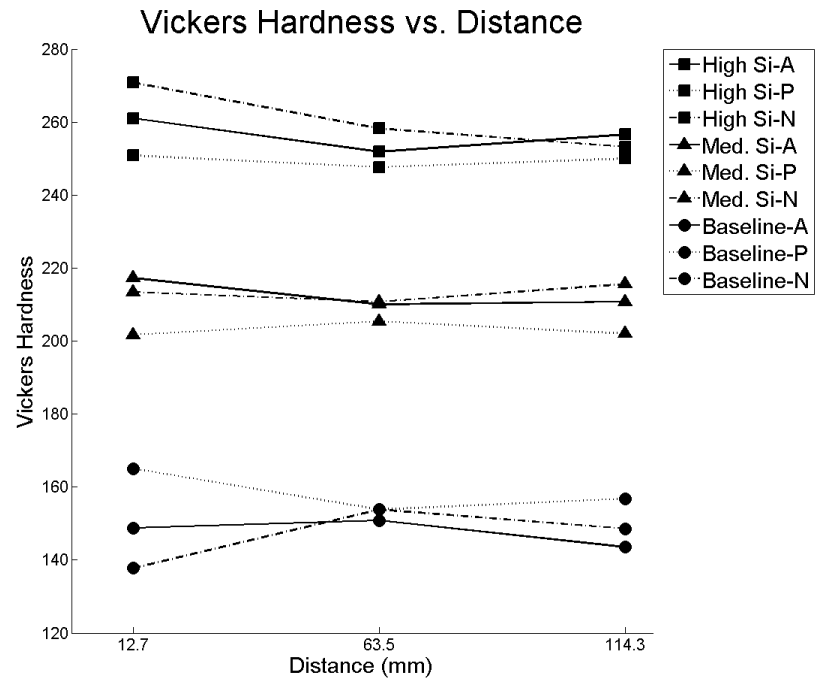


Figure 4.18: Average Vickers hardness of each block plotted as a function of distance from the chill. Note that each heat is grouped together and they are distinct from each other.

Table 4.11
Summary of hardness results

Heat	Chill Type	Distance from Chill (mm)	Average Hardness	Standard Deviation
Baseline	Active	12.7	148.8	3.11
Baseline	Active	63.5	150.8	6.14
Baseline	Active	114.3	139.4	10.06
Baseline	Passive	12.7	165	3.67
Baseline	Passive	63.5	153.8	4.38
Baseline	Passive	114.3	156.8	4.21
Baseline	None	12.7	140.6	7.37
Baseline	None	63.5	153.8	3.35
Baseline	None	114.3	148.6	5.59
Med. Si	Active	12.7	217.2	4.82
Med. Si	Active	63.5	210	7.45
Med. Si	Active	114.3	210.8	13.70
Med. Si	Passive	12.7	213.4	11.63
Med. Si	Passive	63.5	210.8	11.78
Med. Si	Passive	114.3	215.6	6.15
Med. Si	None	12.7	201.75	16.68
Med. Si	None	63.5	205.4	13.65
Med. Si	None	114.3	204.8	11.21
High Si	Active	12.7	261	3.81
High Si	Active	63.5	251.8	5.93
High Si	Active	114.3	256.6	2.79
High Si	Passive	12.7	250.8	6.53
High Si	Passive	63.5	247.6	5.46
High Si	Passive	114.3	250	6.04
High Si	None	12.7	270.8	8.81
High Si	None	63.5	258.2	5.89
High Si	None	114.3	253.2	5.63

5 Discussion

5.1 ANOVA Analysis

For many of the results, ANOVA analyses were performed. This type of analysis is powerful for being able to separate factors and determine if each one individually is significant to a measured response. ANOVA tests the null hypothesis that the means of two groups are equal to each other. The alternative hypothesis is that they are not. An F test is then performed from which a p value may be obtained for a specified confidence level. For the purposes of this study, the confidence level was set at 95%. In order for the alternative hypothesis to be proven true, a p value of 0.05 or less is required for each factor. Otherwise, the null hypothesis is proven true - that the means are equal.

5.2 Cooling Rate

One of the primary focuses of this study was the effect of an actively cooled chill and a passive chill on the solidification time, microstructure and mechanical properties of heavy section castings when compared to a conventional sand casting. The cooling curves, calculated cooling rates and times to 400°C presented in section 4.2 illustrated that both the chills had a large effect on the solidification of the castings. It was not uncommon to see, as shown in Tables 4.4 - 4.5, that the chilled blocks cool in a third to 45% of the time that the non-chilled block required with the actively cooled chill being slightly more potent than the passive chill. Had the ratio of casting weight to chill weight been higher, it is expected that an even more dramatic difference between the two chills would have been observed.

Specifically, in the baseline alloy, the actively and passively cooled blocks took 34% and 41% of the time to cool to 400°C that the non-chilled block required. The medium Si alloy, which was interrupted during cooling, showed a 34% and 35% total cooling time for the actively and passively cooled blocks, respectively. Finally, the high Si alloy blocks cooled in 35% (actively cooled) and 45% (passively cooled) of the time compared to the non-chilled block. In addition to the cost savings of having the castings cool faster, there is also a metallurgical benefit. Faster cooling rates are usually associated with a finer degree of segregation, a higher nodule count and better nodularity.

Further analysis of the cooling curves presented in Figure 4.4 through Figure 4.9 shows that the baseline alloy experienced a highly unusual amount of recalescence while the two higher Si alloys did not. It is typical to see a recalescence on the order of tens of degrees in castings, which is generally associated with austenite nucleation; however, at the 0mm thermocouple in the passively chilled block, a recalescence of 220°C is observed. The degree of

recalescence is slightly less (161°C) in the actively chilled block and decreases in both chilled castings with increasing distance from the chill, until it completely disappears at 120mm. Recalescence occurs when undercooling provides a large driving force for austenite dendrites to grow and nucleate. The result is an increase in the latent heat in the casting causing an increase in temperature. Generally, the temperature increase reaches the eutectic temperature, but this was not seen in the test castings. The large chill:casting ratio and the presence of the fluid in the active chill continued to remove the heat in the casting until the eutectic reaction was complete, at which point the casting began to cool again. The high Si alloy non-chilled block exhibited a neoeutectic at 1130°C . A neoeutectic is associated with a growth in the graphite nodules as C diffuses through the austenite shell (Rundman 2002)

An ANOVA analysis was performed on the effects of chill type, distance and Si content on the cooling rate. It was found that only the distance from the chill was a significant factor. This indicates that there was not a difference between the actively and passively cooled blocks regarding cooling rate and the chill type is not a significant factor. This analysis was repeated to test if this conclusion was the same with respect to the mechanical properties and microstructural features of the blocks and it was found that there was no difference between the two chilled samples. Therefore, the two chilled blocks will be grouped together for the remainder of the analysis and the cooling rates for the chilled blocks are averaged for each sample location: 31, 16, and $13^{\circ}\text{C}/\text{min}$. A full analysis of these results, including an assessment of the significance of the active and passive chills, may be found in Appendix C.

Figure 5.1 shows a plot of the cooling rates of the blocks as a function of distance from the chill/bottom for the chilled and non-chilled castings. The error bars show the standard error for each data point. The non-chilled casting had a relatively constant cooling rate of $5^{\circ}\text{C}/\text{min}$, while the cooling rate of the chilled castings decreased dramatically with increase in distance from the chill. It is interesting to note that the cooling rate furthest from the chill, and thus, presumably, the slowest in the chilled block, is still about 3 times faster than the non-chilled casting. This is evidence that the presence of the chill plays a significant role in the time the casting will take to solidify and cool.

The ANOVA analysis previously discussed tested for the effect of not only distance, but also Si content and chill presence on the cooling rate. It was found that both distance and chill presence were significant to the cooling rate. That is, as distance increased, the cooling rate decreased. Si content did not have an effect on the cooling rate indicating that the Si did not have a chilling effect on the iron. The presence of the chill had an effect on the cooling rate when compared to the castings without a chill present. These effects are shown in Figure 5.2.

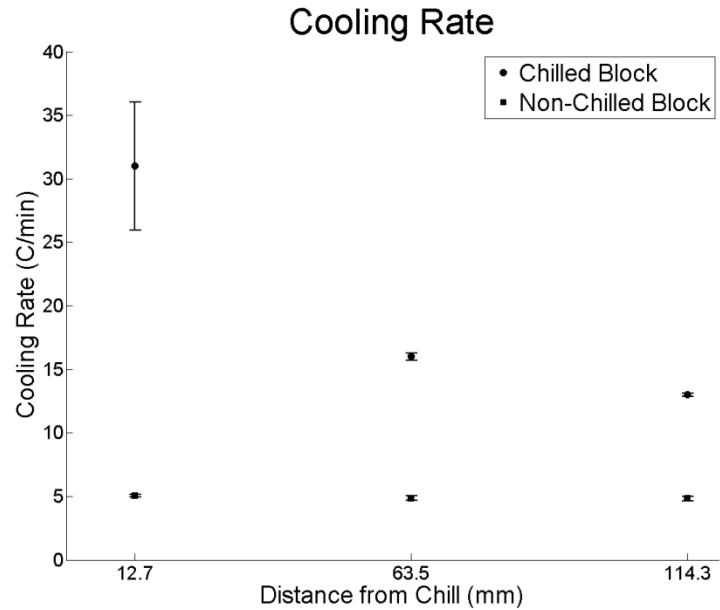


Figure 5.1: Cooling rate as a function of distance from the chill for the chilled blocks and non-chilled blocks. The non-chilled blocks experienced a relatively constant cooling rate while the chilled blocks showed a dramatic decrease in cooling rate for increasing distance from the chill. However, even at the furthest point, the chilled cooling rate is still about 3 times faster than the non-chilled block.

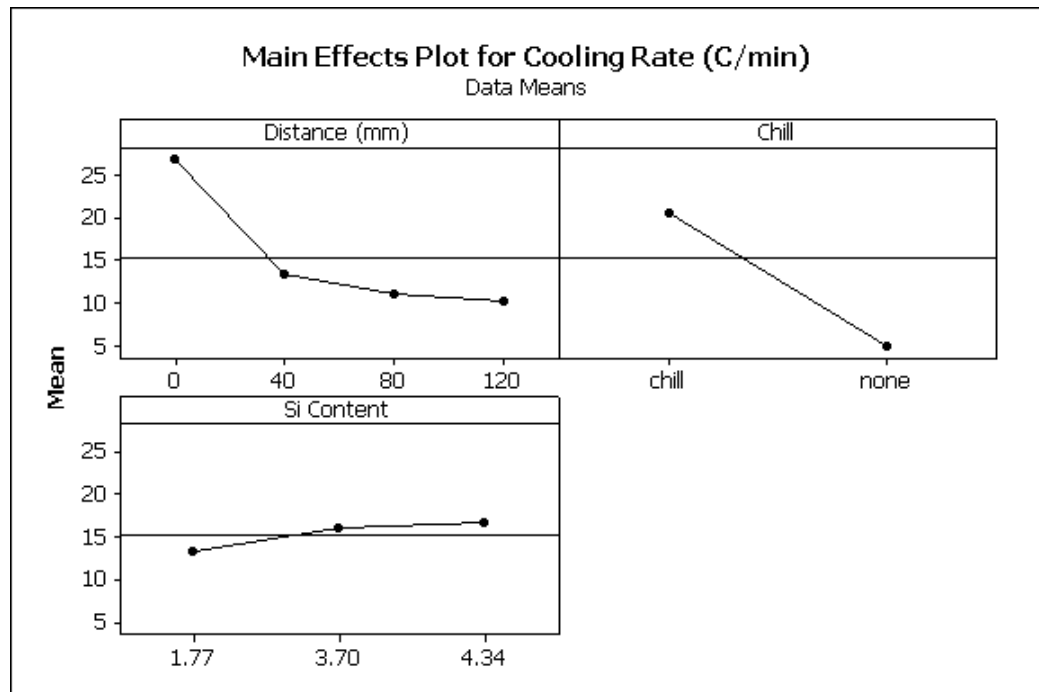


Figure 5.2: Effect of distance from the chill, presence of chill and Si content on the cooling rate. The presence of a chill and the distance were both significant to the cooling rate but the Si content was not. The line at 15 indicates the mean of the data.

5.3 Microstructure

5.3.1 Composition

Alloy composition plays a major role in determining the microstructure of a casting. The presence, or absence, of different alloying elements can influence the occurrence, or lack thereof, of different phases

Figure 5.4 shows nodularity as a function of Si content and the error bars represent one standard error of the mean. The error bars include the effect of cooling rate, thus causing them to be large. Although it is difficult to discern a correlation between Si content and nodularity, performing an ANOVA analysis separates the two factors and indicates that Si content has an effect on the nodularity of the castings. The full analysis may be found in Appendix D. The effect of Si on nodularity is shown in Figure 5.7(a). It can be seen that for an increase in Si content, a corresponding decrease in nodularity is observed.

The same approach may be taken to evaluate the effect of Si on nodule count in a casting. Figure 5.4 shows nodule count as a function of Si content. The effect of cooling rate, just as in Figure 5.3, is large, resulting in large standard

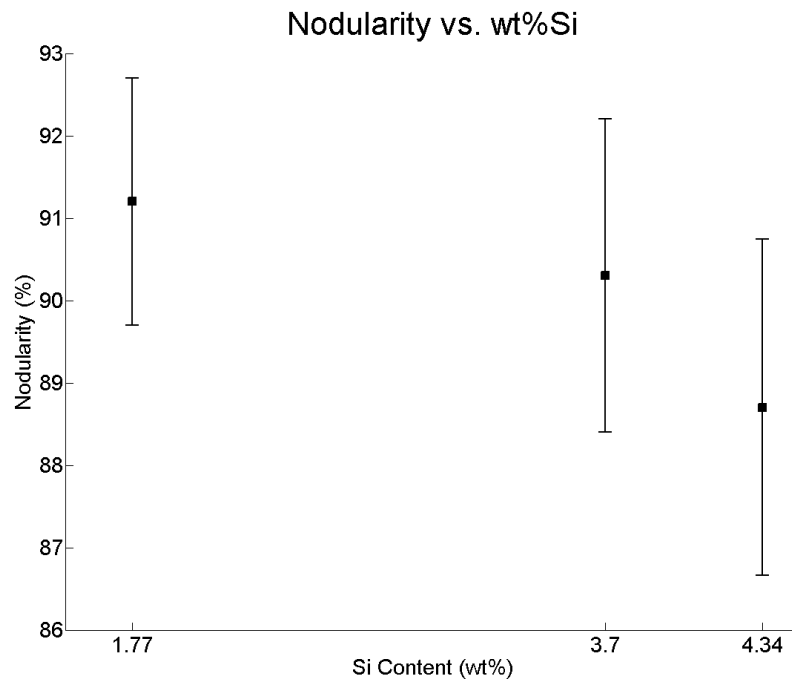


Figure 5.3: Nodularity vs. Si content. The error bars are one standard error of the mean and are large because this plot also includes the effect of cooling rate.

error bars. Their size makes it difficult to discern if there is a correlation between Si content and nodule count. However, the same ANOVA analysis performed previously clearly indicated that the Si content does have an effect on the nodule count. Figure 5.8(a) shows this effect: as the presence of Si increases, the nodule count also increases. Furthermore, it was qualitatively noted that as the nodule count increased, so did the fineness of the ferrite matrix. Therefore, it may be concluded that an increase in Si will lead to an increasingly fine microstructure. This is also evident from analyzing the quantitative metallography results presented in Table 4.8. While a high nodule count increases the fineness of the microstructure, poorly formed nodules may act as stress concentrators decreasing the mechanical properties of the casting.

5.3.2 Cooling Rate

Cooling rates also have a strong impact on microstructure, which is well documented in the literature. Many studies state that the best way to ensure a quality microstructure, especially graphite structure, is to control the cooling rate (Asenjo 2007; Helmink 1977; Sprengler 1995). Asenjo, in his analysis of the formation of chunky graphite in heavy section ductile iron castings,

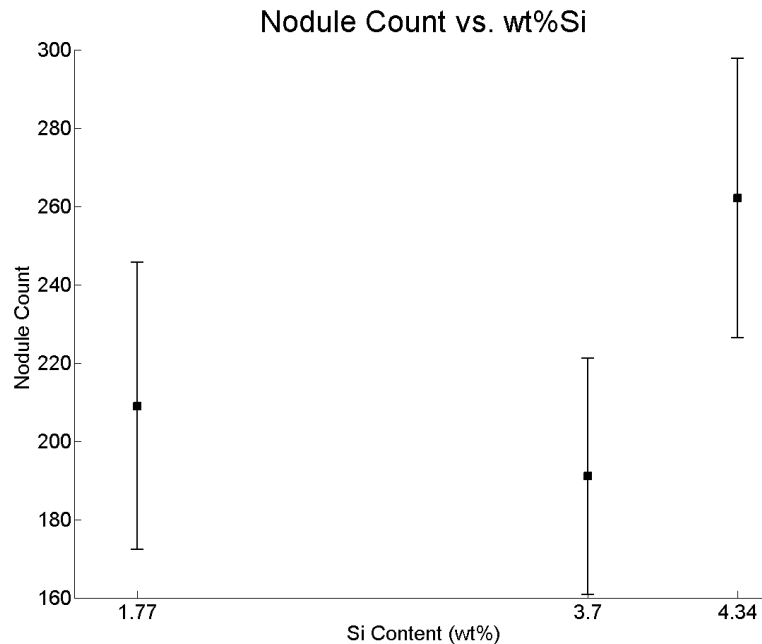


Figure 5.4: Nodule count as a function of Si content. The error bars are one standard error of the mean and are large because they include the effect of cooling rate.

suggests that long eutectic reactions - the point at which the liquid transforms to austenite and graphite - are the cause for chunky graphite. The author further indicates that at locations close to a chill or other heat sink, the eutectic reaction, which typically occurs at one temperature, occurs at continually increasing undercooling and that this is favorable to the formation of highly nodular graphite particles. This was found to be true in the present study and the summary of nodularity ratings can be found in Table 4.8. Samples closer to the chill often had higher nodule counts, smaller nodule sizes and a higher degree of nodularity than those samples further away from the chill. Additionally, when analyzing the cooling curves presented in Figures 4.4 - 4.9, it may be seen that the eutectic arrest was either eliminated or dramatically reduced in length.

Additionally, Tiedje (2010) states that graphite nucleation is a result of undercooling. Therefore, an increase in nodule count as the amount of undercooling increases should be observed. It is difficult to discern the amount of undercooling in the medium Si and high Si alloys since there is not a visible recalescence in the cooling curves. However, the cooling rate can still be analyzed by assuming that the cooling rate decreases as distance from the surface increase. Looking at it in this manner, a decrease in nodule count should be seen for increasing distance from the chill. Table 4.8 shows this decrease for all alloys.

The ANOVA analysis used to determine the significance of Si content on nodularity and nodule count was also used to determine the significance of cooling rate. It was found that cooling rate played an even more significant role in nodularity and nodule count than Si. Figure 5.5 and Figure 5.6 show the nodularity and nodule count, respectively, as a function of cooling rate for the chilled and non-chilled blocks. These plots include the effect of Si on the responses, but since this effect is small compared to the cooling rate, they are smaller than in Figure 5.3 and Figure 5.4. In Figure 5.7 and Figure 5.8, the effect of cooling rate on nodularity and nodule count, respectively, is shown. In both cases it can be seen that an increase in cooling rate results in an increase in nodularity and nodule count.

The effect of cooling rate may be seen in micrographs of samples given in Figure 5.9(a)-(f). Image (a) from the sample baseline-A1, where the cooling rate was 16.8°C/min, shows a high nodule count with high nodularity. Image (c) from sample medium Si-A1 and (e) from sample high Si-P1, which had cooling rates of 38.3 and 22.2°C/min, respectively, also show high nodule counts. These three images also show a high degree of nodularity. In comparison, (b) from medium Si-A5, (d) from medium Si-P5 and (f) from high Si-P5 all show larger nodules, a lower nodule count, and a decrease in

nodularity. Image (d) also shows the presence of degenerate graphite. The occurrence of degenerate graphite was greatest for the slowest cooling rates.

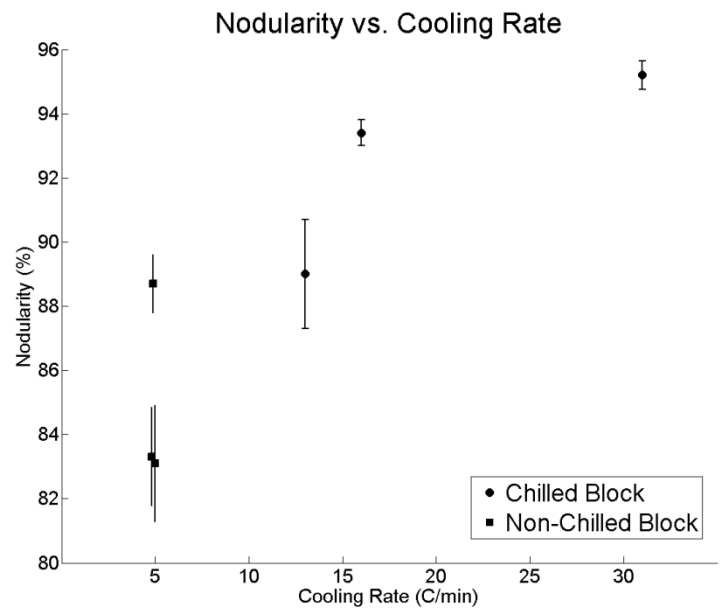


Figure 5.5: Nodularity as a function of cooling rate. The error bars are one standard error of the mean. They are smaller in this figure than in Figure 5.3 because the effect of Si, present in the data, is smaller than cooling rate.

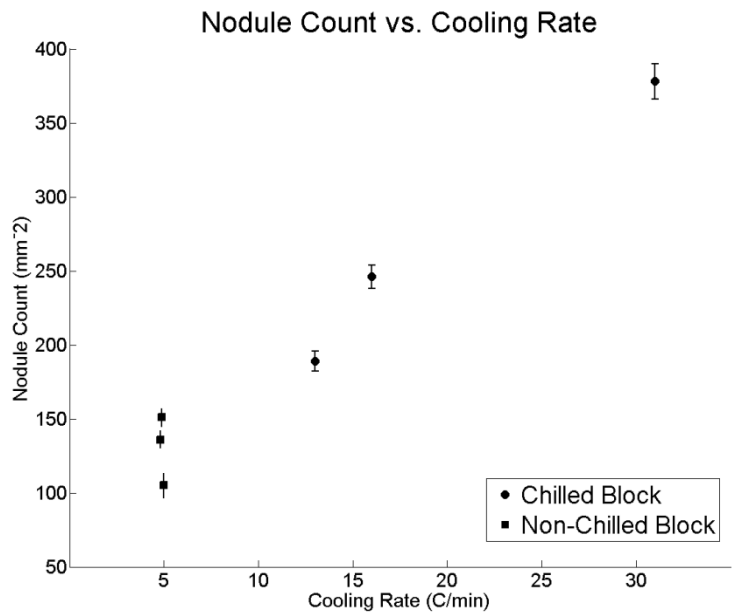


Figure 5.6: Nodule count as a function of cooling rate. The error bars are one standard error of the mean and are small because the effect of Si content is small compared to the effect of cooling rate.

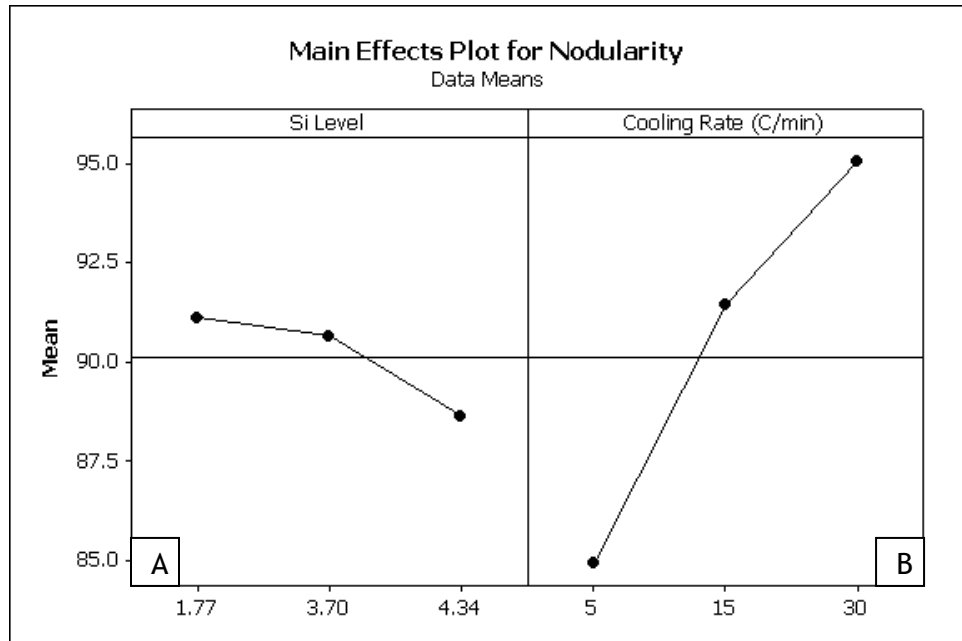


Figure 5.7: Effect of Si content (a) and cooling rate (b) on nodularity. An increase in Si content decreases nodularity while an increase in cooling rate results in an increase in nodularity. By comparing (a) and (b), it can be seen that the cooling rate has a much larger effect on the nodularity than the Si content.

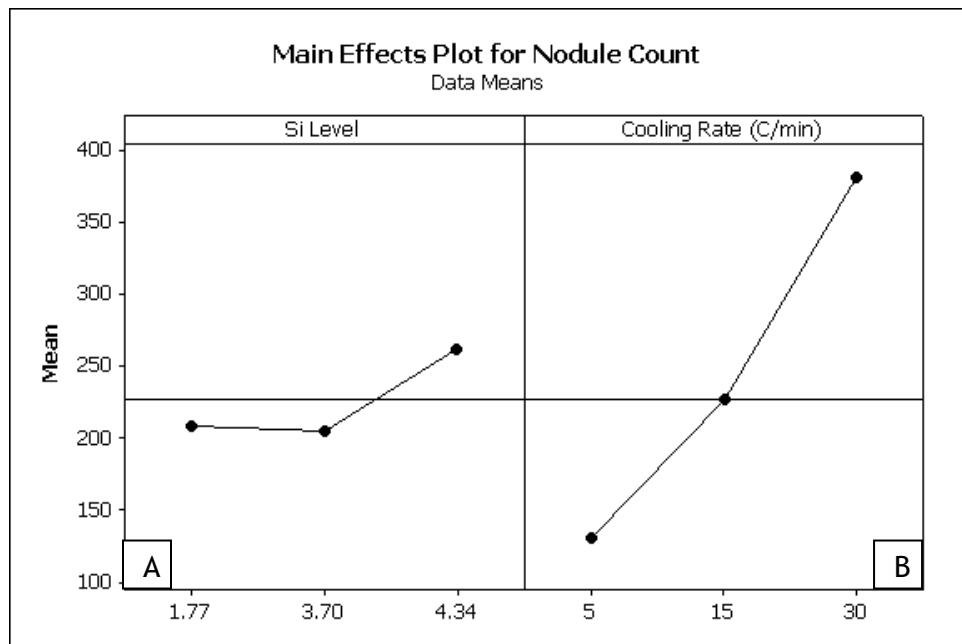


Figure 5.8: Effect of Si content (a) and cooling rate (b) on nodule count. Comparing (a) and (b) shows that the cooling rate has a larger effect on the nodule count than Si, although an increase in either will result in an increase in nodule count.

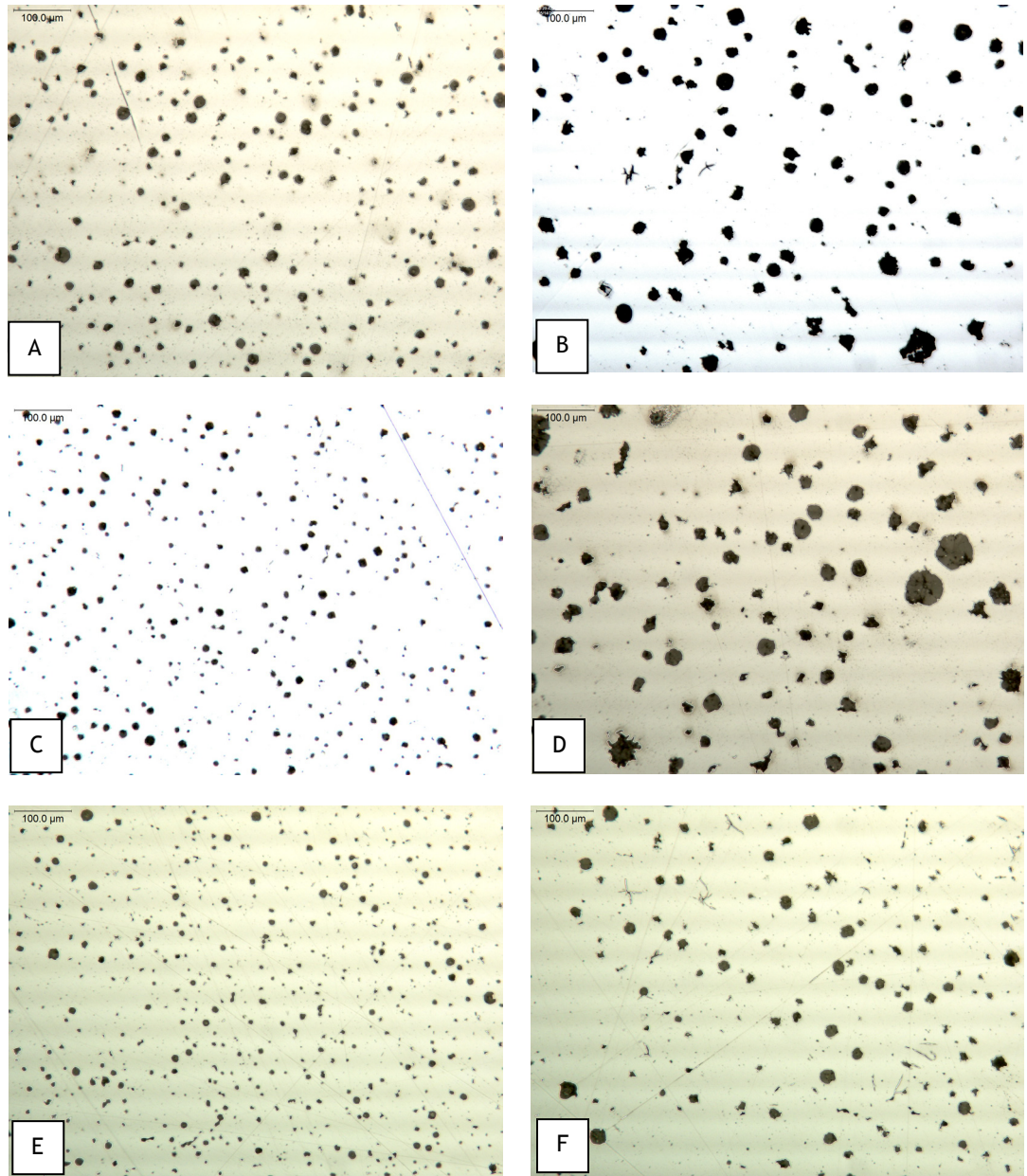


Figure 5.9: Photomicrographs showing as-polished graphite structures of the test castings. Examples of high nodule counts are shown in samples Baseline-A1 (a), Medium Si-A1 (c) and High Si-P1 (e) while lower nodule counts and larger nodules are exemplified in samples Medium Si-A5 (b), Baseline Si-P5 (d) and High Si-P5 (f).

5.4 Hardness

5.4.1 Composition

As covered in section 2.1.2, Si is a ferrite promoter as well as ferrite strengthener. It was proposed in section 2.4.1 that as the Si increased, the strength of the castings would increase. Hardness and strength are closely related; typically, as a material gets stronger, it also gets harder. By analyzing Figure 4.18, which shows the average hardness of each block as a function of distance from the chill, it can be seen that the high Si alloy had the highest overall hardness while the baseline heat had the lowest. Additionally, each alloy was distinct from the others and there was no overlap between them. There are many studies that have related an increase in Si content to an increase in hardness values (Björkgren 1997; Larker 2008) and the results of this study are in good agreement with them.

Figure 5.10 shows the hardness as a function of Si content. It is easy to see that for an increase in Si, a corresponding increase in hardness results. This result can also be seen in Figure 5.12(a). An ANOVA analysis of the data shows that Si content is significant, which was expected based on the plot below. The full results of the ANOVA analysis can be found in Appendix E.

In Donelan (2000), the author proposes an equation in which to estimate matrix hardness from the chemical composition of the DI. The equation he gives is:

$$H_m = H_f X_f + H_p X_p \quad \text{eq. (5.1)}$$

Where H_m is the hardness of the matrix and H_f and H_p are the hardness of the ferrite and pearlite phases, respectively and X_f and X_p are the fractions of ferrite and pearlite, respectively. The matrix of the test castings was nearly 100% ferrite, so the pearlite contribution shall be ignored here. The author further defines H_f as:

$$H_f = 64 + 44(\%Si) + 9(\%Mn) + 114(\%P) + 10(\%Cu) + 7(\%N) + 22(\%Mo) \quad \text{eq.(5.2)}$$

Using this equation and the results of the chemical analysis, the estimated hardness may be calculated for each alloy. The estimated and experimental values, given in Table 5.1, are in good agreement with one another.

Table 5.1
Experimental hardness values and calculated values using equation in Donelan (2000)

Alloy	Calculated	Experimental
Baseline	145	151
Medium Si	233	213
High Si	262	256

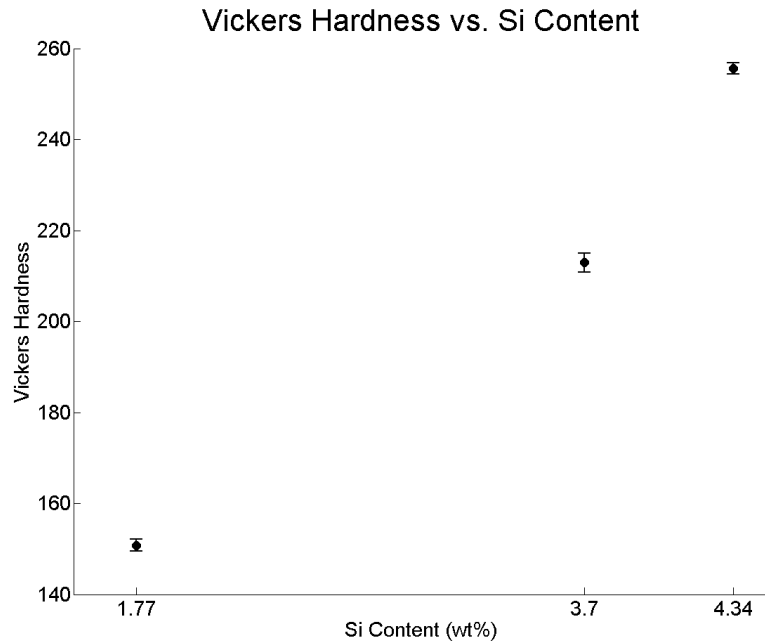


Figure 5.10: Hardness as a function of Si content. The error bars are one standard error of the mean and are small.

5.4.2 Cooling Rate

Cooling rate has the potential to dramatically affect the hardness of a sample. As hypothesized in section 2.4.2, a faster cooling rate would produce a finer microstructure. This is shown in Figure 5.13. Image (a) had a faster cooling rate than (b) and there is a clear difference in the grain size of the ferrite.

The hardness results as a function of cooling rate are shown in Figure 5.11. The data includes the effect of the Si content, creating a large standard error for the data points. It can be seen from Figure 5.12 that the cooling rate did not have an effect on the hardness of the castings. Therefore, the hardness of the matrix is a result of the chemical composition of the matrix and not its structure.

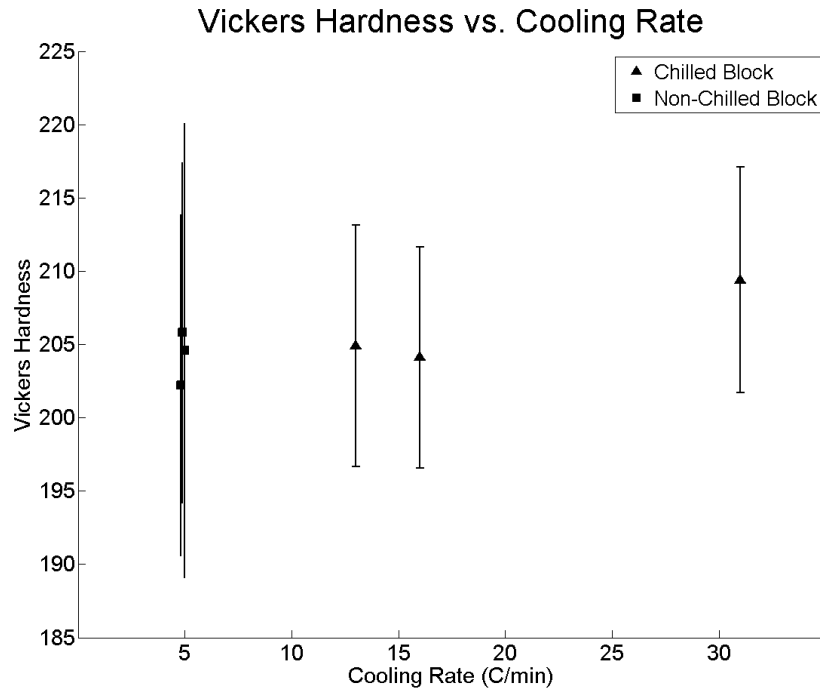


Figure 5.11: Hardness as a function of cooling rate for the chilled and non-chilled castings. The errors bars are one standard error of the mean and are large because the data includes the effect of Si content.

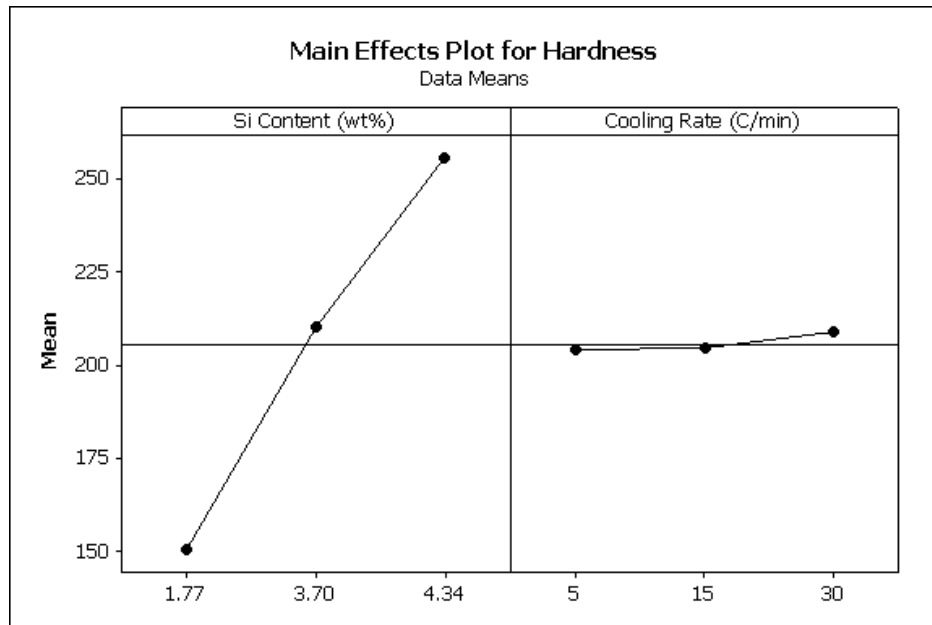


Figure 5.12: Plot showing of effect of Si content and cooling rate on hardness. From this plot it is easy to see that Si content is significant while cooling rate is not.

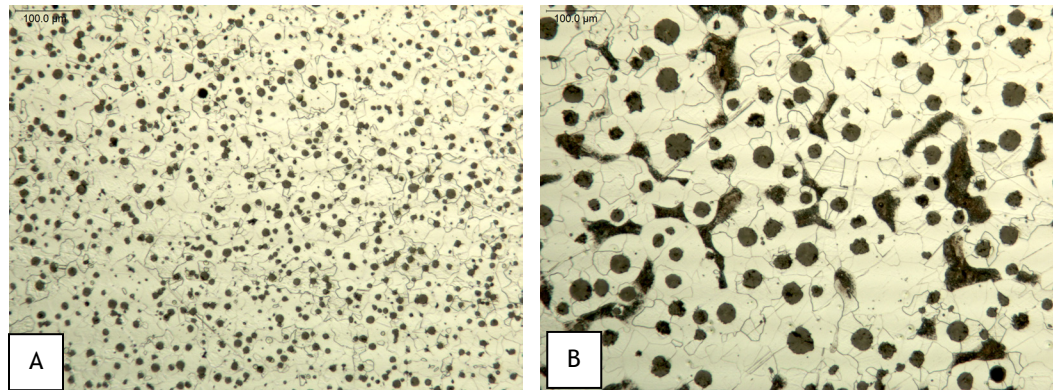


Figure 5.13: Etched micrographs of the baseline alloy showing the matrix microstructure of the test blocks. Sample Baseline-P1 (a) and Baseline-P3 show an increase in nodule size, ferrite grain size, and presence of intercellular pearlite as well as a decrease in nodule count.

5.5 Tensile Testing

5.5.1 Composition

In many studies, the use of Si is evaluated as a solid solution strengthener for producing high strength ferritic ductile irons (Björkgren 2000; Larker 2008). When Si is added to DI, it acts as a solid solution strengthener, replacing some iron atoms in the crystal lattice. This substitution of Si for Fe atoms results in a tensile lattice strain on the bonds surrounding the Si atom which, in turn, creates a strain field. The presence of a strain field is well known to inhibit the motion of dislocations within a crystal (Callister 2005). When dislocations are not allowed to move freely within a crystal, the result is a stronger, less ductile material.

The yield stress as a function of Si content is plotted in Figure 5.14. It is clear from this plot that as the Si content increases, so does the yield stress. A similar result is found when plotting the tensile strength as a function of Si content as shown in Figure 5.15. For many materials, it is common to see a decrease in ductility for a corresponding increase in strength and this is reflected in Figure 5.16. For increasing Si content, a decrease in elongation is also observed. It was noted in the literature that an as-cast DI with a high percentage of Si (3.0 - 3.8wt%) was comparable in mechanical properties to a ferritic/pearlitic grade of ductile iron, but possessed better elongation characteristics due to the fully ferritic matrix (Björkgren 2000). The same studies showed that the strength of a DI casting increased linearly with increasing Si content. In Figure 5.14 and Figure 5.15, it is easy to see this same linear relationship between the measured response and the Si content. An ANOVA analysis performed on the data indicated that Si content was a significant factor for yield stress, tensile strength and elongation, which

corresponds well with results found in the literature. The effect of Si on these properties may be seen in Figure 5.23 through Figure 5.25.

Comparing the experimental data from this study to the values found in the literature (Björkgren 2000; Larker 2008), as shown in Table 5.2, it can be seen that the results of this study are close, but slightly higher than reported. There is not a comparison to the baseline alloy since high Si contents were investigated in the literature studies.

Table 5.2 Comparison of experimentally obtained strengths to those in the literature

Alloy	Yield Strength		Tensile Strength	
	Experimental	Published	Experimental	Published
Low Si	236.29	n/a	389.50	n/a
Medium Si	457.25	400	579.30	540
High Si	535.09	480	661.32	600

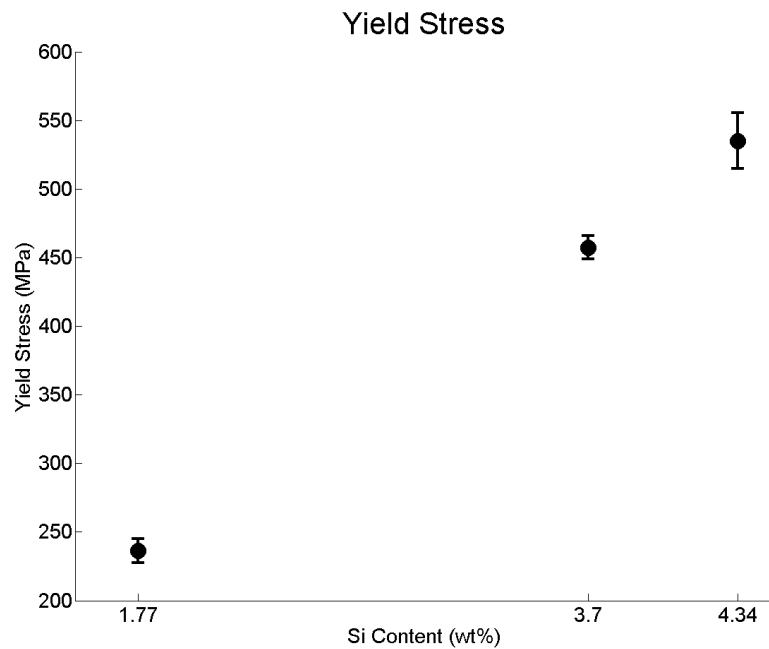


Figure 5.14: Yield stress as a function of Si content. It is clear that an increase in Si content results in an increase in yield stress. The error bars represent one standard error the mean.

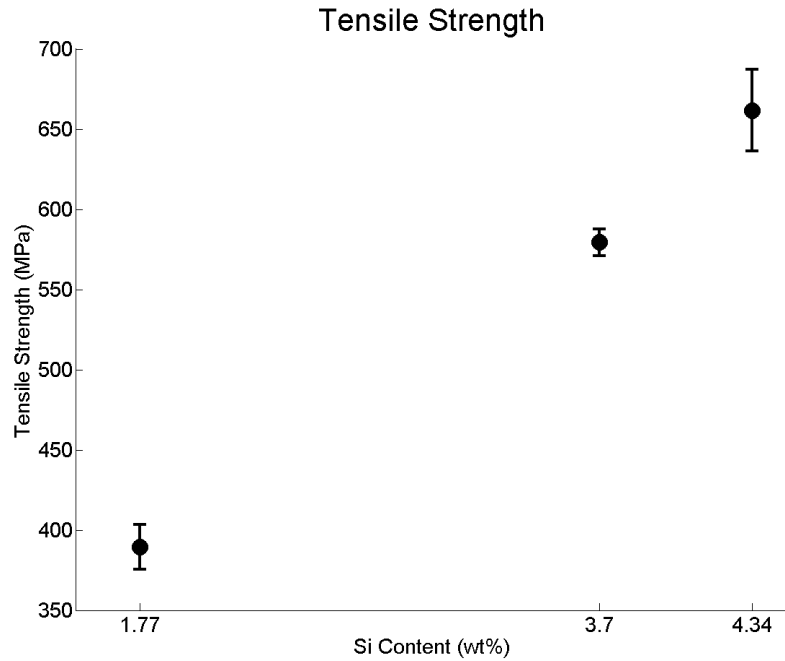


Figure 5.15: Tensile strength as a function of Si content. Just as for yield stress, as Si content increases, an increase in tensile strength results. The error bars are one standard error of the mean.

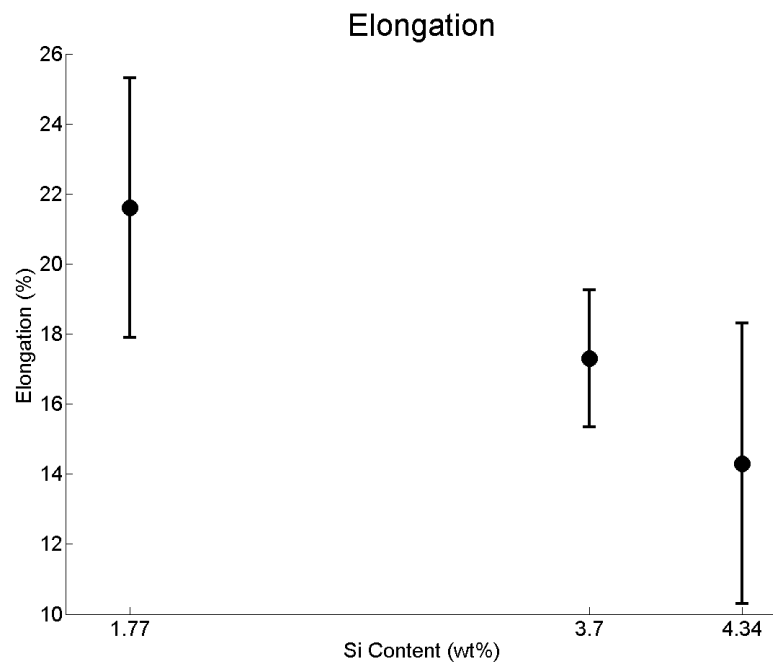


Figure 5.16: Elongation as a function of Si content. For an increase in Si, which also results in an increase in strength, there is a decrease in elongation. The error bars represent one standard error of the mean.

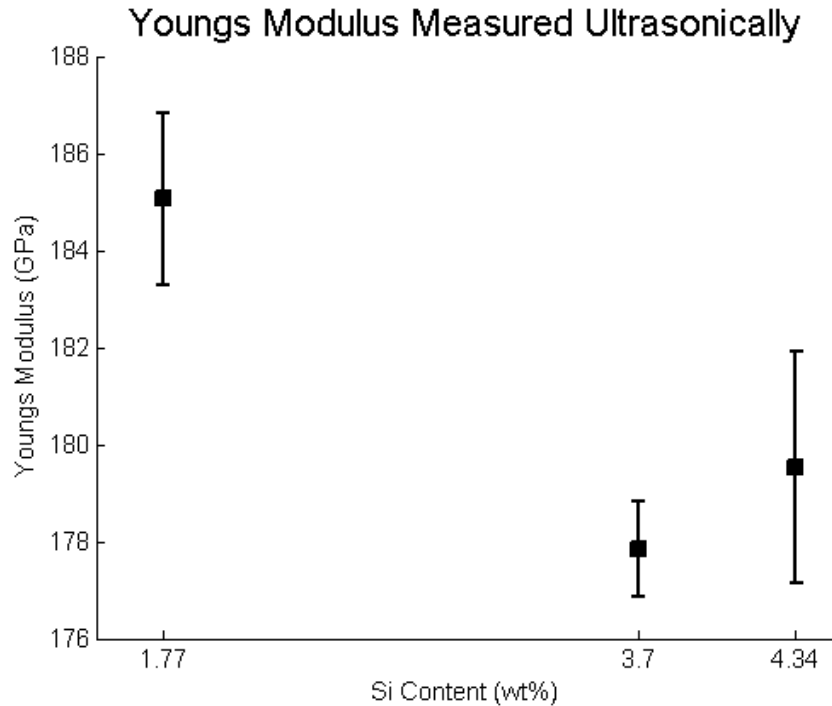


Figure 5.17: Young's modulus measure ultrasonically as a function of Si content. The error bars represent one standard error of the mean. It can be seen that for an increase in Si content, a decrease in modulus occurs.

In addition to tensile testing the moduli of the castings were determined via ultrasonic measurements. The results of modulus as a function of Si content are shown in Figure 5.17. An ANOVA analysis was performed to test the significance of the Si content on Young's modulus and it was found to be a significant factor. In general, Young's modulus is a result of the bond strength between atoms in the crystal lattice of the material. Additionally, the strain on the bonds resulting from the solid solution strengthening effect of the Si impacts the modulus and makes the material stiffer and less likely to plastically deform. It has been indicated in the literature that as the volume percent of graphite in the casting increases, or the nodules become increasingly irregular, the modulus tends to decrease (Pundale 1998).

These results of tensile testing and ultrasonic modulus measurement support the first hypothesis listed in section 2.4.1 which stated that as the Si content increased, the strength should also increase.

5.5.2 Cooling Rate

The effect of cooling rate was also evaluated in the ANOVA analysis. For the analysis, the cooling rates were binned with center point values of 5, 15 and 30. A plot of yield stress as a function of cooling rate is given in Figure 5.19 and a nearly identical plot of tensile strength is given in Figure 5.20. The

elongation and Young's modulus as a function of cooling rate are shown in Figure 5.21 and Figure 5.22, respectively. Although a correlation is hard to discern from these plots, an ANOVA analysis for cooling rate as a factor for yield stress, tensile strength and elongation showed it to be significant. The same analysis for Young's modulus indicated that cooling rate was not a significant factor.

Cooling rates are highly effective in helping to control microstructure; a fast cooling rate results in a high nodule count and a fine grain size. From the Hall-Petch relationship, an increase in yield stress is expected for smaller grain sizes. Qualitatively, it was noted that the smallest grain sizes occurred at the chill/casting interface, where the cooling rate was fastest. Correspondingly, it is in these regions where the highest yield stresses and tensile strengths were observed, a phenomenon also observed in the literature (Gilbert 1970). Small grain sizes serve to increase the yield stress by presenting barriers to dislocation motion (Callister 2005). A greater number of barriers (grain boundaries) results in a higher yield stress, which was observed. Figure 5.18 shows the microstructure of the baseline alloy. Image (a) had a faster cooling rate than (b) and consequently had higher yield stress/tensile strength values. The sample in (a) also had a higher elongation than the one pictured in (b).

Elongation of a material is typically inversely related to strength: as strength increases, the elongation decreases. This relationship was observed with respect to Si content. However, as shown in Figure 5.21, the elongation increased with an increase in cooling rate. This is in agreement with Marks (1999) which stated that an increase in nodule count results in an increase in elongation.

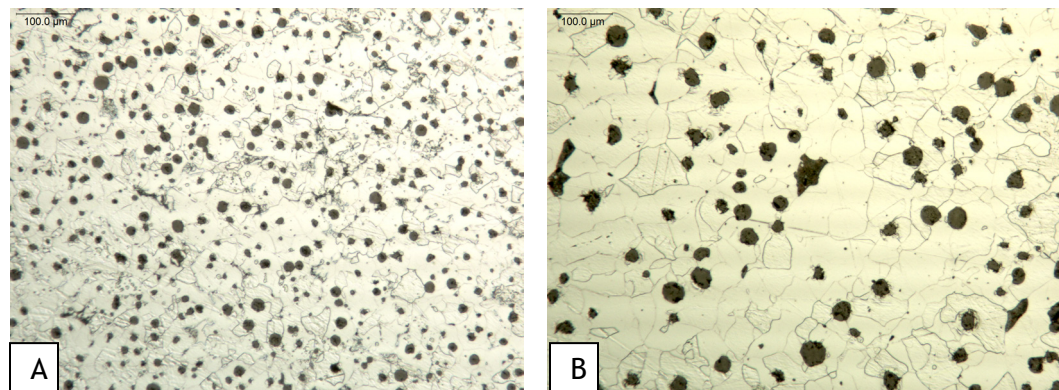


Figure 5.18: Comparison of cooling rate for the baseline alloy. Image (a) is from the sample closest to the chill while (b) is from the center of non-chilled block. The grain size in (a) is much finer than in (b) and this was reflected in the strength of the material. The yield stress/tensile strength for (a) and (b) were 240MPa/398MPa and 224MPa/373MPa, respectively.

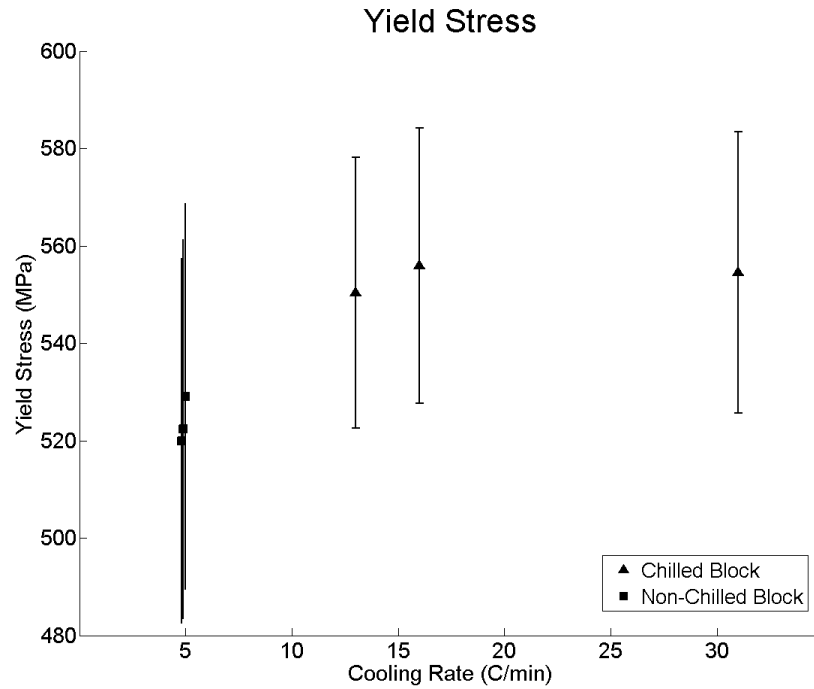


Figure 5.19: Yield stress as a function of cooling rate. The error bars are one standard error of the mean and are large because they include the effect of Si. A correlation is difficult to discern, but ANOVA showed that cooling rate is a significant factor for yield stress.

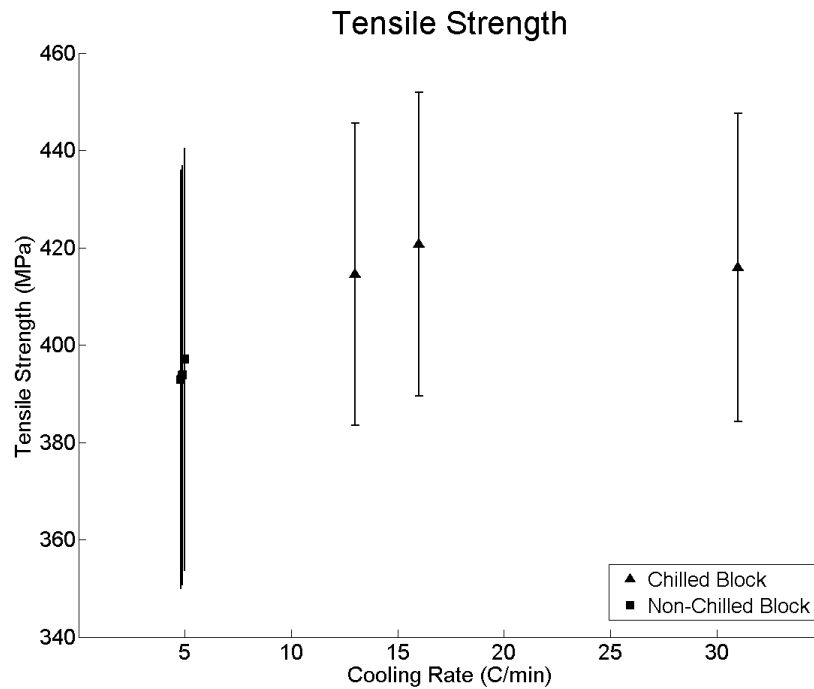


Figure 5.20: Tensile strength as a function of cooling rate. The error bars are one standard error of the mean and are large because they include the effect of Si on the tensile strength.

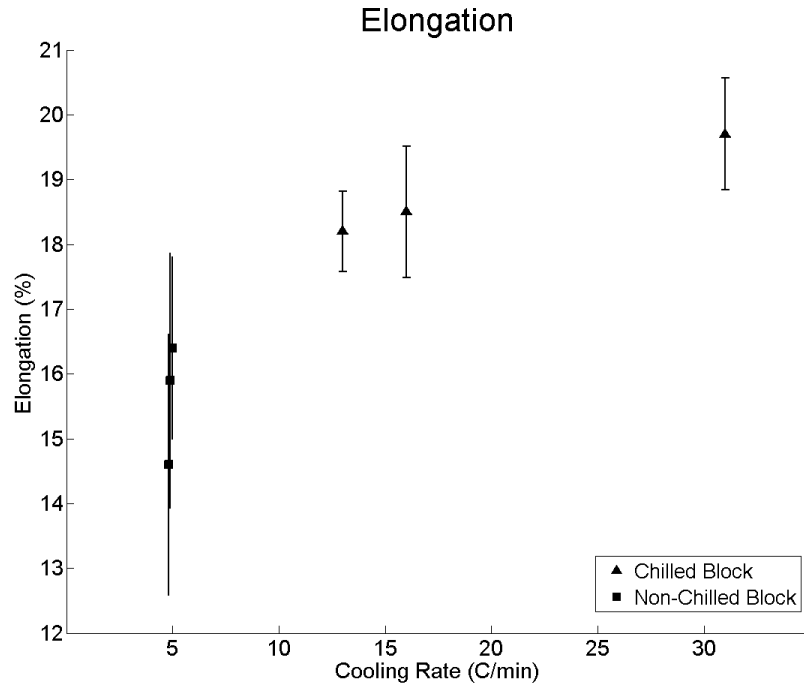


Figure 5.21: Elongation as a function of cooling rate. The error bars are for one standard error of the mean and include the effect of Si causing them to be large.

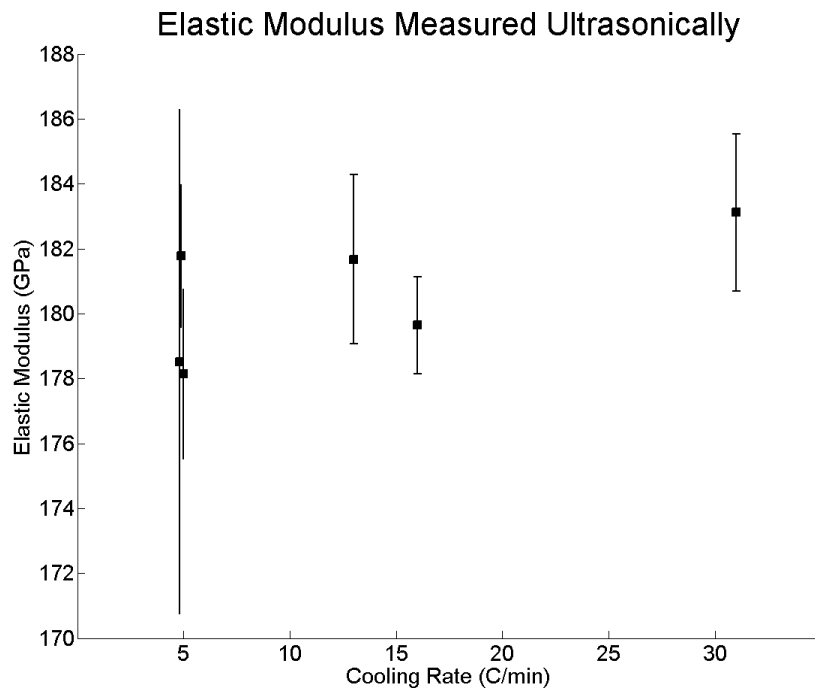


Figure 5.22: Young's modulus as a function of cooling rate. The error bars are for one standard error of the mean and include the effect of Si resulting in a large error.

It was found that cooling rate was a significant factor for tensile strength, yield stress and strain, but not for Young's modulus. An increase in cooling rate always resulted in an increase in strength and elongation. There was no discernable effect of cooling rate on the Young's modulus as seen in Figure 5.22.

5.5.3 Relative Effect of Si Content and Cooling Rate

Figure 5.23 through Figure 5.26 show the effect of Si content and cooling rate on the various mechanical properties previously discussed. Both factors were significant for yield stress, tensile strength and elongation, but only Si (and not cooling rate) was significant for Young's modulus. Additionally, from analysis of the plots, it can be seen that in Figure 5.23 and Figure 5.24 the Si content is a much larger factor for the yield and tensile strength than the cooling rate. However, in Figure 5.25 (elongation), the cooling rate is a larger factor than the Si content. An increase in Si content results in an increase in yield and tensile strength, but a decrease in elongation and Young's modulus while an increase in cooling rate results in an increase yield and tensile strength as well as elongation. The mechanisms for this were previously detailed.

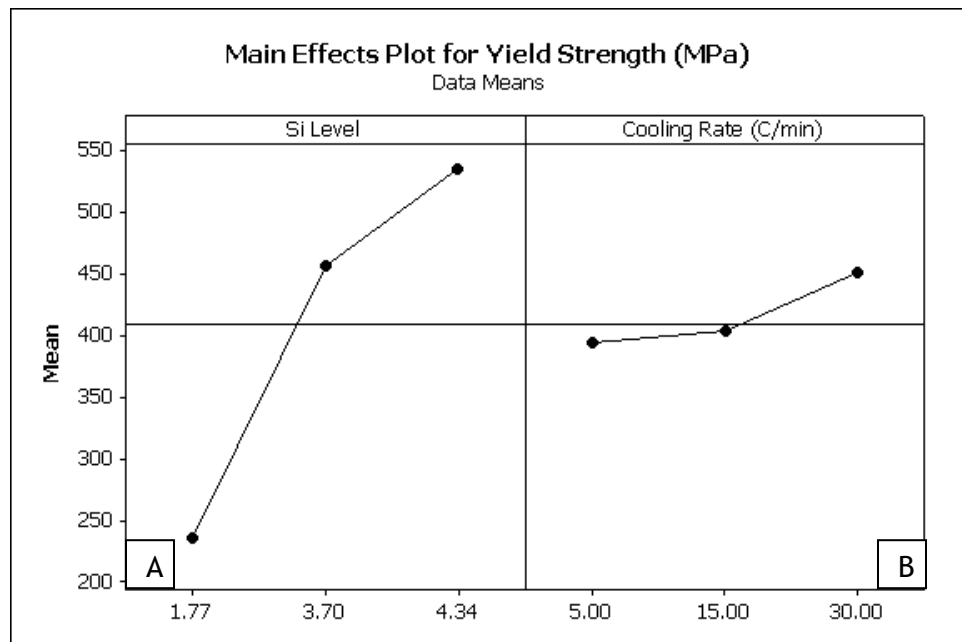


Figure 5.23: Effect of cooling rate and Si content on yield stress. Both factors are significant and an increase in either factor will result in an increase in yield stress.

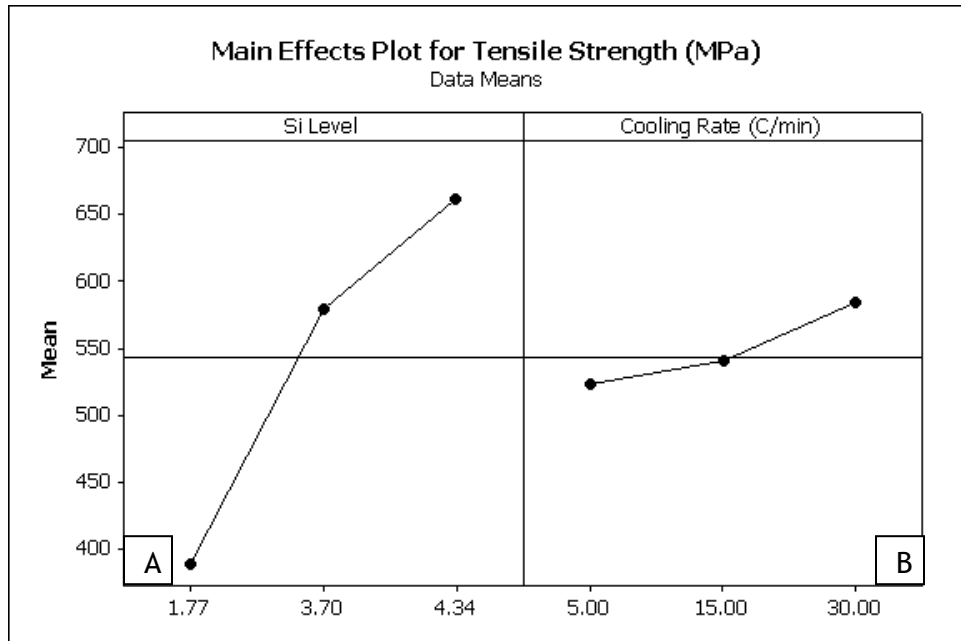


Figure 5.24: Effect of cooling rate and Si content on tensile strength. Both factors are significant and an increase in either will result in an increase in tensile strength.

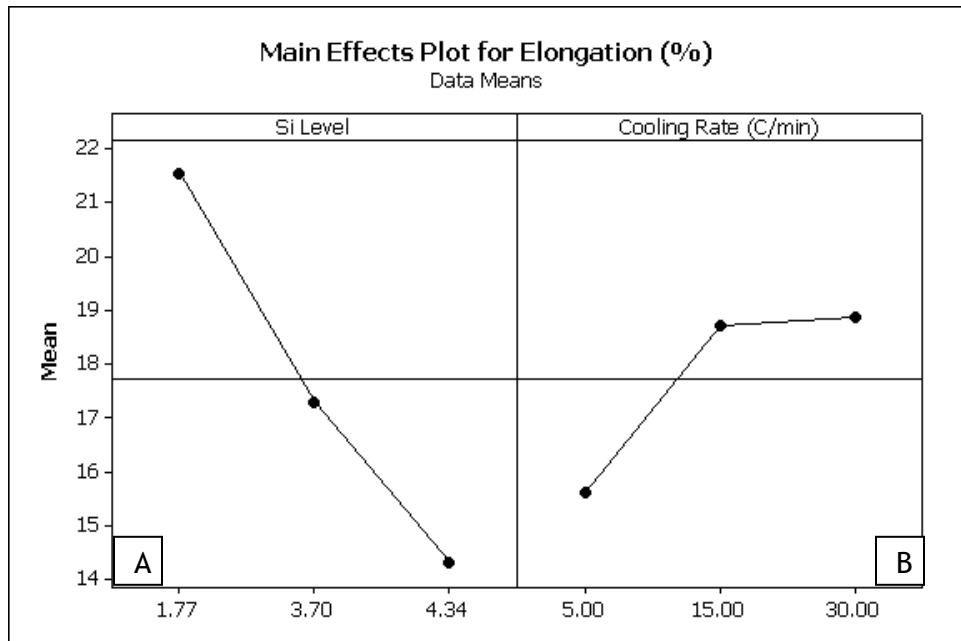


Figure 5.25: Effect of cooling rate and Si content on elongation. Both factors are significant and an increase Si results in decreased elongation while an increase in cooling rate can increase the elongation.

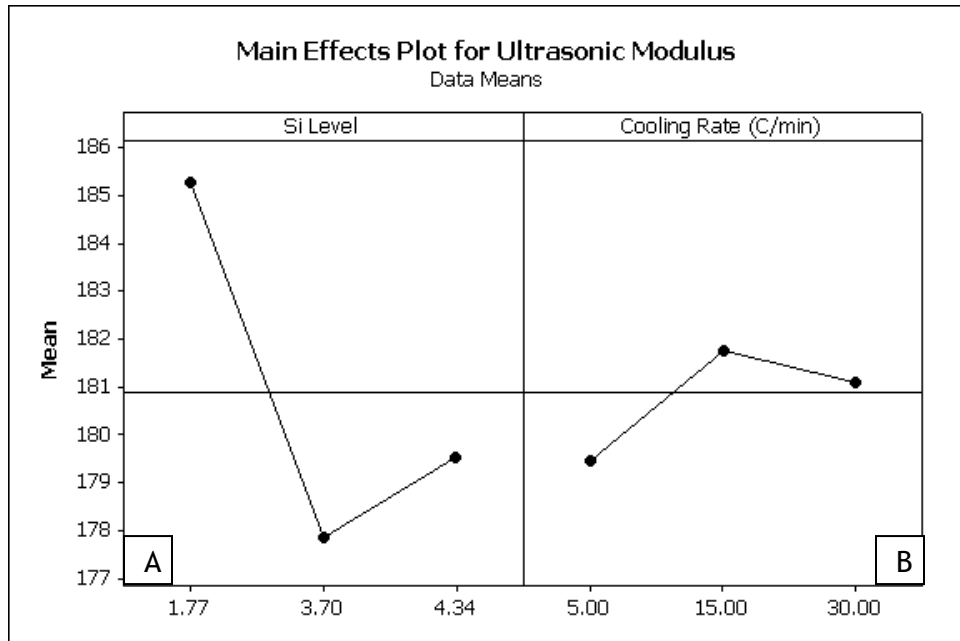


Figure 5.26: Effect of cooling rate and Si content on ultrasonic modulus. Si content is significant while cooling rate is not. An increase in Si content will decrease Young's modulus of the casting.

5.6 Impact Toughness

5.6.1 Composition

The impact toughness of the material was found to vary considerably between the alloys, as seen from Table 4.10. It is well known that the addition of Si increases the DBTT of ductile iron, but the mechanism by which this occurs was not described in detail. CONCEPT OF WORK Recall that in the introduction, Figure 2.1 showed the impact curves for different Si contents as a function of impact temperature. This figure indicates that as the Si content increase, the DBTT, which is defined as the inflection point of an impact-temperature curve, increases. Figure 5.27 shows the impact energy of the castings as a function of temperature. The error bars represent one standard error of the mean. As seen in the figure, the baseline alloy had the highest impact energy compared to the medium and high Si alloys. This indicates that the baseline alloy has a DBTT lower than -40°C while the other two alloys have a DBTT higher than 25°C . It may then be concluded that an increase in Si content causes an increase in the DBTT, which correlates well with the literature.

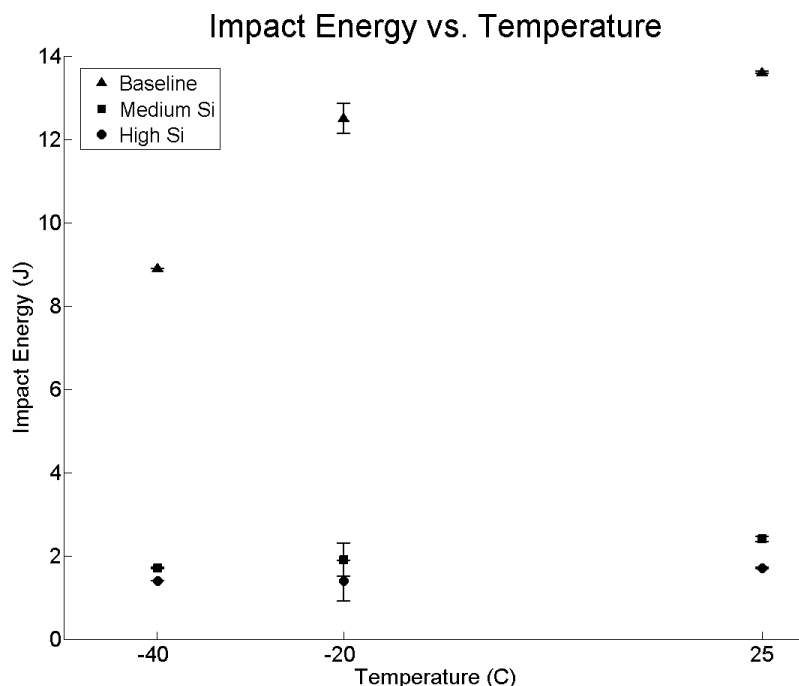


Figure 5.27: Impact energy for the three alloys as a function of impact temperature. By comparing the three alloys, it can be seen that the baseline had the highest impact energies for all temperatures while the medium and high Si alloys has the lowest.

A comparison of the experimental data to results in the literature may be seen in Figure 5.28. Each data point is averaged over the chilled and non-chilled blocks at each temperature. In other words, all data points, regardless of chill condition, that were tested at the same temperature were averaged to obtain the data points. The points are indicated and an estimated curve is drawn through them. The baseline alloy has a Si content of 1.77wt%, which is close to one of the curves shown in the figure and may be compared to it. The other two alloys do not have a specific curve to which they may be compared. The 1.8wt%Si curve shows a higher upper shelf energy for the same temperatures than the experimental data. This is likely a result of microstructural features of the sample than the Si content, since the strength was higher than given in the literature. It also appears as if the DBTT for the baseline alloy is lower than for the 1.8wt%Si. The curves for the medium and high Si alloys indicate that the DBTT increases for increasing Si content. Although it is difficult to make a conjecture regarding the upper shelf energy of the medium and high Si alloys, it is likely that it is less than the 2.95wt%Si.

An ANOVA analysis was then performed to test the significance of the Si content on the impact toughness. The results indicated that Si content was a significant factor. A plot showing the effect of Si content on the impact energy is shown in Figure 5.30.

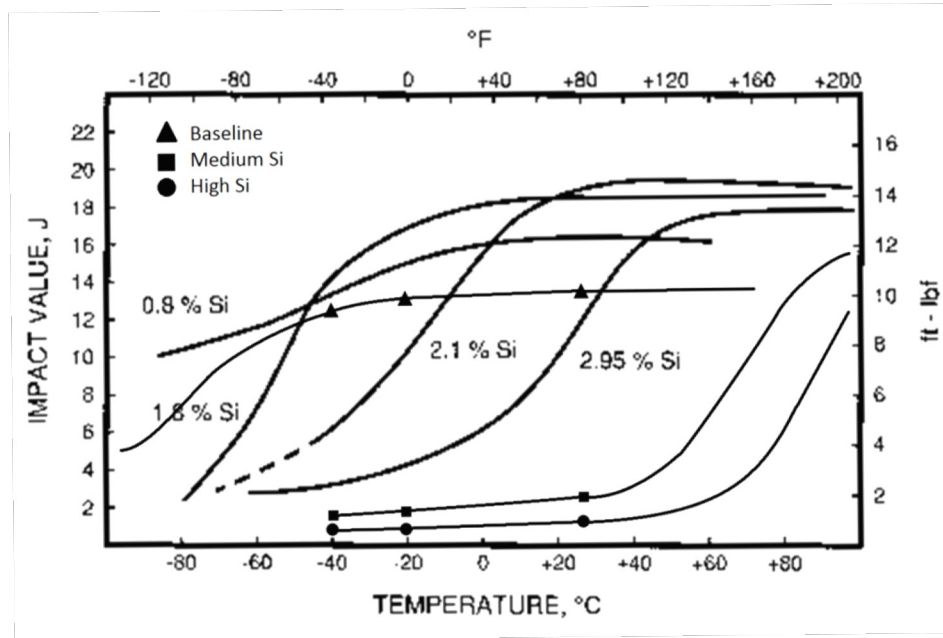


Figure 5.28: Figure from the Ductile Iron Society showing the impact energy vs. temperature for different Si alloys. The data from this study has been placed on the plot for comparison. (Image reprinted from Ductile Iron Society 1990)

5.6.2 Cooling Rate

The effect of the cooling rate on the impact toughness was also evaluated. As previously stated, the faster cooling rates created a finer microstructure and higher nodule counts. An ANOVA analysis revealed that this was not a significant factor; however, the data was only based on two samples per temperature per alloy.

Figure 5.29 shows the results of the impact testing for the alloys and compares the chilled and non-chilled blocks. As can be seen in the baseline results, the chilled block has a lower impact energy for all temperatures. As indicated in the literature, an excessively high nodule count can be detrimental to the impact toughness of a casting (Labrecque 2010). The chilled castings had a nodule count that was 130 nodules/mm² higher than the non-chilled castings. Therefore it is reasonable to conclude that a higher nodule count for the baseline alloy decreases the impact toughness and that an optimal nodule count exists and is less than 250 nodules/mm². In the case of the medium Si alloy, there is not a discernible difference between the chilled and non-chilled castings indicating that the nodule counts of this alloy did not have an effect on impact toughness. The nodule count of the high Si chilled castings was nearly 160 nodules/mm² higher than for the same, non-chilled alloy. While there is not a difference at the low temperatures, the increase in nodule count appears to have been beneficial for room temperature impact toughness.

A comparison of the upper shelf energy of the medium and high Si alloys is not possible, but it is possible to compare the baseline alloy to the 1.8wt%Si curve in Figure 5.28. The results of the impact energies for the baseline alloy are relatively constant over the three test temperatures; therefore, it is assumed that these values are representative of the upper shelf energy. Comparing these to the 1.8wt%Si curve, it is seen that the experimental upper shelf energy is less than those in the literature. In Labrecque (2010), it is noted that the upper shelf energy may be negatively affected by a high nodule count.

One of the most important results of impact testing is determining the DBTT. By once again comparing the baseline results to the 1.8wt%Si curve, it is possible to see that the DBTT of the experimental casting is lower than the DBTT of the curve shown in the figure. Additionally, by examining the extrapolated curves for the medium and high Si alloys, it can be seen that the DBTT increases with the Si content. Gilbert (1970) indicates that a smaller grain size can decrease the DBTT for cast DI. This was observed for the baseline alloy, but could not be determined for the medium and high Si alloys.

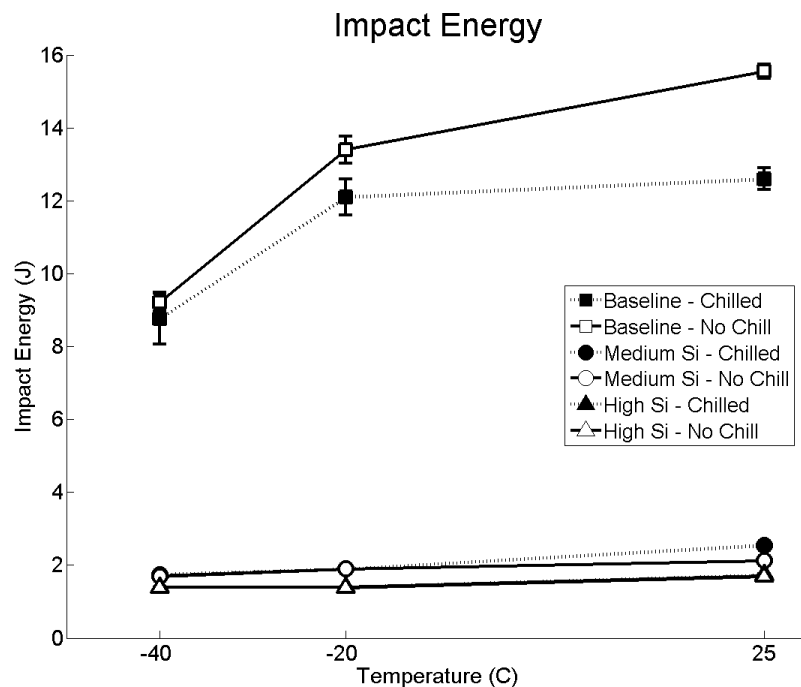


Figure 5.29: Impact energy as a function of temperature. The medium and high Si impact energies for the chilled samples are the same as the non-chilled samples and are, therefore, not visible on this graph.

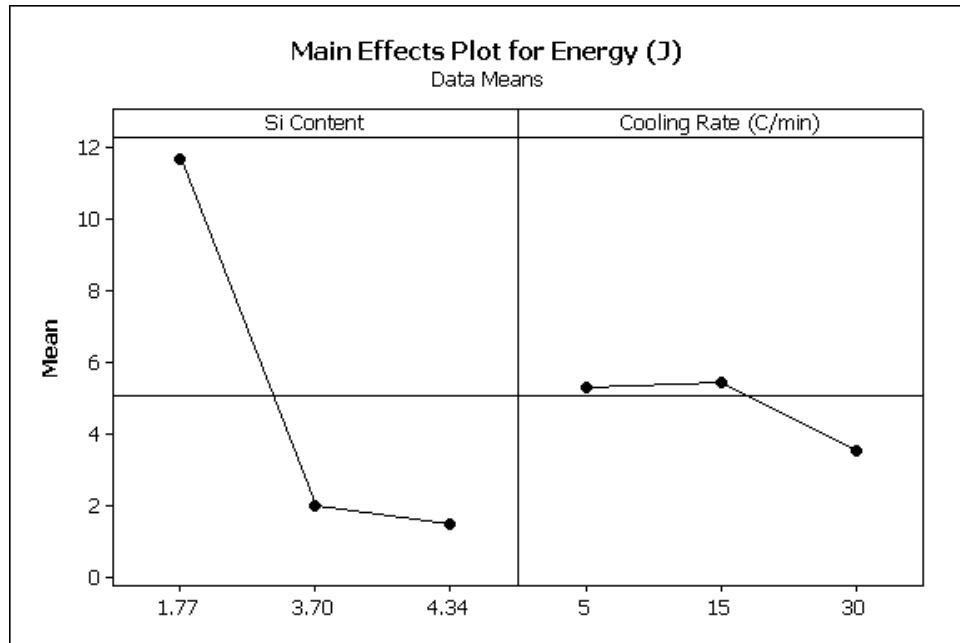


Figure 5.30: Plot showing effect of Si content and cooling rate on impact energy.

5.6.3 Relationship Between Impact Energy, Elongation and Tensile Strength

The results of the Charpy tests are given in Table 4.10. It is important to note that the unit for impact energy is Joules. These are the same units as work, and as such, the two are closely related. Work is defined as the product of force and distance. In the case of a material, these may be thought of as stress and strain, respectively. A multiple regression analysis was performed on the data to predict the impact energy based on the tensile strength and elongation, but a definitive equation relating both factors could not be found. The regression did indicate that the tensile strength was significant to the impact energy while elongation was not. The regression equation from the analysis is given in equation 5.3. The R^2 value of the equation is 0.95.

$$\text{Impact Energy} = 30.78 - 0.05 * \text{Tensile Strength} \quad \text{eq. (5.3)}$$

However, an exponential fit describes the data much better, as shown in Figure 5.31. As expected, an increase in tensile strength results in an exponential decrease in impact energy. This fit may be used to better predict the impact energy based on the tensile strength of a casting, but caution should be exercised.

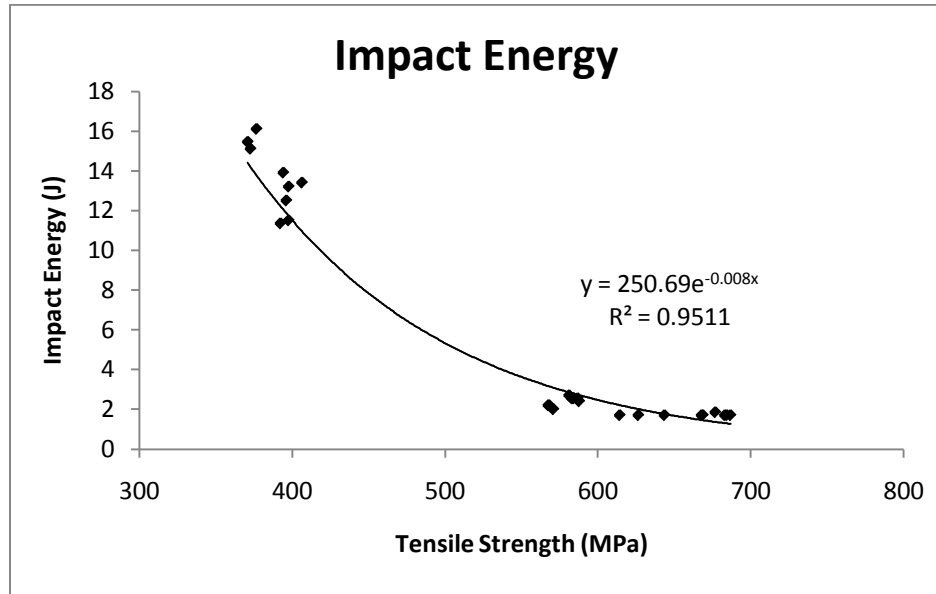


Figure 5.31: Plot showing impact energy as a function of tensile strength and the equation for the line of best fit. This shows that for an increase in tensile strength, a large decrease in impact energy results.

By referring to Table 4.9 and Table 4.10, it may be qualitatively noted that as the tensile strength increases, the elongation and percent shear decrease. A regression analysis revealed that the tensile strength was a significant factor for predicting percent shear, but elongation was not. Performing the regression again, this time neglecting the elongation factor, the following regression equation is given in equation 5.4. The R^2 value for this equation was high, 0.85, indicating a good fit with the data.

Eq 5.1

Further work needs to be done to establish a reliable relationship between tensile strength, elongation and impact energy.

6 Conclusions

Three test castings were prepared - baseline, medium Si and high Si alloys - and the cooling rate was varied via the presence of chills. By casting three blocks at the same time with different cooling rates, the variables associated with casting were eliminated. The microstructure and mechanical properties were evaluated at different locations within each casting to determine if there was a difference between them as a result of cooling rate and/or Si content.

6.1 Hypothesis 1 - Effect of Composition

In this study, it was hypothesized that the addition of Si to a ferritic ductile iron would increase its strength but cause a decrease in fracture toughness. This was found to be correct. The addition of Si to the castings caused an increase in yield stress, tensile strength, and hardness as a result of the solid solution strengthening effect. Furthermore, it was responsible for a decrease in elongation and Young's modulus.

The addition of Si was also found to affect the nodule count and nodularity of the castings. An increase in the Si content resulted in an increase in nodule count but a decrease in nodularity. This can, in turn, affect the mechanical properties of a casting since a high nodule count can increase strength and elongation and poorly formed nodules may act as stress concentrators.

The effect of Si addition to the castings was often a larger factor for the measured responses than the cooling rate.

6.2 Hypothesis 2 - Effect of Cooling Rate

A difference in cooling rate was expected between the active and passive chills, but none was found via statistical analysis of the data. The only difference noted between the chills was the amount of recalescence exhibited in the baseline alloy at locations close to the chill. However, the chill:casting ratio was large and in cases when this ratio is much smaller, it would be reasonable to expect a difference.

Although the cooling rate was, statistically, a smaller factor than the Si content of a casting for many properties, it was the primary influence on the microstructure of the castings. There was not a significant difference between the actively and passively chilled blocks; however, the presence of the chills did have an effect when compared to the non-chilled casting. The chilled casting had higher nodule counts and nodularity and finer grain sizes compared to the non-chilled blocks. These finer microstructures resulted in a higher yield and tensile strength, following the Hall-Petch relationship, greater elongation and a decrease in DBTT for the baseline alloy. The increase in DBTT as a result of the faster cooling rate does not overcome the extreme increase

caused by an increase in Si content. Some samples had very high nodule counts of >350 nodules/mm². The high counts resulted in a decrease in impact toughness and upper shelf energy. It is therefore implied that an optimum nodule count exists.

References

- Asenjo I, Larranaga P, Sertucha J, Suarez R, Gomez JM, Ferrer I, Lacaze J. 2007. Effect of mould inoculation on formation of chunky graphite in heavy section spheroidal graphite cast iron parts. *International Journal of Cast Metals Research* 20(6):319-324.
- Association WWE. 2011. World Wind Energy Report 2010. World Wind Energy Association.
- Basutkare PK, Loper CR, Babu CL. Solidification of Heavy Section Ductile Iron Castings. *AFS Transactions* [Internet].429-434.
- Björkgren LE, Hamberg K. 2000. Silicon alloyed ductile iron with excellent ductility and machinability. *International CIATF Conference*. Paris, France.
- Callister WDJ. 2005. *Fundamentals of Materials Science and Engineering*. John Wiley and Sons, Inc.
- Cho GS, Choe KH, Lee KW, Ikenaga A. 2007. Effects of alloying elements on the microstructures and mechanical properties of heavy section ductile cast iron. *Journal of Materials Science & Technology* 23(1):97-101.
- Donelan P. 2000a. Modelling microstructural and mechanical properties of ferritic ductile cast iron. *Materials Science and Technology* 16(3):261-269.
- Donelan P. 2000b. Modelling microstructural and mechanical properties of ferritic ductile cast iron *Journal of Materials Science and Technology* 16:261-269.
- Ecob CM. A Review of Common Metallurgical Defect in Ductile Cast Iron. Available from: <http://www.elkem.no/dav/dfa48df95b.pdf>
- Gilbert JNG. 1970. *Ductility of Cast Irons With Special Reference to Impact Properties*.
- Goodrich GM. 1997. Cast Iron Microstructure Anomalies and Their Causes. *Transactions of the American Foundrymen's Association* 104:669 - 683.
- Hayrynen K. 1988. *Heavy Section Ductile Cast Iron: Production and Segregation*. [Houghton, MI]: Michigan Technological University. p. 126.
- Helmink RC, Wallace JI. 1977. *Ductile Iron Society Report No. 8: Factors Affecting Optimum Properties in Heavy Section Ductile Iron*. Mountainside, NJ.
- Hoover HWJ. 1986. A Literature Survey of Degenerate Graphite in Heavy Section Ductile Iron. *Transactions American Foundrymen's Society* 94:86 - 102.
- Hughes ICH. 1988. Ductile Iron. In: Davis JR, editor. *Metals Handbook*. 9th ed. Metals Park, OH: ASM International. p. 647 - 666.

- Karsay SI. 1970. Control of Graphite Structure in Heavy Ductile Iron Castings. American Foundry Society Transactions 78:8.
- Khajure R. **INFLUENCE OF VARIOUS PROCESS PARAMETERS ON PHYSICAL AND MECHANICAL PROPERTIES OF DUCTILE IRON CASTINGS.** 114th AFS Metalcasting Congress; 2010; Orlando, FL: American Foundry Society.
- Labrecque C. 2010. Ductile Iron Characteristics and Impact Strength at Low Temperature. In: Cabanne P-M, Muratore EC, editors. AFS Proceedings: American Foundry Society. p. 10.
- Labrecque C, Cabanne PM. 2011. Low temperature impact strength of heavy section ductile iron castings: effects of microstructure and chemical composition. China Foundry 8(1):66-73.
- Larker R. 2008. Solution Strengthened Ferritic Ductile Iron ISO 1083/JS/500-10 Provides Superior Consistent Properties in Hydraulic Rotators. Keith Millis Symposium on Ductile Cast Iron. Las Vegas, NV: The Ductile Iron Society.
- Marks JR. 1999. Metallography of Ductile Iron. Transactions of the American Foundrymen's Society 107:819-827.
- Nakamura S, Sakamoto N, Inoue K, Ogi K, Matsuda K. 1989. As-Cast Heavy Section Ferritic Spheroidal Graphite Cast Iron. Transactions of the American Foundrymen's Society 97:6.
- Pundale SH, Rodgers RJ, Nadkarni GR. 1998. Finite Element Modeling of Elastic Modulus in Ductile Iron: Effect of Graphite Morphology. AFS Transactions 106:7.
- Puttenat D. 2008. REpower Systems AG installs prototype of the REpower 3.XM onshore wind turbine near Husum, Germany. Google.
- Radzikowska JM. 2005. Effect of specimen preparation on evaluation of cast iron microstructures. Materials Characterization 54(4-5):287-304.
- Riposan I, Chisamera M, Stan S. 2010. Performance of heavy ductile iron castings for windmills. China Foundry 7(2):163-170.
- Rundman K. Metal Casting (Reference Book for MY4130). Houghton, MI: Michigan Technological University. p. 150.
- Shy YH, Hsu CH, Lee SC, Hou CY. 2000. Effects of titanium addition and section size on microstructure and mechanical properties of compacted graphite cast iron. Materials Science and Engineering a-Structural Materials Properties Microstructure and Processing 278(1-2):54-60.
- Society DI. Ductile Iron Data for Design Engineers [Internet]. Available from: <http://www.ductile.org/didata/default.htm>
- Sprengler AF. 1995. Ductile Iron Society Report No. 23: Determining the relationship Between Solidification Time and Mechanical Properties of Heavy Section Ductile Iron Castings. North Olmsted, OH: Ductile Iron Society.

Standardization TGI. 1997. EN 1563 Founding - Spheroidal graphite cast iron.

Thrury W. **PREVENTION OF SOME FAULTS IN SPHEROIDAL GRAPHITE IRON CASTINGS.**

Quality Control of Engineering Alloys and the Role of Metals Science
Symposium; 1977; Delft, the Netherlands. p. 8.

Tiedje NS. 2010. Solidification, processing and properties of ductile cast iron.
Materials Science and Technology 26(5):505-514.

Appendix A Mass Balance and Charge Determination for Each Heat

Mass balances are required for each heat in order to obtain the required chemistry using a mix of material from various sources (see Table 3.3 for complete list). The mass balances are performed using the following generic equation:

$$wt\%X = \frac{\sum(m_i * wt\%X_i)}{\sum m_i}$$

Where X is the element of interest and *m* is the weight of each material added to the charge. This process was performed in Microsoft Excel for simplicity. Equations for each of the six elements of interest for each alloy are given below. Note that yields determined from experience and prior heats are used in the equations.

Alloy: Baseline (Heat H110419)

Table A.1
Charge material chemistries and final melt chemistry for the baseline alloy

Material	Weight (lbs)	C	Si	Mg	P	Mn	S
Steel	55	0.03	0.01	0.001	0.008	0.14	0.014
Pig Iron - Sorel	245	4.26	0.21		0.005	0.005	0.007
Graphite	2.25	99.7					0.03
FeMn	0.6	6.72				75.1	
Foundrisil	1		74.9				
Mg Treatment	3.5		44.4	5.55			
Foundrisil	3.6		74.9				
Germalloy	1.19		78.0				
Calculated:	312	3.7	2.07	0.037	0.005	0.17	0.004
Target:	300	3.7	2.00	0.039	0.025	0.18	0.005

Wt.% C:

$$\frac{55(0.03) + 245(4.26) + 2.25(99.7) + 0.6(6.72)}{312} * 0.90 = 3.7\text{wt\% C}$$

Wt.% Si:

$$\frac{55(0.01) + 245(0.21) + 1(74.9) + 3.5(44.4) + 3.6(74.9) + 1.19(78.0)}{312} * 0.90$$

$$= 2.07\text{wt\% Si}$$

Wt.% Mg:

$$\frac{55(0.001) + 3.5(5.55)}{312} * 0.60 = 0.037\text{wt\% Mg}$$

Wt% P:

$$\frac{55(0.008) + 245(0.005)}{312} = 0.005\text{wt\%P}$$

Wt% Mn:

$$\frac{55(0.14) + 245(0.005) + .6(75.1)}{312} = 0.17\text{wt\%Mn}$$

Wt% S:

$$\frac{55(0.014) + 245(0.007) + 2.25(0.03)}{312} * 0.5 = 0.004\text{wt\%S}$$

Alloy: Medium Si (Heat H110413)

Table A.2
Charge material chemistries and final melt chemistry for the medium Si alloy

Material	Weight (lbs)	C	Si	Mg	P	Mn	S
Steel	40	0.03	0.01	0.001	0.008	0.14	0.014
Pig Iron - Sorel	180	4.26	0.21		0.005	0.005	0.007
Graphite	0.25	99.7					0.03
FeMn	0.75	6.72				75.1	
Returns - Small	27	3.74	2.4		0.015	0.28	0.005
Returns - Large	44	3.76	2.4		0.017	0.33	0.005
Foundrisil	6.75		74.9				
Mg Treatment	4.25		44.4	5.55			
Foundrisil	4		74.9				
Germalloy	1.32		78.0				
Calculated:	308	3.070	3.81	0.042	0.008	0.28	0.007
Target	300	3.2	3.65	0.045	0.025	0.28	0.005

Wt% C:

$$\frac{40(0.03) + 180(4.19) + .25(99.7) + .75(6.72) + 27(3.74) + 44(3.76)}{308} * 0.9$$

$$= 3.07\text{wt}\%C$$

Wt.%Si:

$$\frac{40(0.01) + 180(0.21) + 27(2.4) + 44(2.4) + 6.75(74.9) + 4.25(44.4) + 4(74.9) + 1.32(78)}{308} *$$

$$0.90 = 3.81\text{wt}\%Si$$

Wt.%Mg:

$$\frac{40(0.001) + 4.25(44.4)}{308} * 0.60 = 0.042\text{wt}\%Mg$$

Wt.% P:

$$\frac{40(0.008) + 180(0.005) + 27(0.015) + 44(0.017)}{308} = 0.008\text{wt}\%P$$

Wt.%Mn:

$$\frac{40(0.14) + 180(0.005) + .75(75.1) + 27(0.28) + 44(0.33)}{308} = 0.28\text{wt\%Mn}$$

Wt.%S:

$$\frac{40(0.014) + 180(0.007) + .25(0.03) + 27(0.005) + 44(0.005)}{308} = 0.007\text{wt\%S}$$

Alloy: High Silicon (Heat H110504)

Table A.3
Charge material chemistries and final melt chemistry for the high Si alloy

Material	Weight (lbs)	C	Si	Mg	P	Mn	S
Steel	50	0.03	0.01	0.001	0.008	0.14	0.014
Pig Iron - Sorel	105	4.26	0.21		0.005	0.005	0.007
Graphite	1	99.7					0.03
FeMn	0.45	6.72				75.1	
Returns - Large	132	3.76	2.4		0.017	0.33	0.005
Foundrisil	6.5		74.9				
Mg Treatment	4.15		44.4	5.55			
Foundrisil	4.5		74.9				
Germalloy	1.32		78.0				
Calculated:	305	3.09	4.28	0.045	0.010	0.28	0.007
Target	300	3.05	4.25	0.045	0.025	0.25	0.005

Wt.%C:

$$\frac{50(0.03) + 105(4.26) + 1(99.7) + .45(6.72) + 132(3.76)}{305} * 0.9 = 3.09\text{wt}\%C$$

Wt.%Si:

$$\frac{50(0.01) + 105(0.21) + 132(2.4) + 6.5(74.9) + 4.15(44.4) + 4.5(74.9) + 1.32(78.0)}{305} * 0.9$$

$$= 4.28\text{wt}\%Si$$

Wt.%Mg:

$$\frac{50(0.001) + 4.15(5.55)}{305} * 0.5 = 0.45\text{wt}\%Mg$$

Wt.%P

$$\frac{50(0.008) + 105(0.005) + 132(0.017)}{305} = 0.01\text{wt}\%P$$

Wt.%Mn:

$$\frac{50(0.14) + 105(0.005) + 0.45(75.1) + 132(0.33)}{305} = .28\text{wt}\%Mn$$

Wt.%S:

$$\frac{50(0.014) + 105(0.007) + 1(0.03) + 132(0.005)}{305} = 0.007\text{wt}\%S$$

Appendix B Photomicrographs of Test Castings

HEAT: Baseline

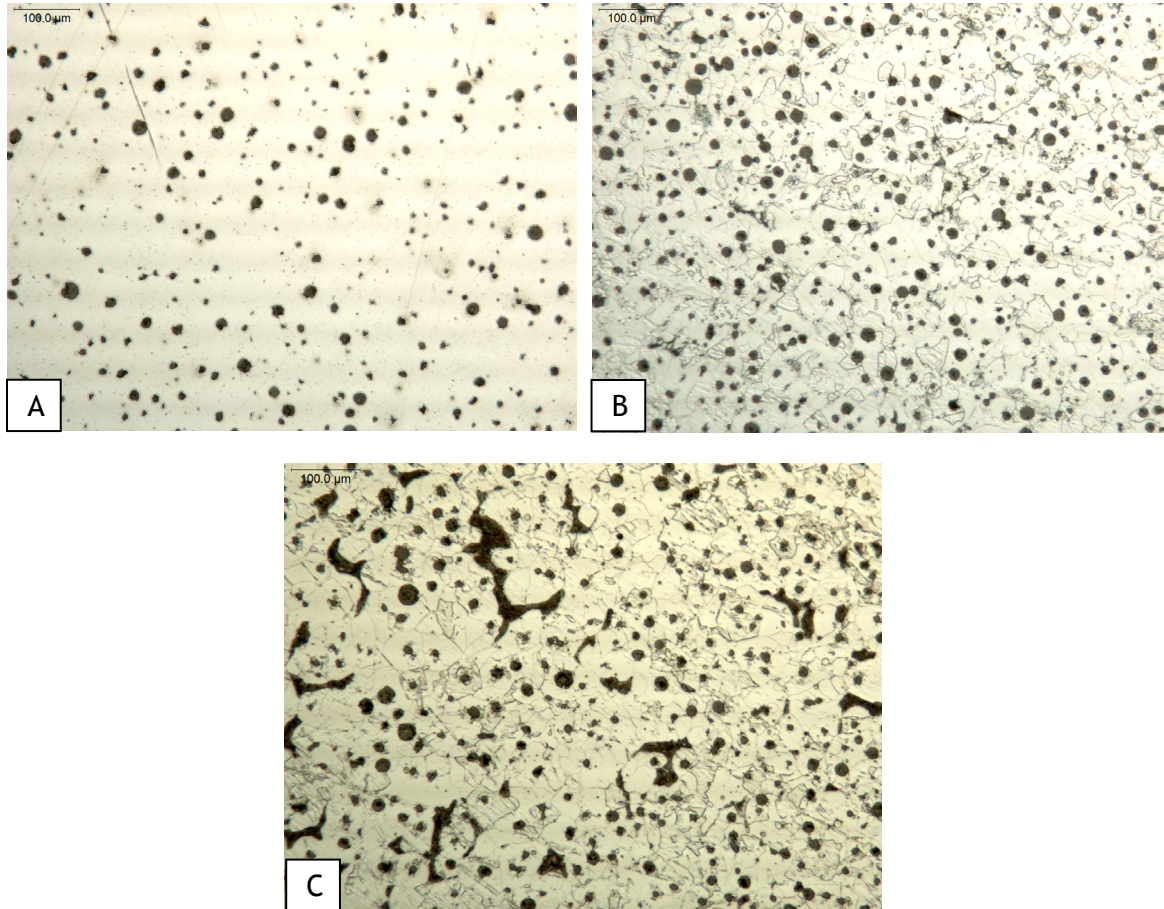


Figure B.1: Baseline-A1. (a) and (b) are from close to the surface while (c) is from further inside the casting. Note decrease in nodule count and the appearance of pearlite in (c) compared to (a) and (b)

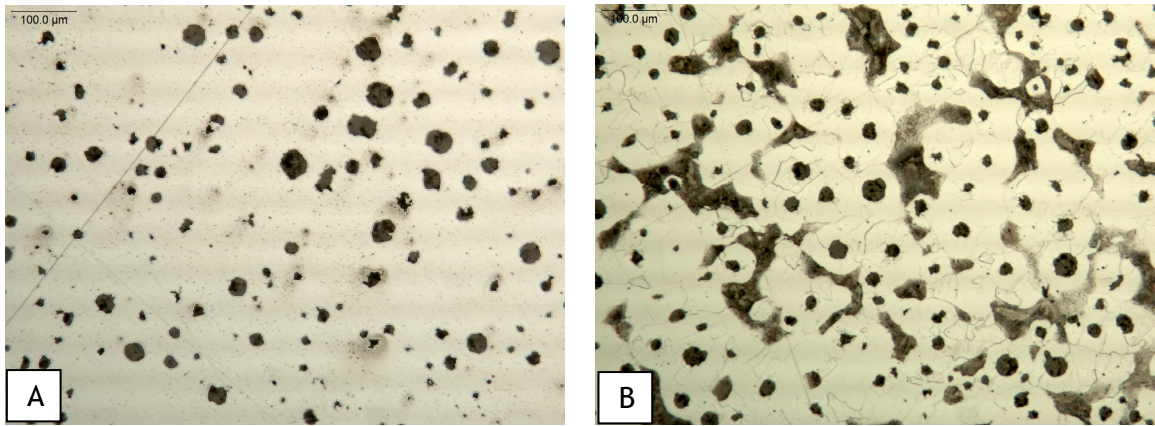


Figure B.2: Micrographs of sample Baseline-A3. Image (a) is taken at 100x in the as-polished condition while (b) is taken at 50x after being etched with 2% Nital. There is relatively the same amount of intercellular pearlite present as in Baseline-A1.

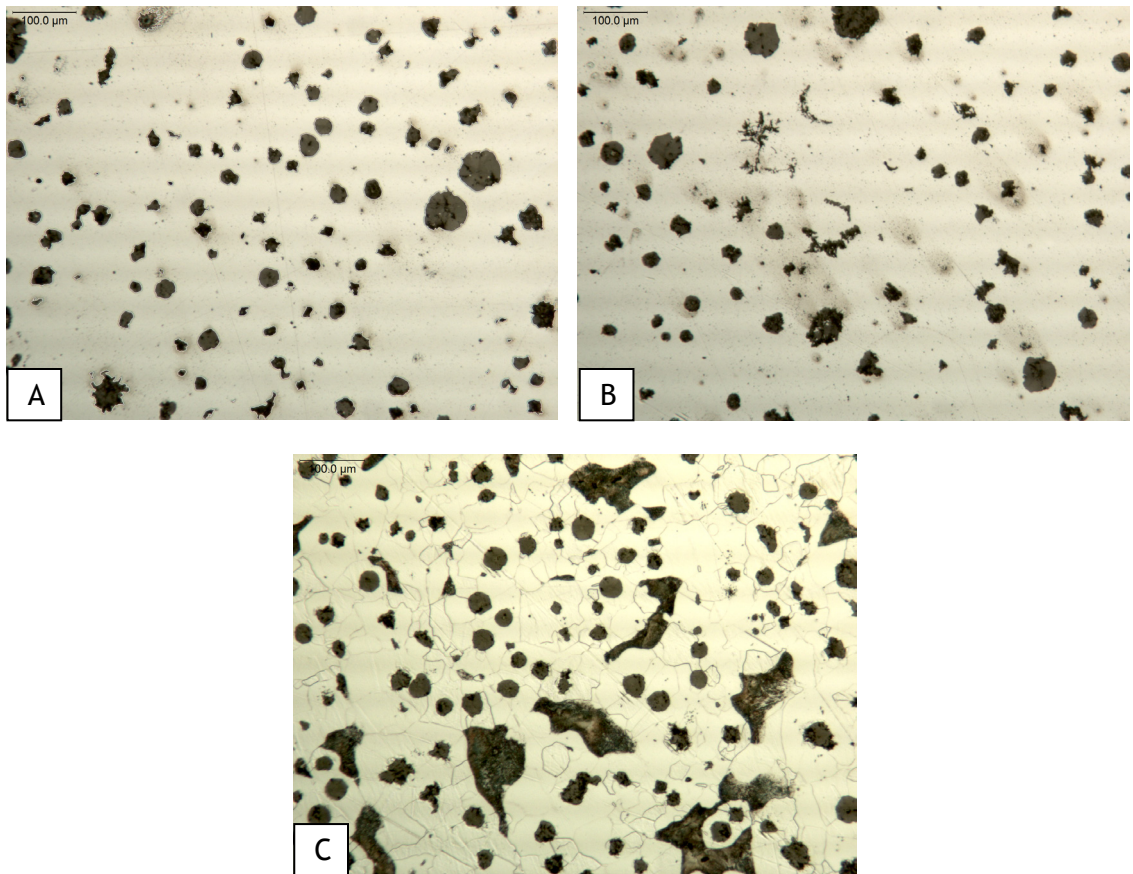


Figure B.3: Baseline-A5. Note the larger intercellular pearlite colonies present in (c) and the degenerate graphite that begins to appear in (b). (a) shows a representative area of the sample. Additionally, this sample shows larger graphite nodules when compared to Baseline-A1 and -A3.

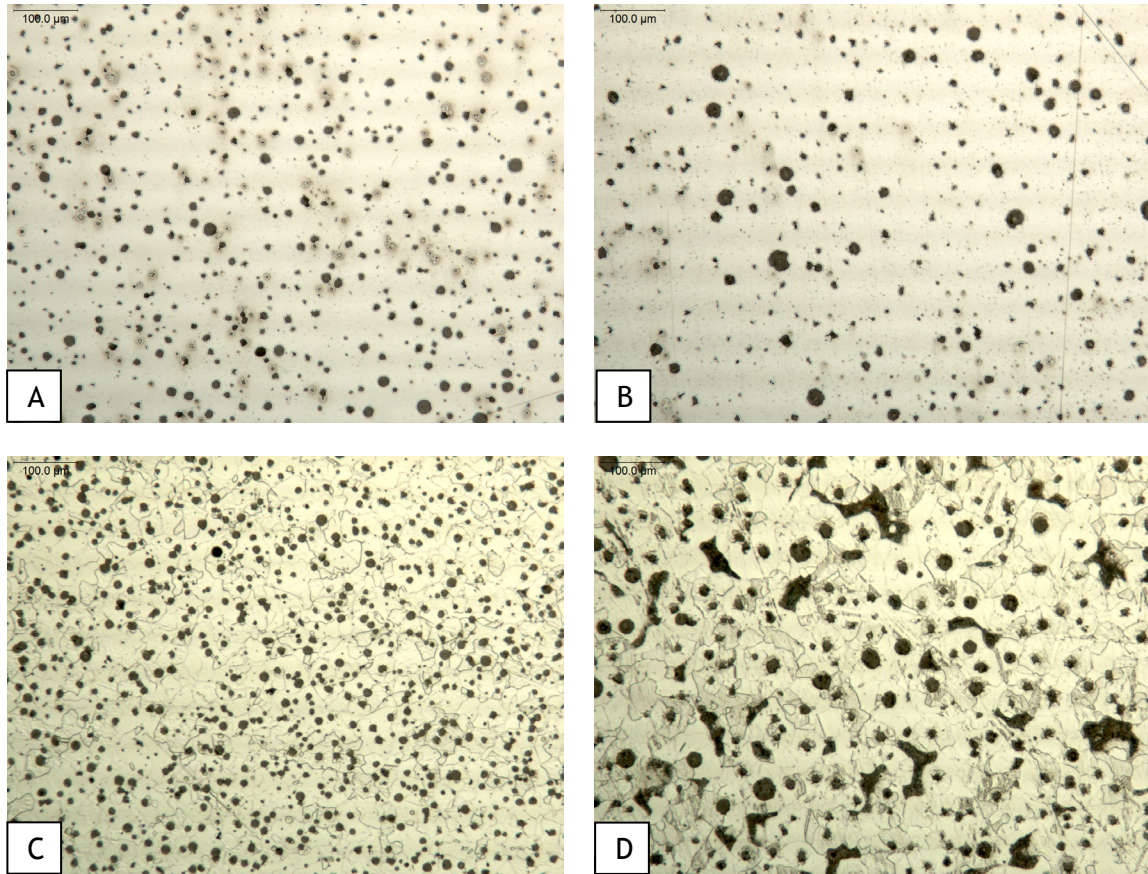
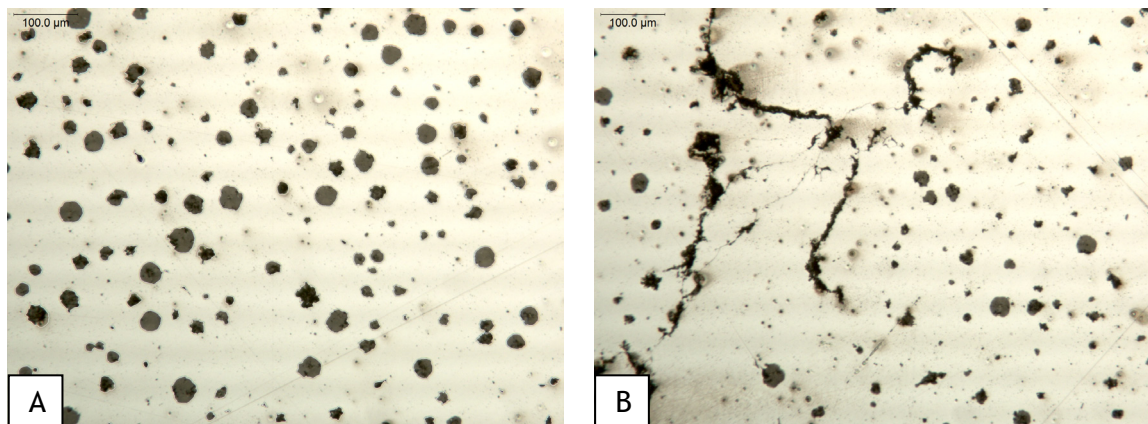


Figure B.4: Baseline-P1. Images (a) and (c) are taken close to the chill/casting interface while (b) and (d) are taken further away. Note the decrease in nodule count and increase in nodule size ((a) and (b)) and the increase in ferrite grain size ((c) and (d)) as distance from the chill increases.



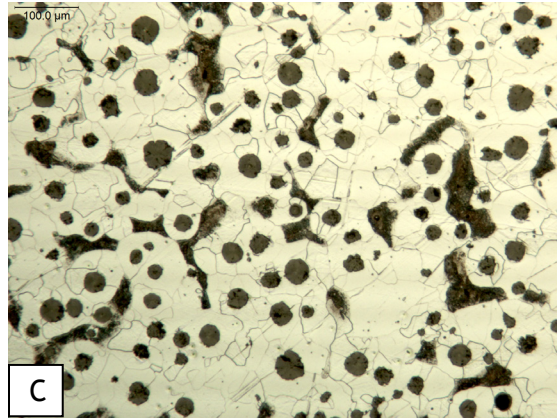


Figure B.5: Baseline-P3. Image (a) shows a representative area of the sample while (b) shows the presence of degenerate graphite. When comparing (c) with Figure B.4 (d), it is apparent that there is an increase in the size of the intercellular pearlite colonies. An increase in nodule size can also be seen by comparing Figure B.4 (a) and (b) with (a) above.

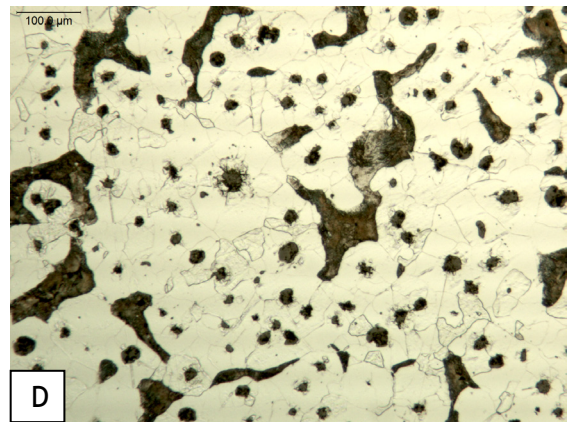
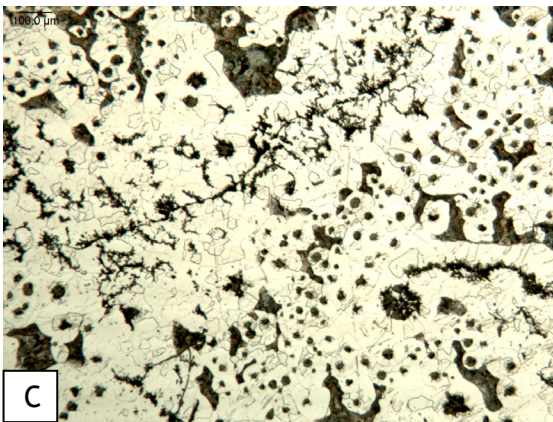
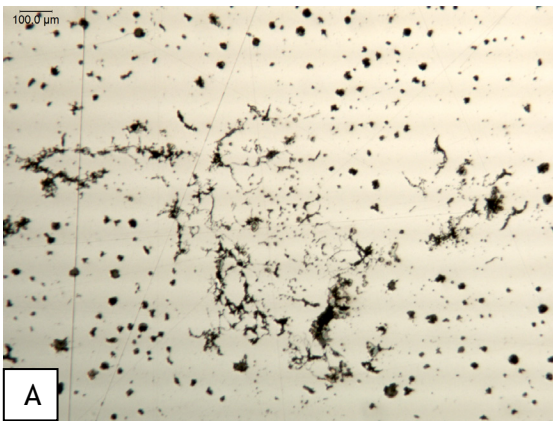


Figure B.6: Baseline-P5. A dramatic decrease in nodule count compared to Figure B.4 can be seen in (b). Image (a) shows the presence of chunky graphite. Additionally, (c) shows degenerate graphite

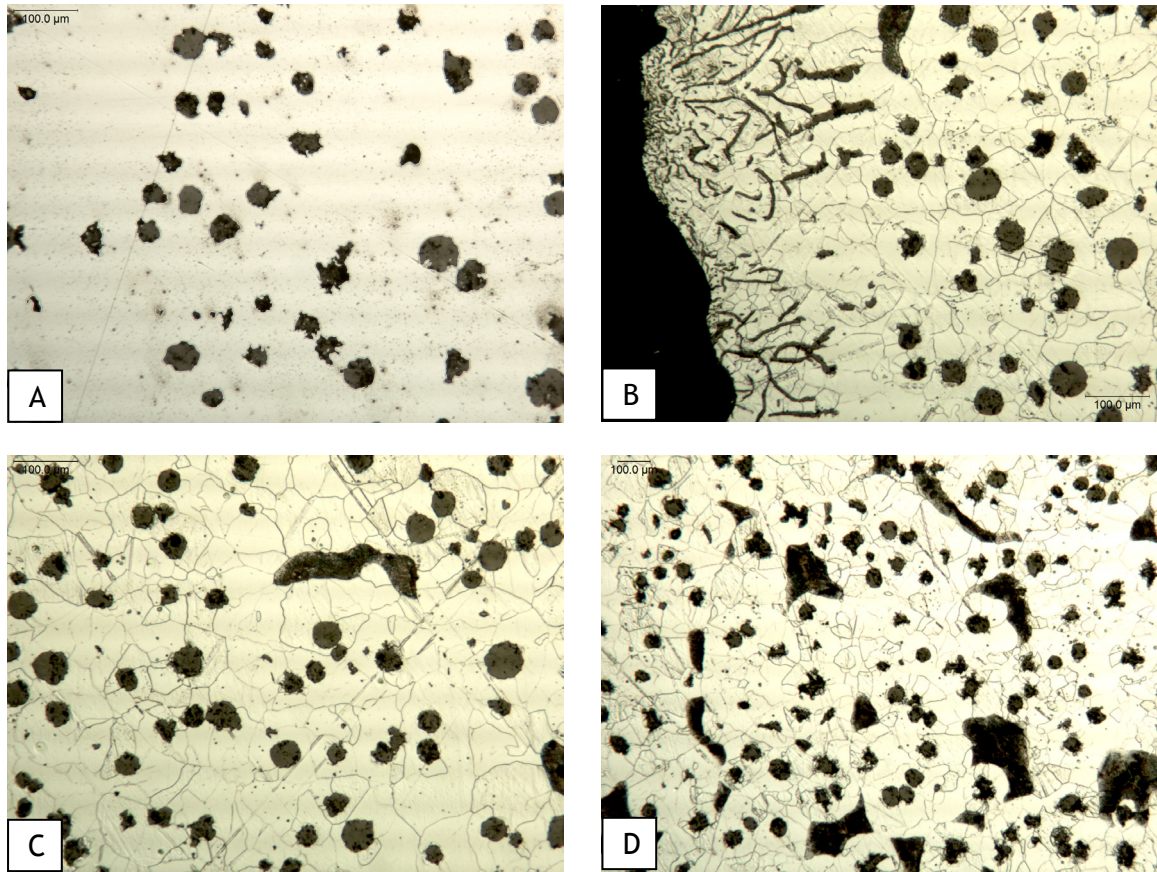
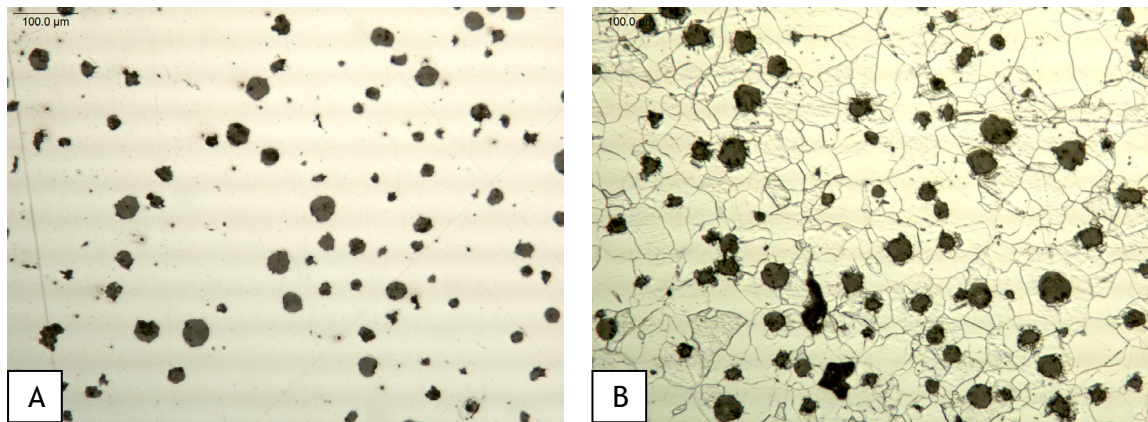


Figure B.7: Baseline-N1. Note that (a) shows larger and fewer nodules than the Baseline-A and Baseline-P blocks. Additionally, there was flake graphite at the casting surface (b). Pearlite was present close to the surface (c), but became more prevalent as distance from the surface increased (d).



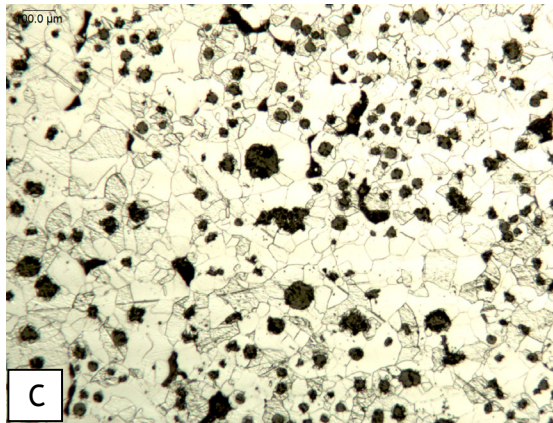


Figure B.8: Baseline-N3. Nodule count has improved, but it is still inferior to the actively and passively chilled blocks. Nodularity has also deteriorated (b). Presence of intercellular pearlite has decreased (c).

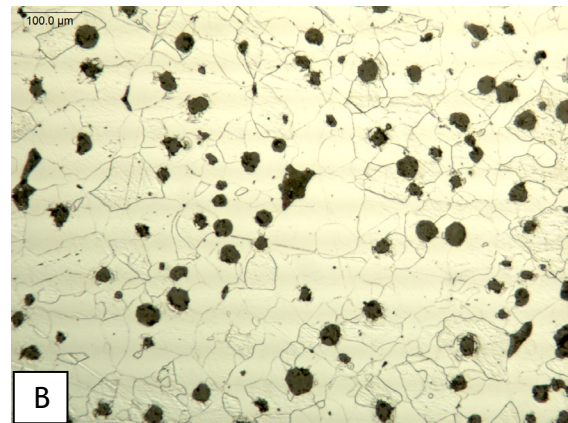
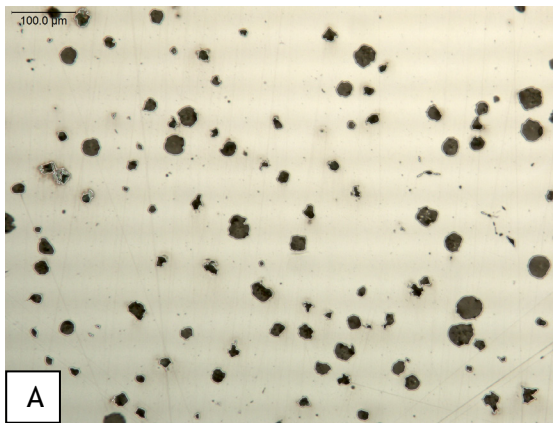


Figure B.9: Baseline-N5. The nodule count is about the same compared to Baseline-N3 in (a). Less intercellular pearlite is present as shown in (b).

HEAT: Medium Si

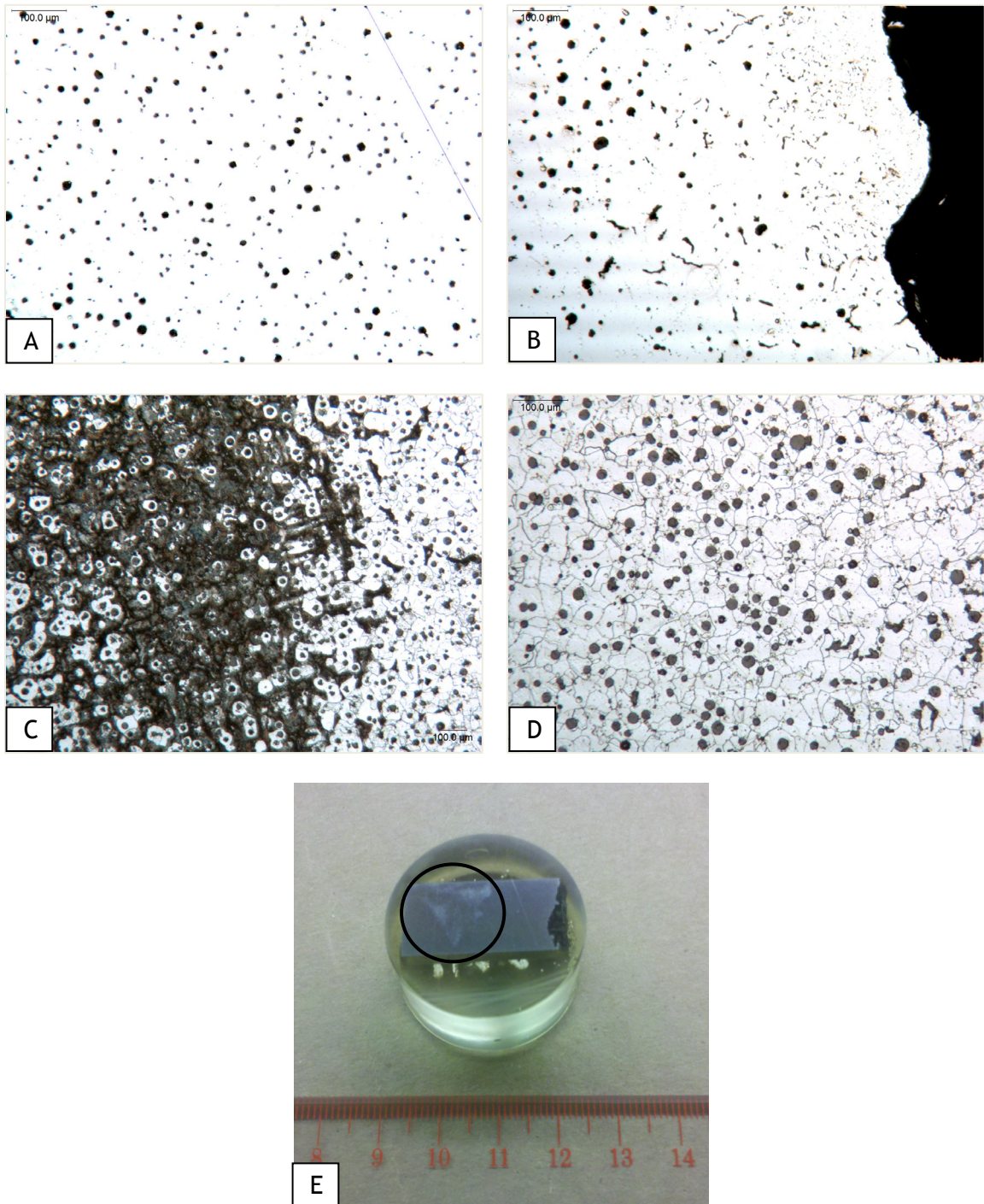


Figure B.10: Medium Si-A1. The nodule count in this sample was very high at the chill/casting interface (a); however, there was some degenerate graphite present at the surface (b). This sample had a region of pearlite (c) that was also visible macroscopically (e). Image (d) shows a representative area

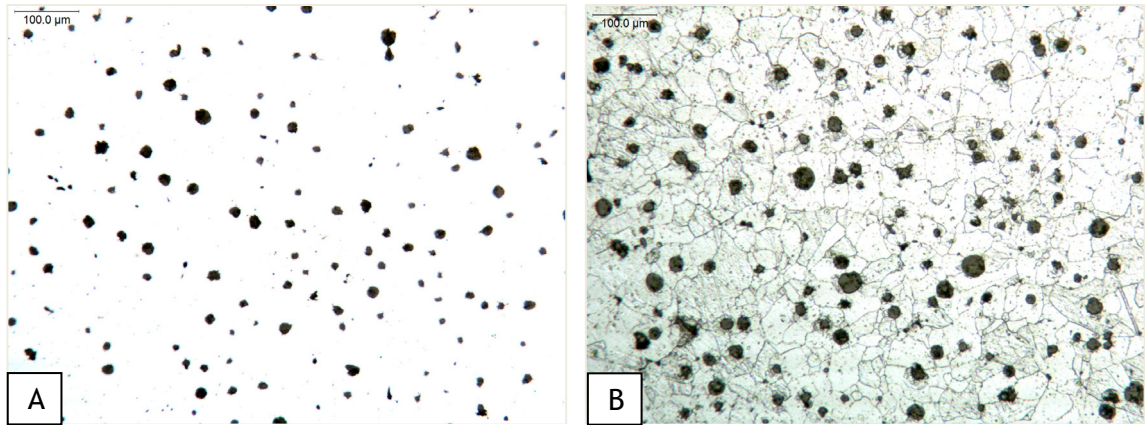


Figure B.11: Medium Si-A3. Both (a) and (b) are representative of the sample. Very little degenerate graphite and pearlite were present and there was a bimodal distribution in nodule size.

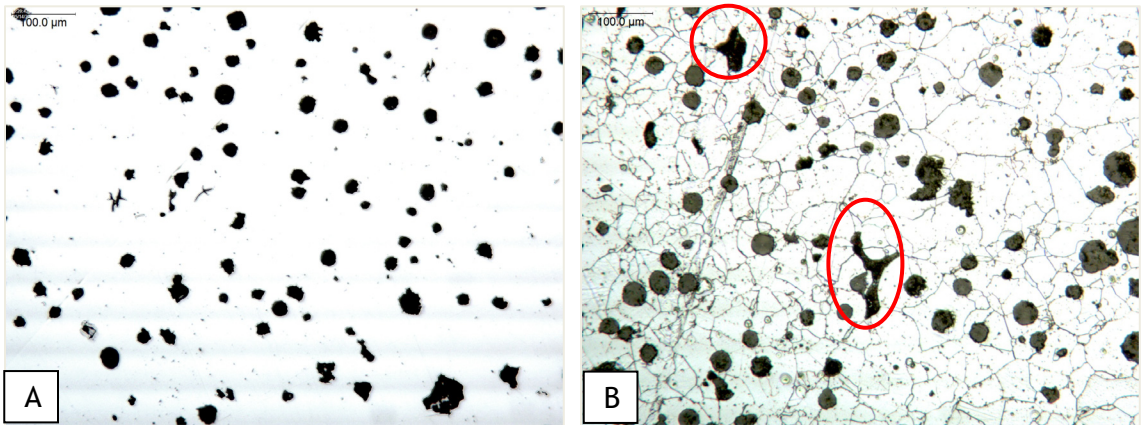
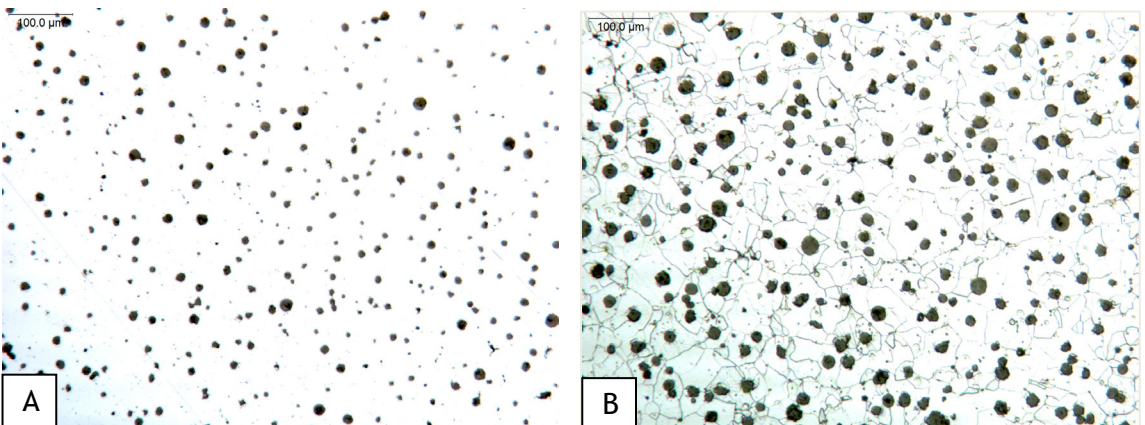


Figure B.12: Medium Si-A5. Some degenerate graphite was present in the form of spiky, chunky and exploded. The spiky graphite is visible in (a). Intercellular pearlite colonies also began to appear (b).



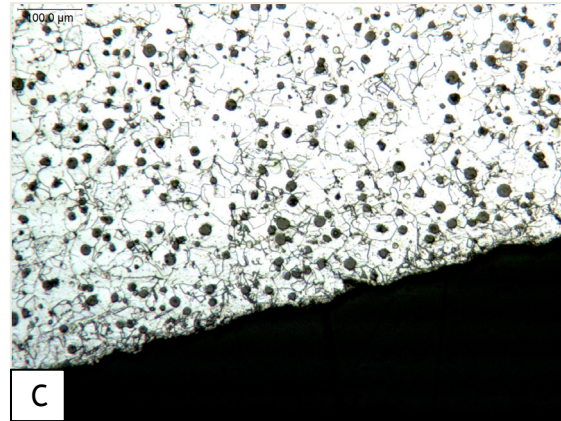


Figure B.13: Medium Si-P1. Small nodules and a high nodule count seen in (a). The ferrite is very fine at the surface (c) and slightly coarser further away from the chill (b)

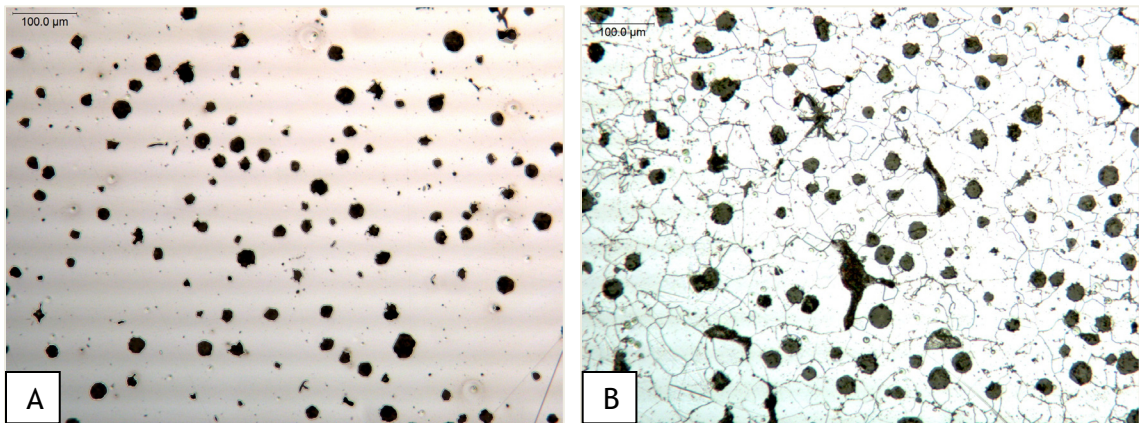


Figure B.14: Medium Si-P3. Note that the graphite nodules in (a) are larger than in Figure B.13(a). Also, more intercellular pearlite colonies are present and in the sample closer to the chill.

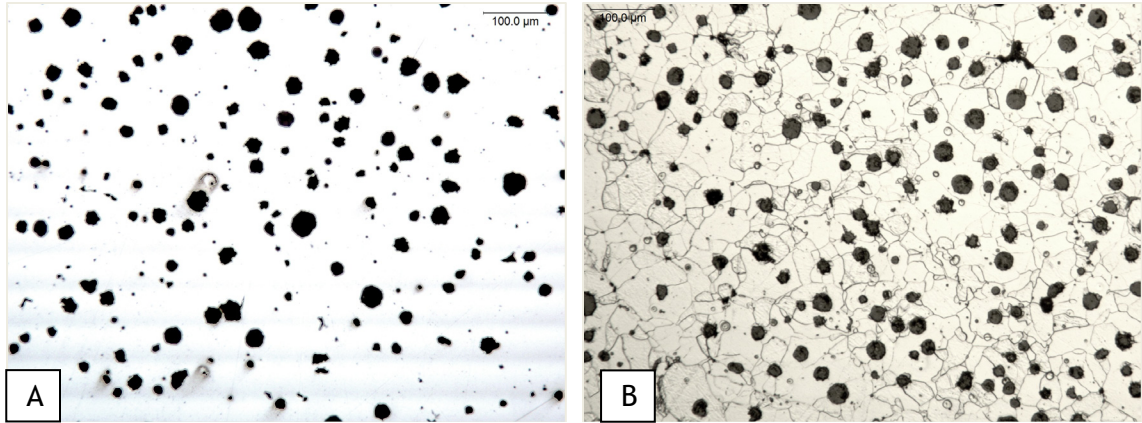


Figure B.15: Medium Si-P5. The nodules are roughly the same as in Medium Si-P3. Relatively the same amount of intercellular pearlite is present. Some degenerate graphite was also present.

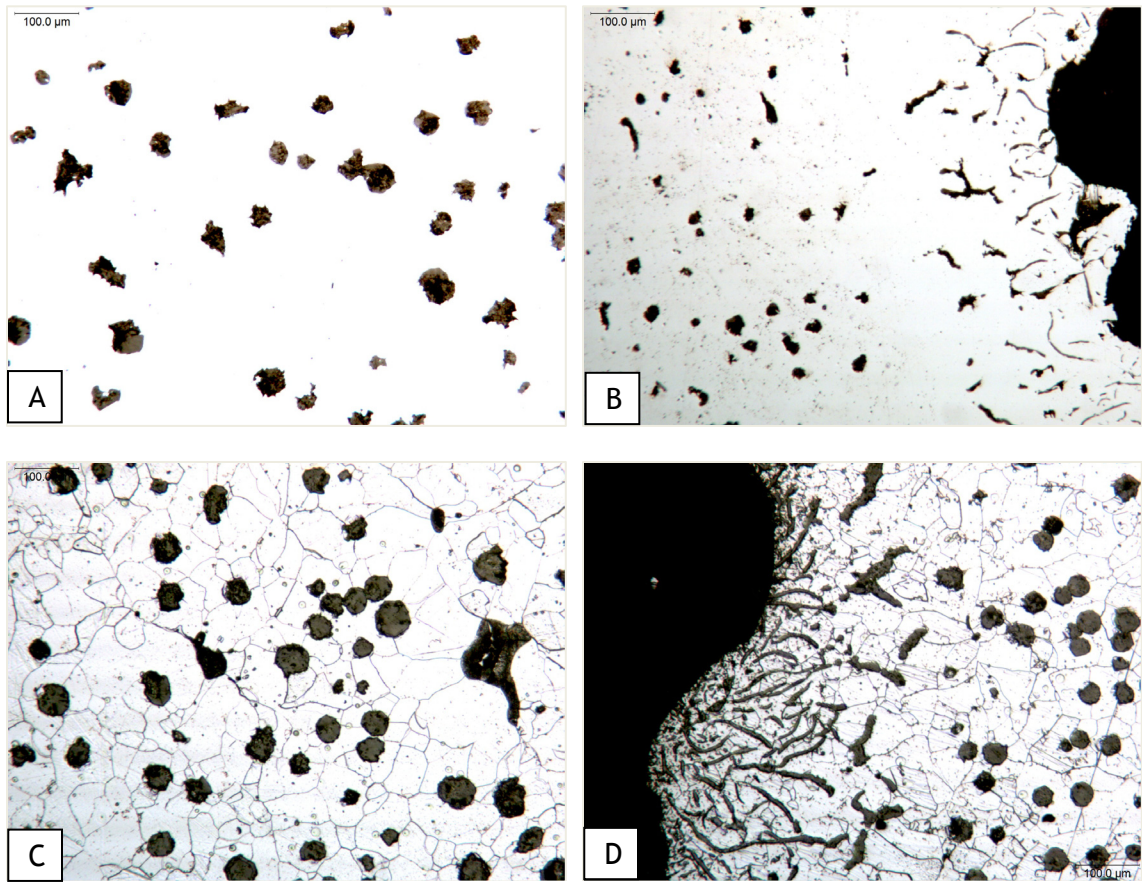


Figure B.16: Medium Si-N1. This sample had noticeable lower nodule count and poor nodularity (a). Compacted graphite was present on the surface of the casting (b) and (d). Intercellular pearlite was also present here where it was virtually absent in the actively and passively chilled blocks.

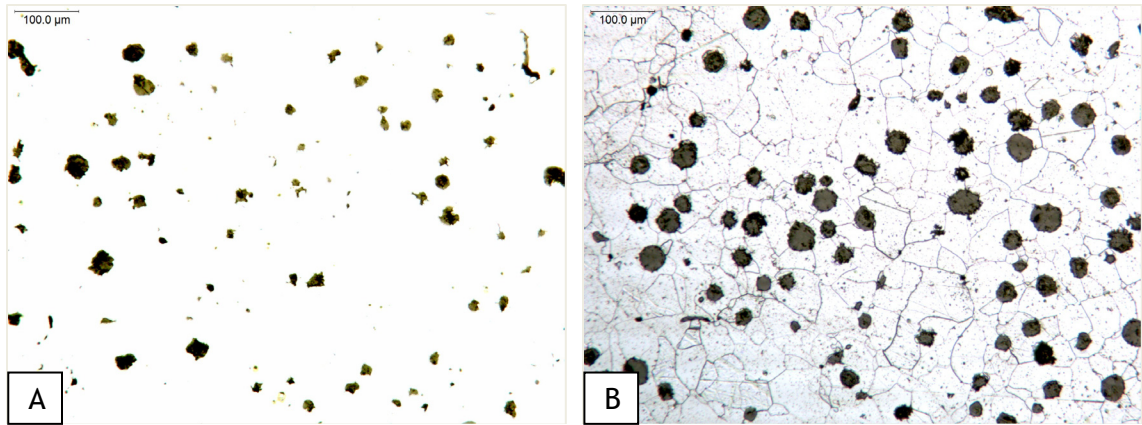


Figure B.17: Medium Si-N3. Poor nodularity and nodule count (a), (b). Nearly identical to medium Si-N1

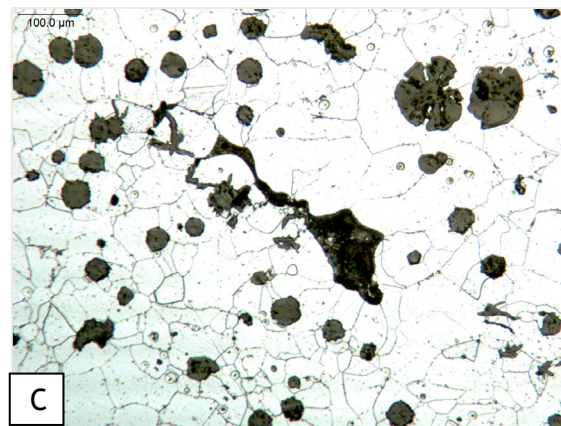
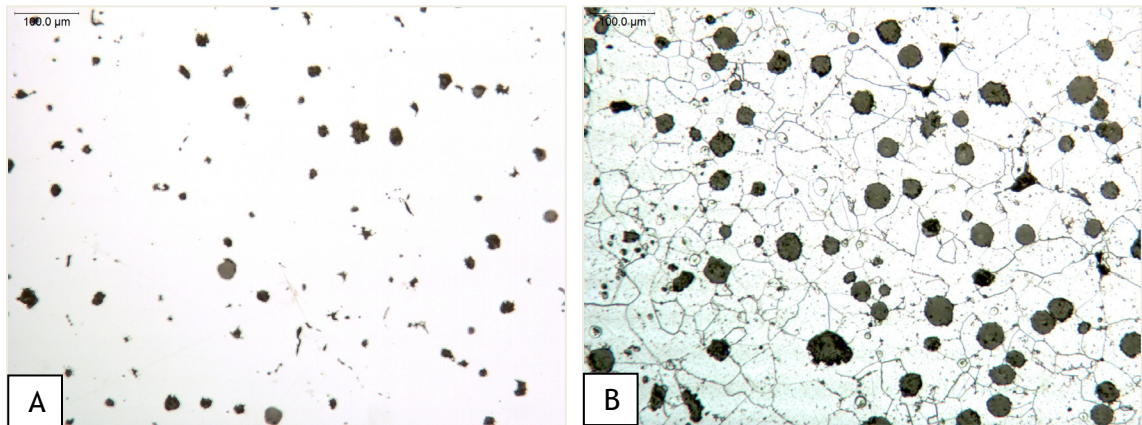


Figure B.18: Medium Si-N5. This sample has very large nodules and the presence of exploded graphite and large intercellular pearlite colonies (c). It also had a low nodule count (a), (b).

HEAT: High Si

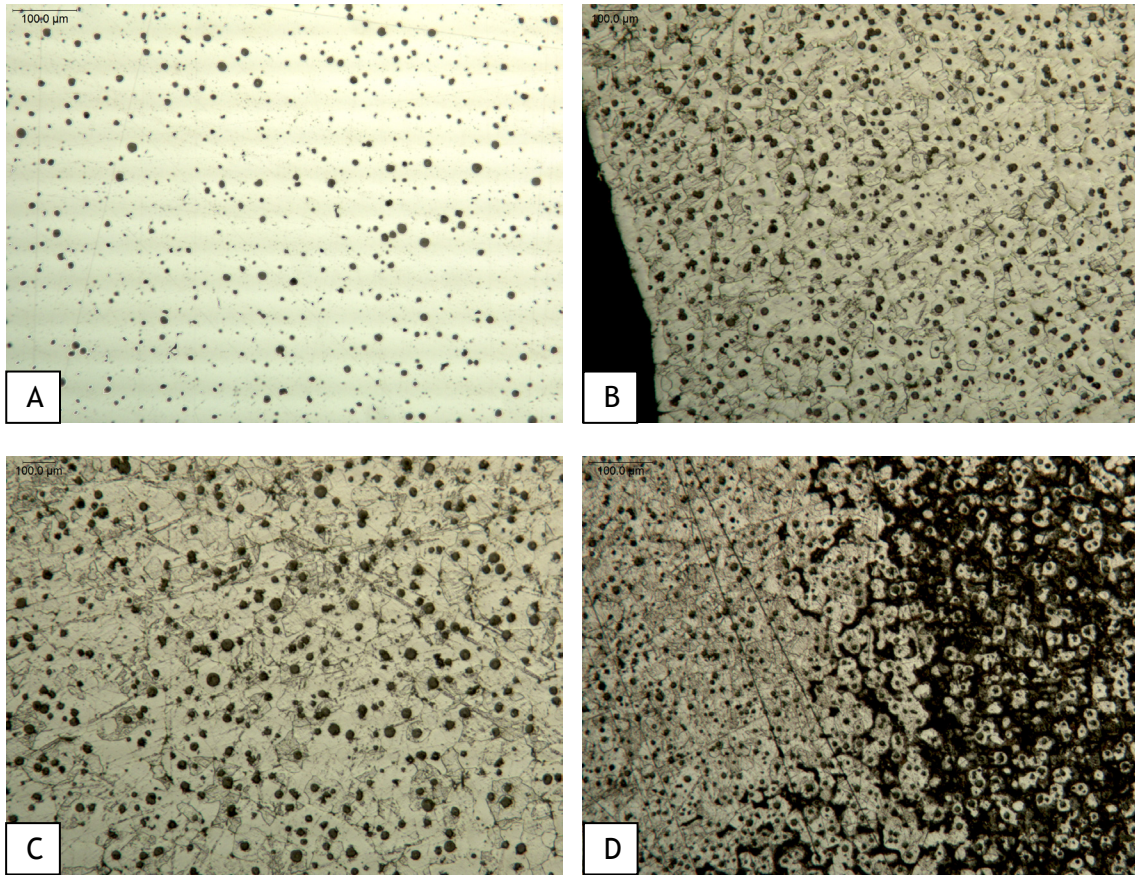
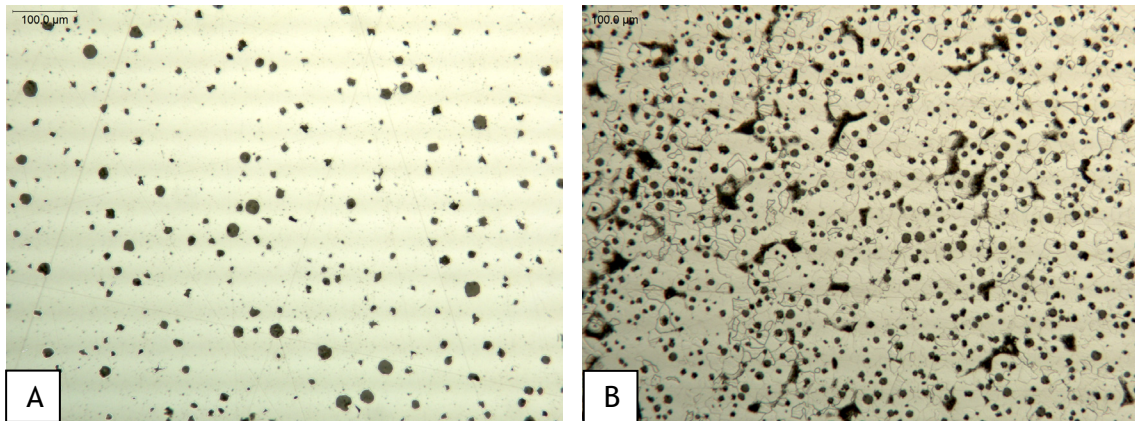


Figure B.19: High Si-A1. Note that it has a very fine graphite morphology (a) and ferrite matrix (b). This sample also had an area of pearlite (d) similar to the medium silicon-A1 sample.



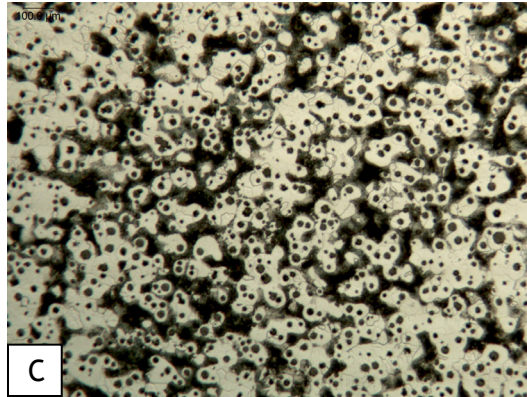


Figure B.20: High Si-A3. The nodules were larger and there was a lower nodule count than in the sample closer to the chill (a). There was also more pearlite present (b). One region showed an unusually high amount of pearlite (c) that appear to be intercellular.

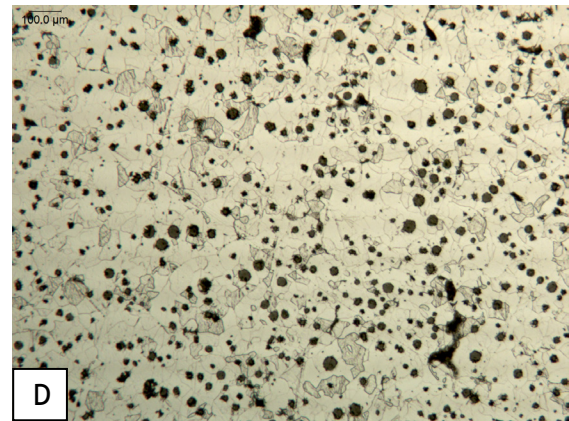
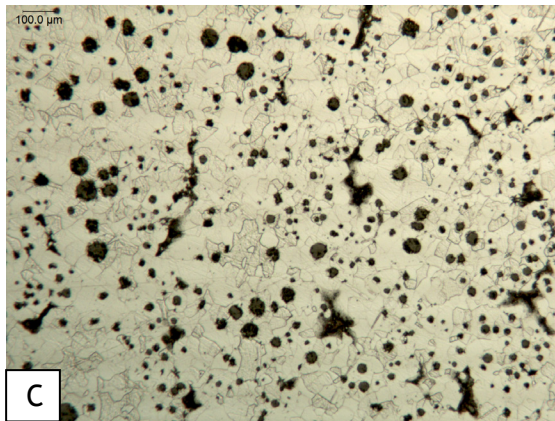
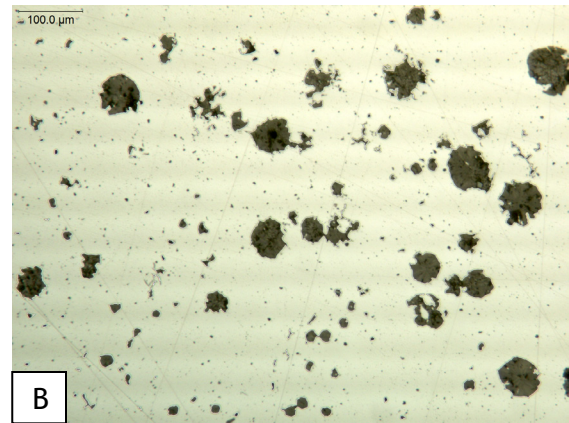
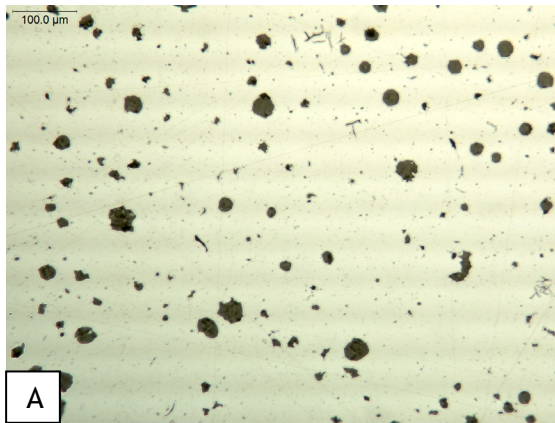


Figure B.21: High Si-A5. Image (a) shows a representative area with decent graphite structure while (b) shows an area with a fair amount of degenerate graphite. The matrix microstructure in (c) and (d), which were obtained at 50x while (a) and (b) were obtained at 100x, is coarser than in the A3 sample. Intercellular pearlite is also present in this sample (c), (d).

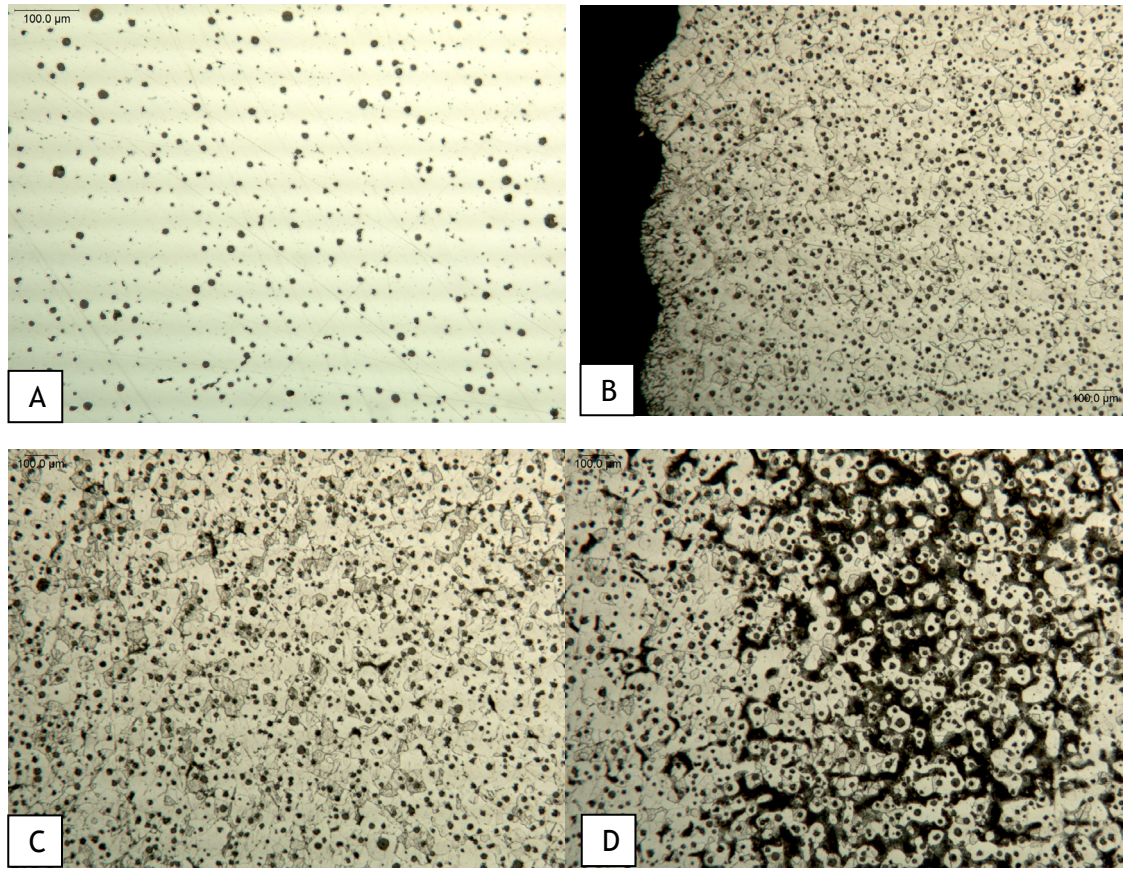


Figure B.22: High Si-P1. This sample had a very fine microstructure like A1. The graphite nodules are small and well-formed (a). The surface shows evidence of compacted graphite (b), but there is no other degenerate graphite. The ferrite was very fine (c); there was also a region of pearlite (d).

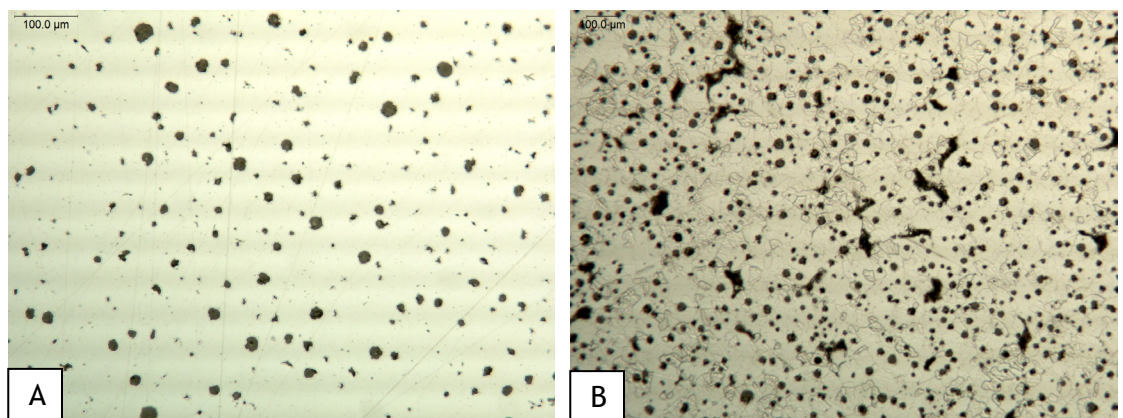


Figure B.23: High Si-P3. This sample had larger nodules and a lower nodule count than P1 (a). Intercellular pearlite also began to appear (b).

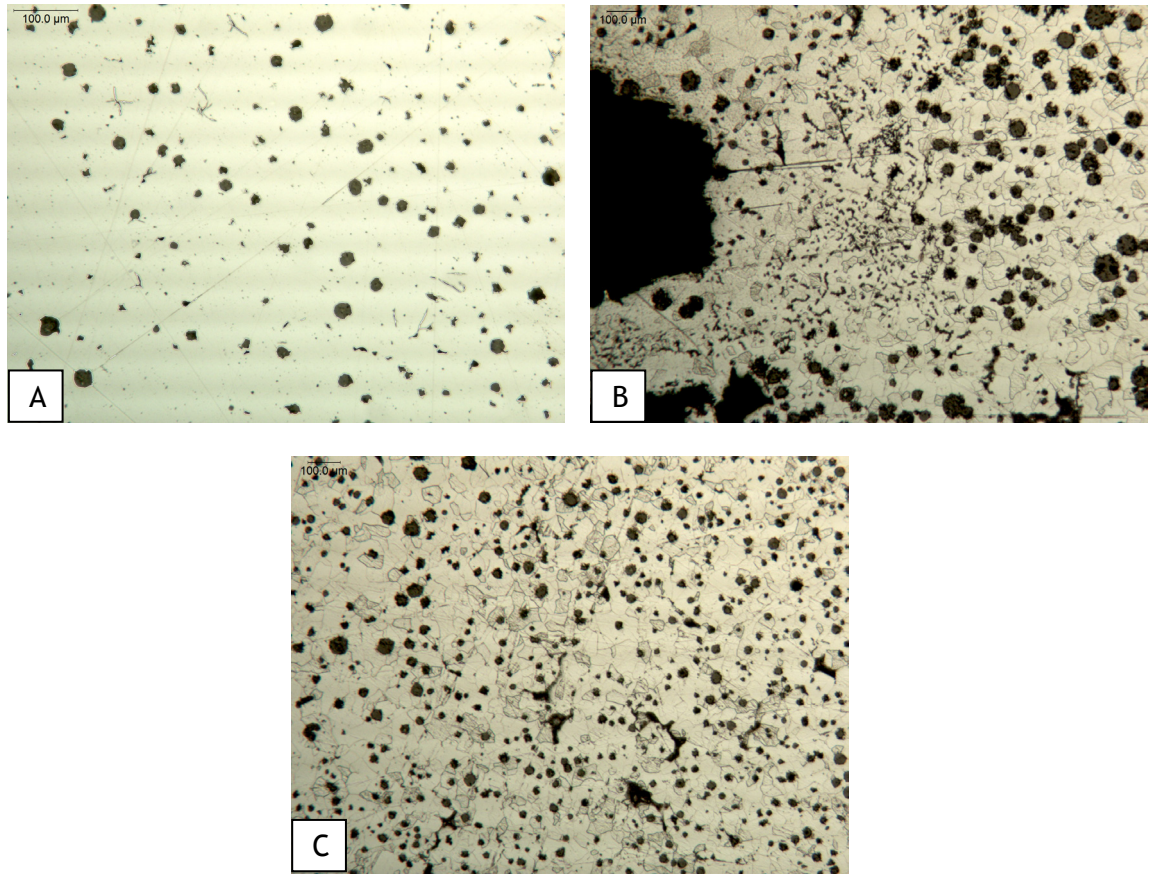
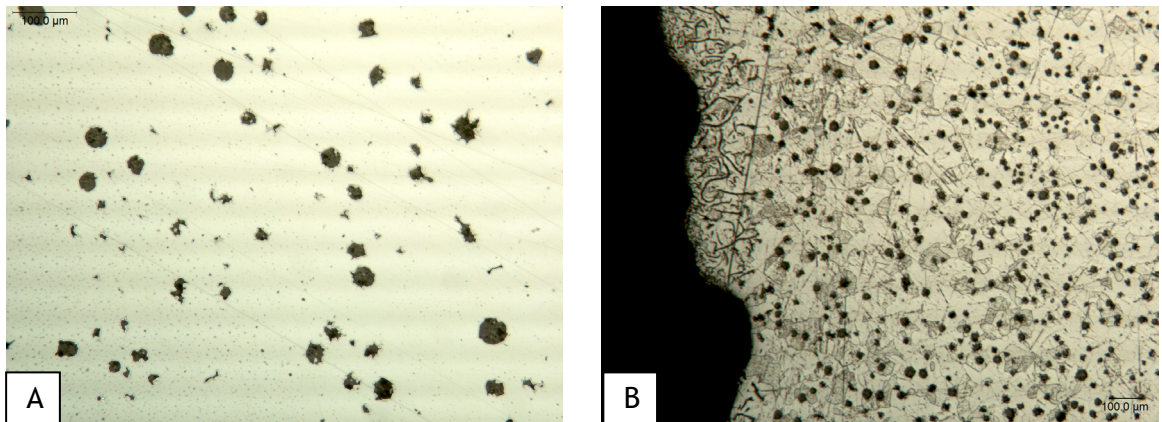


Figure B.24: High Si-P5. A fair amount of degenerate graphite was observed in this sample. In (a), spiky graphite is present while in (b), chunky graphite is present near a portion of the thermocouple. Image (c) shows a representative area with a bimodal distribution in nodules and intercellular pearlite present.



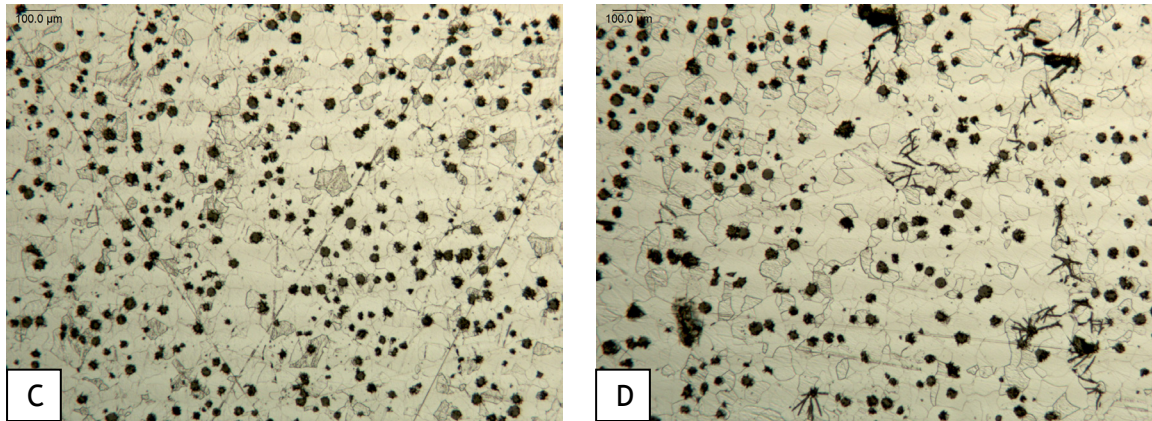


Figure B.25: High Si-N1. This sample had a much lower nodule count than the chilled blocks (a). The surface in (b) shows evidence of compacted graphite. Image (c) was taken at an intermediate distance away from the chill and shows a very good microstructure. However, further away from the chill and spiky graphite forms, the nodule count falls and intercellular pearlite begins to appear (d).

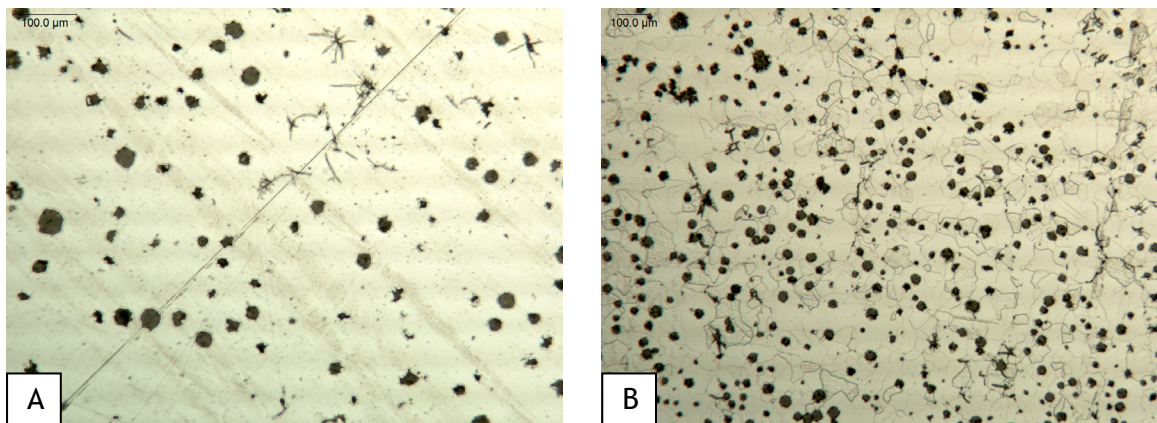


Figure B.26: High Si-N3. The presence of degenerate graphite continues as the distance from the chill increases (a). However, the pearlite is no longer present as it is in N1 (b).

NOTE: Sample High Si-N5 was identical to High Si-N3.

Appendix C ANOVA and Linear Regression Results for Cooling Rate Analysis

An ANOVA analysis was performed for the cooling rate to test if there was a difference between the active and passive chill. According to the ANOVA table below, the p value is 0.883, larger than 0.05, indicating that the chill type was not significant.

General Linear Model: Cooling Rate (C/min) versus Chill Type

Factor	Type	Levels	Values
Chill Type	fixed	2	Active, Passive

Analysis of Variance for Cooling Rate (C/min), using Adjusted SS for Tests

Source	DF	Seq SS	Adj SS	Adj MS	F	P
Chill Type	1	1.39	1.39	1.39	0.02	0.883
Error	16	988.89	988.89	61.81		
Total	17	990.28				

S = 7.86165 R-Sq = 0.14% R-Sq(adj) = 0.00%

It was then necessary to ensure that the difference in chills was not significant for the mechanical properties. In all cases, the ANOVA table indicated p values of greater than the confidence limit of 0.05. Therefore, it was concluded that the chill type was not significant in determining the cooling rate. The ANOVA tables below give the details of the analysis.

General Linear Model: Yield versus Chill Type

Factor	Type	Levels	Values
Chill Type	fixed	2	Active, Passive

Analysis of Variance for Yield, using Adjusted SS for Tests

Source	DF	Seq SS	Adj SS	Adj MS	F	P
Chill Type	1	13	13	13	0.00	0.979
Error	16	300367	300367	18773		
Total	17	300380				

S = 137.014 R-Sq = 0.00% R-Sq(adj) = 0.00%

General Linear Model: Tensile versus Chill Type

Factor	Type	Levels	Values
Chill Type	fixed	2	Active, Passive

Analysis of Variance for Tensile, using Adjusted SS for Tests

Source	DF	Seq SS	Adj SS	Adj MS	F	P
Chill Type	1	1	1	1	0.00	0.993
Error	16	245163	245163	15323		
Total	17	245164				

S = 123.785 R-Sq = 0.00% R-Sq(adj) = 0.00%

General Linear Model: %EL versus Chill Type

Factor	Type	Levels	Values
Chill Type	fixed	2	Active, Passive

Analysis of Variance for %EL, using Adjusted SS for Tests

Source	DF	Seq SS	Adj SS	Adj MS	F	P
Chill Type	1	0.030	0.030	0.030	0.00	0.952
Error	16	129.440	129.440	8.090		
Total	17	129.470				

S = 2.84429 R-Sq = 0.02% R-Sq(adj) = 0.00%

General Linear Model: Hardness versus Chill Type

Factor	Type	Levels	Values
Chill Type	fixed	2	Active, Passive

Analysis of Variance for Hardness, using Adjusted SS for Tests

Source	DF	Seq SS	Adj SS	Adj MS	F	P
Chill Type	1	17	17	17	0.01	0.927
Error	16	30557	30557	1910		
Total	17	30574				

S = 43.7017 R-Sq = 0.05% R-Sq(adj) = 0.00%

General Linear Model: Impact versus Chill Type

Factor	Type	Levels	Values
Chill Type	fixed	2	Active, Passive

Analysis of Variance for Impact, using Adjusted SS for Tests

Source	DF	Seq SS	Adj SS	Adj MS	F	P
Chill Type	1	0.09	0.09	0.09	0.00	0.955
Error	16	448.82	448.82	28.05		
Total	17	448.92				

S = 5.29637 R-Sq = 0.02% R-Sq(adj) = 0.00%

Finally, the significance of the distance from the chill, presence of a chill and Si content were then evaluated for cooling rate. The ANOVA table below shows that the distance and chill presence were both significant factors affecting the cooling rate.

General Linear Model: Cooling Rate (C/min) versus Distance (mm), Chill, Si Content

Factor	Type	Levels	Values
Distance (mm)	fixed	4	0, 40, 80, 120
Chill	fixed	2	chill, none
Si Content	fixed	3	1.77, 3.70, 4.34

Analysis of Variance for Cooling Rate (C/min), using Adjusted SS for Tests

Source	DF	Seq SS	Adj SS	Adj MS	F	P
Distance (mm)	3	1648.92	1648.92	549.64	6.73	0.001
Chill	1	1952.54	1952.54	1952.54	23.91	0.000
Si Content	2	74.74	74.74	37.37	0.46	0.637
Error	29	2368.28	2368.28	81.66		
Total	35	6044.48				

S = 9.03686 R-Sq = 60.82% R-Sq(adj) = 52.71%

Unusual Observations for Cooling Rate (C/min)

Obs	Cooling Rate (C/min)	Fit	SE Fit	Residual	St Resid
17	67.4412	33.3520	3.8399	34.0892	4.17 R

R denotes an observation with a large standardized residual.

Appendix D ANOVA and Linear Regression Results for Quantitative Metallography Results.

Below are the results of an ANOVA analysis and linear regression for both nodularity and nodule count. There were two factors evaluated in each test: Si content and cooling rate. Both factors were found to be significant for nodularity and nodule count.

General Linear Model: Nodularity versus Cooling Rate (C/min), Si Level

Factor	Type	Levels	Values
Cooling Rate (C/min)	fixed	3	5, 15, 30
Si Level	fixed	3	1.77, 3.70, 4.34

Analysis of Variance for Nodularity, using Adjusted SS for Tests

Source	DF	Seq SS	Adj SS	Adj MS	F	P
Cooling Rate (C/min)	2	3500.98	3574.09	1787.05	52.12	0.000
Si Level	2	380.16	380.16	190.08	5.54	0.004
Error	242	8298.02	8298.02	34.29		
Total	246	12179.16				

S = 5.85571 R-Sq = 31.87% R-Sq(adj) = 30.74%

Regression Analysis: Nodularity versus Cooling Rate (C/min), Si Level

The regression equation is

Nodularity = 87.7 + 0.423 Cooling Rate (C/min) - 1.18 Si Level

Predictor	Coef	SE Coef	T	P
Constant	87.667	1.257	69.76	0.000
Cooling Rate (C/min)	0.42304	0.04346	9.73	0.000
Si Level	-1.1797	0.3354	-3.52	0.001

S = 5.94225 R-Sq = 29.3% R-Sq(adj) = 28.7%

Analysis of Variance

Source	DF	SS	MS	F	P
Regression	2	3563.4	1781.7	50.46	0.000
Residual Error	244	8615.7	35.3		
Total	246	12179.2			

Source	DF	Seq SS
Cooling Rate (C/min)	1	3126.6
Si Level	1	436.8

General Linear Model: Nodule Count versus Cooling Rate (C/min), Si Level

Factor	Type	Levels	Values
Cooling Rate (C/min)	fixed	3	5, 15, 30
Si Level	fixed	3	1.77, 3.70, 4.34

Analysis of Variance for Nodule Count, using Adjusted SS for Tests

Source	DF	Seq SS	Adj SS	Adj MS	F	P
Cooling Rate (C/min)	2	1907520	1934273	967137	236.14	0.000
Si Level	2	199236	199236	99618	24.32	0.000
Error	242	991145	991145	4096		
Total	246	3097901				

S = 63.9972 R-Sq = 68.01% R-Sq(adj) = 67.48%

Regression Analysis: Nodularity versus Cooling Rate (C/min), Si Level

The regression equation is

Nodularity = 87.7 + 0.423 Cooling Rate (C/min) - 1.18 Si Level

Predictor	Coef	SE Coef	T	P
Constant	87.667	1.257	69.76	0.000
Cooling Rate (C/min)	0.42304	0.04346	9.73	0.000
Si Level	-1.1797	0.3354	-3.52	0.001

S = 5.94225 R-Sq = 29.3% R-Sq(adj) = 28.7%

Analysis of Variance

Source	DF	SS	MS	F	P
Regression	2	3563.4	1781.7	50.46	0.000
Residual Error	244	8615.7	35.3		
Total	246	12179.2			

Source	DF	Seq SS
Cooling Rate (C/min)	1	3126.6
Si Level	1	436.8

Appendix E ANOVA and Linear Regression Results for Analysis of the Effect of Si Content and Cooling Rate on Hardness

The following ANOVA analysis evaluated the effect of cooling rate and Si content on the measured hardness. It was found that the Si content was significant while the cooling rate was not for a 95% confidence limit.

General Linear Model: Hardness versus Si Content (wt%), Cooling Rate (C/min)

Factor	Type	Levels	Values
Si Content (wt%)	fixed	3	1.77, 3.70, 4.34
Cooling Rate (C/min)	fixed	3	5, 15, 30

Analysis of Variance for Hardness, using Adjusted SS for Tests

Source	DF	Seq SS	Adj SS	Adj MS	F	P
Si Content (wt%)	2	248131	248162	124081	1357.77	0.000
Cooling Rate (C/min)	2	550	550	275	3.01	0.053
Error	129	11789	11789	91		
Total	133	260469				

S = 9.55959 R-Sq = 95.47% R-Sq(adj) = 95.33%

Main Effects Plot for Hardness

Appendix F ANOVA and Linear Regression Results for Mechanical Testing Data

ANOVA analyses were also performed for the tensile testing results. The ANOVA tables given below indicate that Si content and cooling rates were significant for yield stress, tensile strength and elongation. Neither factor was significant for Young's modulus.

General Linear Model: Modulus (GPa), Yield Strength (MPa), Tensile Strength (MPa), %Elongation versus Si Level, Cooling Rate (C/min)

Factor	Type	Levels	Values
Si Level	fixed	3	1.77, 3.70, 4.34
Cooling Rate (C/min)	fixed	3	5, 15, 30

Analysis of Variance for Modulus (GPa), using Adjusted SS for Tests

Source	DF	Seq SS	Adj SS	Adj MS	F	P
Si Level	2	184.72	117.51	58.76	0.67	0.516
Cooling Rate (C/min)	2	416.86	416.86	208.43	2.37	0.101
Error	76	6691.83	6691.83	88.05		
Total	80	7293.41				

S = 9.38352 R-Sq = 8.25% R-Sq(adj) = 3.42%

Unusual Observations for Modulus (GPa)

Obs	Modulus (GPa)	Fit	SE Fit	Residual	St Resid
11	208.977	180.108	2.775	28.869	3.22 R
28	151.855	171.495	2.037	-19.640	-2.14 R
37	156.288	177.244	3.011	-20.956	-2.36 R
40	196.925	171.495	2.037	25.430	2.78 R

R denotes an observation with a large standardized residual.

Analysis of Variance for Yield Strength (MPa), using Adjusted SS for Tests

Source	DF	Seq SS	Adj SS	Adj MS	F	P
Si Level	2	1297605	1273627	636814	8975.40	0.000
Cooling Rate (C/min)	2	9127	9127	4564	64.32	0.000
Error	76	5392	5392	71		
Total	80	1312125				

S = 8.42324 R-Sq = 99.59% R-Sq(adj) = 99.57%

Unusual Observations for Yield Strength (MPa)

Yield Strength					
Obs	(MPa)	Fit	SE Fit	Residual	St Resid
57	559.643	541.962	2.491	17.681	2.20 R
78	503.792	520.137	2.095	-16.345	-2.00 R
81	495.716	520.137	2.095	-24.420	-2.99 R

R denotes an observation with a large standardized residual.

Analysis of Variance for Tensile Strength (MPa), using Adjusted SS for Tests

Source	DF	Seq SS	Adj SS	Adj MS	F	P
Si Level	2	1051630	1031200	515600	4918.39	0.000
Cooling Rate (C/min)	2	15642	15642	7821	74.61	0.000
Error	76	7967	7967	105		
Total	80	1075240				

S = 10.2387 R-Sq = 99.26% R-Sq(adj) = 99.22%

Unusual Observations for Tensile Strength (MPa)

Tensile Strength					
Obs	(MPa)	Fit	SE Fit	Residual	St Resid
31	370.119	399.159	2.223	-29.040	-2.91 R
57	694.555	671.998	3.028	22.557	2.31 R
78	621.604	641.939	2.546	-20.334	-2.05 R
79	619.571	641.939	2.546	-22.367	-2.26 R
80	619.173	641.939	2.546	-22.766	-2.30 R
81	609.464	641.939	2.546	-32.475	-3.27 R

R denotes an observation with a large standardized residual.

Analysis of Variance for Elongation (%), using Adjusted SS for Tests

Source	DF	Seq SS	Adj SS	Adj MS	F	P
Si Level	2	716.98	732.65	366.33	41.77	0.000
Cooling Rate (C/min)	2	194.45	194.45	97.22	11.09	0.000
Error	76	666.46	666.46	8.77		
Total	80	1577.89				

S = 2.96128 R-Sq = 57.76% R-Sq(adj) = 55.54%

Unusual Observations for Elongation (%)

Elongation					
Obs	(%)	Fit	SE Fit	Residual	St Resid
3	13.0100	19.1953	0.8757	-6.1853	-2.19 R
31	4.7760	22.3635	0.6428	-17.5875	-6.08 R

R denotes an observation with a large standardized residual.

Regression Analysis: Modulus (GPa) versus Cooling Rate (C/min), Si Level

The regression equation is

$$\text{Modulus (GPa)} = 167 + 0.236 \text{ Cooling Rate (C/min)} + 1.09 \text{ Si Level}$$

Predictor	Coef	SE Coef	T	P
Constant	167.164	3.590	46.57	0.000
Cooling Rate (C/min)	0.2355	0.1206	1.95	0.054
Si Level	1.0872	0.9541	1.14	0.258

S = 9.34321 R-Sq = 6.6% R-Sq(adj) = 4.2%

Analysis of Variance

Source	DF	SS	MS	F	P
Regression	2	484.36	242.18	2.77	0.069
Residual Error	78	6809.05	87.30		
Total	80	7293.41			

Source	DF	Seq SS
Cooling Rate (C/min)	1	371.00
Si Level	1	113.35

Unusual Observations

Obs	Cooling Rate (C/min)	Modulus (GPa)	Fit	SE Fit	Residual	St Resid
11	30.0	208.98	178.25	2.15	30.72	3.38R
28	15.0	151.85	172.62	1.77	-20.77	-2.26R
37	30.0	156.29	176.15	2.67	-19.87	-2.22R
38	30.0	194.22	176.15	2.67	18.07	2.02R
40	15.0	196.92	172.62	1.77	24.30	2.65R
47	5.0	188.62	170.27	2.03	18.36	2.01R

R denotes an observation with a large standardized residual.

Regression Analysis: Yield Strength (MPa) versus Cooling Rate (C/min), Si Level

The regression equation is

$$\text{Yield Strength (MPa)} = 19.4 + 0.927 \text{ Cooling Rate (C/min)} + 115 \text{ Si Level}$$

Predictor	Coef	SE Coef	T	P
Constant	19.418	4.253	4.57	0.000
Cooling Rate (C/min)	0.9271	0.1429	6.49	0.000
Si Level	115.211	1.130	101.93	0.000

S = 11.0689 R-Sq = 99.3% R-Sq(adj) = 99.3%

Analysis of Variance

Source	DF	SS	MS	F	P
Regression	2	1302568	651284	5315.69	0.000
Residual Error	78	9557	123		
Total	80	1312125			

Source	DF	Seq SS
Cooling Rate (C/min)	1	29616
Si Level	1	1272952

Unusual Observations

Obs	Cooling Rate (C/min)	Yield Strength (MPa)	Fit	SE Fit	Residual	St Resid
2	30.0	448.06	473.51	2.55	-25.45	-2.36R
11	30.0	448.36	473.51	2.55	-25.15	-2.34R
59	15.0	556.62	533.34	1.72	23.28	2.13R
81	5.0	495.72	524.07	2.25	-28.35	-2.62R

R denotes an observation with a large standardized residual.

Regression Analysis: Tensile Strength versus Cooling Rate (C/min), Si Level

The regression equation is

Tensile Strength (MPa) = 188 + 1.26 Cooling Rate (C/min) + 103 Si Level

Predictor	Coef	SE Coef	T	P
Constant	187.670	5.778	32.48	0.000
Cooling Rate (C/min)	1.2568	0.1941	6.47	0.000
Si Level	103.256	1.536	67.23	0.000

S = 15.0400 R-Sq = 98.4% R-Sq(adj) = 98.3%

Analysis of Variance

Source	DF	SS	MS	F	P
Regression	2	1057596	528798	2337.74	0.000
Residual Error	78	17644	226		
Total	80	1075240			

Source	DF	Seq SS
Cooling Rate (C/min)	1	35106
Si Level	1	1022491

Unusual Observations

Obs	Cooling Rate (C/min)	Tensile Strength (MPa)	Fit	SE Fit	Residual	St Resid
2	30.0	576.43	607.42	3.46	-30.99	-2.12R

68	15.0	686.52	654.66	2.34	31.87	2.15R
81	5.0	609.46	642.09	3.06	-32.62	-2.22R

R denotes an observation with a large standardized residual.

Regression Analysis: Elongation (%) versus Cooling Rate (C/min), Si Level

The regression equation is

Elongation (%) = 24.4 + 0.168 Cooling Rate (C/min) - 2.80 Si Level

Predictor	Coef	SE Coef	T	P
Constant	24.448	1.164	21.01	0.000
Cooling Rate (C/min)	0.16759	0.03910	4.29	0.000
Si Level	-2.7956	0.3093	-9.04	0.000

S = 3.02939 R-Sq = 54.6% R-Sq(adj) = 53.5%

Analysis of Variance

Source	DF	SS	MS	F	P
Regression	2	862.07	431.03	46.97	0.000
Residual Error	78	715.82	9.18		
Total	80	1577.89			

Source	DF	Seq SS
Cooling Rate (C/min)	1	112.57
Si Level	1	749.50

Unusual Observations

Obs	Cooling Rate (C/min)	Elongation (%)	Fit	SE Fit	Residual	St Resid
3	30.0	13.010	19.132	0.698	-6.122	-2.08R
31	15.0	4.776	22.014	0.575	-17.238	-5.80R
80	5.0	7.156	13.153	0.617	-5.997	-2.02R
81	5.0	6.874	13.153	0.617	-6.279	-2.12R

R denotes an observation with a large standardized residual.

The uncertainty in the tensile modulus was high due to a number of variables: therefore, the ultrasonic modulus was determined and analyzed below.

General Linear Model: Ultrasonic Modulus versus Si Level, Cooling Rate (C/min)

Factor	Type	Levels	Values
Si Level	fixed	3	1.77, 3.70, 4.34
Cooling Rate (C/min)	fixed	3	5, 15, 30

Analysis of Variance for Ultrasonic Modulus, using Adjusted SS for Tests

Source	DF	Seq SS	Adj SS	Adj MS	F	P
Si Level	2	813.68	812.29	406.15	15.34	0.000
Cooling Rate (C/min)	2	82.74	82.74	41.37	1.56	0.216
Error	76	2012.04	2012.04	26.47		
Total	80	2908.46				

S = 5.14532 R-Sq = 30.82% R-Sq(adj) = 27.18%

Unusual Observations for Ultrasonic Modulus

Ultrasonic						
Obs	Modulus	Fit	SE Fit	Residual	St Resid	
76	190.200	178.101	1.280	12.099	2.43	R
77	190.200	178.101	1.280	12.099	2.43	R
78	190.200	178.101	1.280	12.099	2.43	R
79	163.800	178.101	1.280	-14.301	-2.87	R
80	163.800	178.101	1.280	-14.301	-2.87	R
81	163.800	178.101	1.280	-14.301	-2.87	R

R denotes an observation with a large standardized residual.

Appendix G ANOVA and Linear Regression Results for Charpy Impact Results

The Charpy data was analyzed for the effect of Si content and cooling rate. It was found that the Si content was a significant factor for all alloy at all testing temperatures.

General Linear Model: Energy (J) versus Si Content, Cooling Rate (C/min)

Factor	Type	Levels	Values
Si Content	fixed	3	1.77, 3.70, 4.34
Cooling Rate (C/min)	fixed	3	5, 15, 30

Analysis of Variance for Energy (J), using Adjusted SS for Tests

Source	DF	Seq SS	Adj SS	Adj MS	F	P
Si Content	2	3554.53	3479.83	1739.92	722.88	0.000
Cooling Rate (C/min)	2	7.83	7.83	3.92	1.63	0.200
Error	157	377.89	377.89	2.41		
Total	161	3940.25				

S = 1.55143 R-Sq = 90.41% R-Sq(adj) = 90.17%

Unusual Observations for Energy (J)

Obs	Energy (J)	Fit	SE Fit	Residual	St Resid
86	8.1000	11.5344	0.2382	-3.4344	-2.24 R
90	1.7000	11.5344	0.2382	-9.8344	-6.41 R
91	8.1000	11.5240	0.3521	-3.4240	-2.27 R
93	8.1000	11.5344	0.2382	-3.4344	-2.24 R
94	8.1000	11.5344	0.2382	-3.4344	-2.24 R
115	15.9000	11.9958	0.2733	3.9042	2.56 R
116	16.3000	11.9958	0.2733	4.3042	2.82 R
117	15.6000	11.9958	0.2733	3.6042	2.36 R
118	15.3000	11.9958	0.2733	3.3042	2.16 R
120	15.3000	11.9958	0.2733	3.3042	2.16 R
152	8.8000	11.9958	0.2733	-3.1958	-2.09 R
155	8.5000	11.9958	0.2733	-3.4958	-2.29 R
156	8.8000	11.9958	0.2733	-3.1958	-2.09 R

R denotes an observation with a large standardized residual.

Regression Analysis: Energy (J) versus Si Content

The regression equation is
Energy (J) = 18.8 - 4.21 Si Content

Predictor	Coef	SE Coef	T	P
Constant	18.8197	0.4479	42.02	0.000

Si Content -4.2051 0.1299 -32.37 0.000

S = 1.80635 R-Sq = 86.8% R-Sq(adj) = 86.7%

Analysis of Variance

Source	DF	SS	MS	F	P
Regression	1	3418.2	3418.2	1047.59	0.000
Residual Error	160	522.1	3.3		
Total	161	3940.2			

Additionally, the data from each testing temperature was analyzed for the effect of Si content and cooling rate. The Si content was found to be significant for all while the cooling rate was significant for the -20°C test temperature and nearly significant (p=0.055) for the room temperature tests.

Results for: Room Temperature Tests

General Linear Model: Energy versus Si Content, Cooling Rate (C/min)

Factor	Type	Levels	Values
Si Content	fixed	3	1.77, 3.70, 4.34
Cooling Rate (C/min_	fixed	3	5, 15, 30

Analysis of Variance for Energy, using Adjusted SS for Tests

Source	DF	Seq SS	Adj SS	Adj MS	F	P
Si Content	2	802.20	802.20	401.10	492.55	0.000
Cooling Rate (C/min_	2	5.42	5.42	2.71	3.33	0.055
Error	22	17.92	17.92	0.81		
Total	26	825.53				

S = 0.902405 R-Sq = 97.83% R-Sq(adj) = 97.44%

Results for: -20C Test Temperature

General Linear Model: Energy versus Si Content, Cooling Rate (C/min)

Factor	Type	Levels	Values
Si Content	fixed	3	1.77, 3.70, 4.34
Cooling Rate (C/min_	fixed	3	5, 15, 30

Analysis of Variance for Energy, using Adjusted SS for Tests

Source	DF	Seq SS	Adj SS	Adj MS	F	P
Si Content	2	708.11	708.11	354.06	677.39	0.000
Cooling Rate (C/min_	2	4.04	4.04	2.02	3.87	0.036
Error	22	11.50	11.50	0.52		
Total	26	723.66				

S = 0.722967 R-Sq = 98.41% R-Sq(adj) = 98.12%

Results for: -40C Test Temperature

General Linear Model: Energy versus Si Content, Cooling Rate (C/min)

Factor	Type	Levels	Values
Si Content	fixed	3	1.77, 3.70, 4.34
Cooling Rate (C/min_	fixed	3	5, 15, 30

Analysis of Variance for Energy, using Adjusted SS for Tests

Source	DF	Seq SS	Adj SS	Adj MS	F	P
Si Content	2	324.635	324.635	162.318	338.64	0.000
Cooling Rate (C/min_	2	0.760	0.760	0.380	0.79	0.465
Error	22	10.545	10.545	0.479		
Total	26	335.940				

S = 0.692326 R-Sq = 96.86% R-Sq(adj) = 96.29%